UNIVERSITY OF CALIFORNIA

Santa Barbara

Development of Functionalized Carbon Surfaces with Redox Switchable Compounds for Clean Energy Applications

A dissertation submitted in partial satisfaction of the

requirements for the degree Doctor of Philosophy

in Chemistry

by

Maxwell Robert Mattejat

Committee in charge:

Professor Gabriel Ménard, Chair

Professor Mahdi Abu-Omar

Professor Trevor Hayton

Professor Lior Sepunaru

June 2023

The dissertation of Maxwell Robert Mattejat is approved.

_____
Mahdi Abu-Omar

_____
Trevor Hayton

_____
Lior Sepunaru

_____
Gabriel Ménard, Committee Chair

May 2023

Development of Functionalized Carbon Surfaces with Redox Switchable Compounds for Clean Energy Applications

ACKNOWLEDGEMENTS

My graduate career has been very akin to my surfing. The highs of riding a perfect wave all the way from the point to the beach are analogous to the feelings of finally getting that key piece data to publish. Getting that perfect wave or that piece of data never came without the hard work of paddling out to the break or endless hours researching, prepping, and analyzing data. Much like learning to surf, developing as a scientist was not achieved alone and required a lot of support from mentors, friends, and family.

I have to first thank my mentor and supervisor Gabriel Ménard. Even though you were physically gone for what seems like 50% of my time here, you always made time to talk through problems, develop new plans, and help me grow as a scientist. Thank you for allowing me to explore the numerous crazy ideas I had that were outside our normal approaches. While many of these ideas did not succeed, your support helped me learn and grow from the failures. I cannot thank you enough for all your support over these past five years.

My accomplishments would not have been possible without the support of my friends and lab mates. We in the Gab lab have a unique way of constructively pushing each other to improve our results and communicate them effectively. I have appreciated our numerous grilling discussions that have developed as an effective scientist. I would like to specifically thank Arun and Shannon. Arun, I cannot thank you enough for your support as a friend and lab mate. You have been instrumental in helping me work through so many problems from dumb issues with potentiostats to complex electrochemistry. Your suggestions on podcast were always top tier and helped me enjoy many hours of tedious dilutions. Shannon, thank you for your friendship and support in the lab. Your encouragement and push for me to always

do that next experiment helped me keep my drive in lab. I enjoyed the camping trips we were able to take and glad you were not mad at me about the accidental 18 mile hike I took us on. I wish we had time to fit more adventures in during my time here.

I also would like to thank the numerous UCSB staff members that have helped me over the years, especially Guang Wu, Hongjun Zhou, and Amanda Storm. The data collection for my projects would not have been possible without your support.

I have to thank my brother and Dad for their continued support of my pursuits. You both have always supported me with all the adventures and have always been there when I needed you.

Lastly, I could not have finished this program without my biggest supporter and partner Christina. You have always been there for me on the best and worst of days. With each other's support, I know we can tackle anything in our way. I am excited to ride the wave that is life with you. Love you more, forever and always.

VITA OF MAXWELL ROBERT MATTEJAT

May 2023

EDUCATION

Bachelor of Science in Chemistry, University of North Carolina Wilmington 2018
Doctor of Philosophy in Chemistry, University of California, Santa Barbara, May 2023

PROFESSIONAL EMPLOYMENT

2016-2018: Student Researcher, Department of Chemistry University of North Carolina Wilmington
Summer 2017: NOAA Hollings Internship, NIST, Charleston South Carolina
2018-2022: Teaching Assistant, Department of Chemistry University of California, Santa Barbara

PUBLICATIONS

Mattejat, M.; Ménard, G. *ChemComm* Submitted

Mattejat, M.; Peterson, M.; Chakraborty A.; Ménard, G. *Energy Fuels* 2023, *37* (1), 785–790

Mattejat, M.; Keener, M.; Zheng, S.-L.; Wu, G.; Hayton, T. W.; Ménard, G. *Chem. Sci.* 2022 *13* (12), 3369-3374

Hunt, C.; Mattejat, M.; Anderson, C.; Sepunaru, L.; Ménard, G. *ACS Appl. Energy Mater*.2019, *2* (8), 5391-5396

Heinrich, S; Benhaim, H; Mattejat, M.; Ménard, G. *In Preparation*

AWARDS

Honorable Mention in the National Science Foundation Graduate Research Fellowship 2020
National Oceanic and Atmospheric Administration Hollings Scholar 2016
American Chemical Society Division of Organic Chemistry Undergraduate award 2018

FIELDS OF STUDY

Major Field: Inorganic Chemistry, Minor Field: Electrochemistry

Abstract

Development of Functionalized Carbon Surfaces with Redox Switchable Compounds for Clean Energy Applications

by

Maxwell Robert Mattejat

Global energy consumption continues to increase annually, leading to dangerous levels of atmospheric carbon dioxide. To avoid irreparable harm to our planet, we need to rapidly convert our grid from fossil fuel dependence to low carbon sources of energy such as nuclear, wind and solar power. These technologies, however, need further development before the full conversion of our grid can occur. In this dissertation, we present advancements in spent nuclear fuel recycling and redox flow batteries for energy storage.

In the first half, we studied the use of electrochemically switchable carboranes (polyhedral boron-carbon cluster compounds) for selective actinide capture from simulated spent nuclear fuel. Initially utilizing a biphasic approach, an organic phase containing an electrochemically generated *ortho*-substituted *nido*-carborane anion, ($^{PO}Cb^{2-}$) was found to selectively extract uranyl (UO_2^{2+}) from a mixed-metal alkali (Cs^+), lanthanide (Nd^{3+}, Sm^{3+}), and actinide (Th^{4+}, UO_2^{2+}) aqueous solutions. Bulk electrolysis of the organic phase was used to re-generate the *closo*-carborane (^{PO}Cb) and release the captured UO_2^{2+}, which was later back-extracted into a fresh aqueous phase.

In a follow up study, we heterogenized our molecular, electrochemically switchable carboranes onto carbon electrodes. These functionalized electrodes demonstrated carborane-based heterogeneous electrochemical behaviour enhanced by the inclusion of single-walled carbon nanotubes (CNTs). Charged functionalized electrodes selectively captured and released actinides (Th^{4+}, UO_2^{2+}) from a mixed solutions containing alkali (Cs^{+}), lanthanide (Nd^{3+}, Sm^{3+}) and actinide (Th^{4+}, UO_2^{2+}) metal ions.

In the second half of my thesis, we demonstrated the use of commercially available phthalocyanine metal complexes (PcM) as cheap charge carriers in RFBs for green energy storage. Our systems utilized slurries of conductive carbon Ketjenblack (KB) to create electronically conducting percolation networks that interfaced with undissolved PcM. We found no significant performance differences between the commercial unsubstituted PcM and 1,4,8,11,15,18,22,25-octaethoxyphthalocyanine metal complexes (^{EtO}PcM) synthesized with peripheral solubilizing substituents despite their increased solubility. Electrochemical analyses of several commercial first-row variants ($PcTiCl_2$, PcVO, PcMnCl, PcFe, PcCo, PcNi, and PcCu) as well as one heavy-metal analogue (PcPb) revealed most to be effective charge carriers for slurry-based PcM/KB RFB applications. Cells using PcCu proved to have the highest efficiencies, energy density (1.23 Wh/L), and stability (>99% capacity retention) of the series while also having the lowest cost by mass.

Table of Contents

List of Figures

List of Symbols and Abbreviations

A	amp
AEM	anion exchange membrane
ATR-FTIR	attenuated total reflectance fourier transform infrared spectroscopy
Cb	*ortho*-carborane
^{PO}Cb	1,2-$(Ph_2PO)_2$-1,2-$C_2B_{10}H_{10}$
^{PO}Cb-Pyr	1,2-$(Ph_2PO)_2$-9- pyrenyl-1,2-$C_2B_{10}H_{10}$
CD_2Cl_2	deuterated dichloromethane
CF	carbon fiber
CNT	carbon nanotubes
Cp*	pentamethylcyclopentadienyl
CV	cyclic voltammetry
DCE	1,2-dichloroethane
DCM	dichloromethane
DCM-d_2	deuterated dichloromethane
DPV	differential pulse voltammetry
ESS	energy storage systems
equiv	equivalent
Et	ethyl
^{OEt}PC	1,4,8,11,15,18,22,25-octaethoxyphthalocyanine
Fc	ferrocene
Fc^+	ferrocenium

g	gram
GC	glassy carbon
h	hour
I	current
ICP-MS	inductively coupled plasma mass spectrometry
ITO	indium tin oxide
L	liter
M	molar
MeCN	acetonitrile
MeCN-d_3	deuterated acetonitrile
min	minute
mol	mole
*n*BuLi	n-butyl lithium
NMR	nuclear magnetic resonance
OAc	acetate
^{o}C	degrees Celsius
Pc	phthalocyanine
Ph	phenyl
ppm	parts per million
PUREX	plutonium and uranium reduction extraction
Pyr	pyrene
RFB	redox flow battery
r.t.	room temperature

RVC	reticulated vitreous carbon
SCE	saturated calomel electrode
SHE	standard hydrogen electrode
SNF	spent nuclear fuel
SOC	state of charge
SWCNT	single walled carbon nanotubes
T	temperature
t	time
T_1	relaxation time
TBP	tributyl phosphate
THF	tetrahydrofuran
THF-d_8	deuterated tetrahydrofuran
UREX	uranium extrication
UV-Vis	ultraviolet-visible
V	volt
ν	scan rate
W	watt
XPS	x-ray photoelectron spectroscopy
XRD	x-ray diffraction

Chapter 1 Introduction

1.1. Nuclear Power

1.1.1. Overview

Global climate change is the greatest threat currently facing our planet and is occurring at a faster rate than has previously been predicted.[1] One of the main drivers of global climate change is the emission of CO_2.[2] Year over year our global CO_2 emissions continue to grow, which has led to an increase in the atmosphere CO_2 concentration by 50% since the pre-industrial era.[3, 4] Our society has become heavily dependent on the combustion of fossil fuels for the generation of power that drives our modern world. To avoid the potentially deadly effects of climate change, we need to dramatically reduce our use of fossil fuels and convert to low CO_2 emission energy sources such as wind, solar and nuclear power. This switch needs to occur rapidly to avoid slipping past the point where we can no longer reverse the damage to our planet.[2]

Nuclear power is a key element in facilitating the shift away from fossil fuels. Generally nuclear power is considered a clean source of electricity because it does not directly produce carbon emissions when generating electricity.[5, 6] The only carbon emissions in nuclear power arise from the building/decommissioning of the facilities and production of nuclear fuel. These contributions are insignificant compared to the lifetime emissions from coal and natural gas plants.[7]

Globally, 443 reactors operational supply roughly 11% of all the electricity generated.[8] Several countries have proposed to build new reactors as a method to meet the Paris climate agreement, with 52 projects under construction.[8] The main concerns surrounding nuclear power plants are the potential for reactor failures and the disposal of spent nuclear fuel (SNF). Modern nuclear power plants have developed increased safety features that make them

significantly safer than original designs.[9, 10] The disposal and handling of SNF is highly regulated with most countries opting to store SNF in secured short and long-term storage facilities. A few countries, however, do reprocess SNF to extract uranium and plutonium before storage. [11, 12] Further advancement and adoption of these reprocessing systems would reduce the amount of SNF needed to be stored long-term.

1.1.2. Nuclear Fuel Cycle

The nuclear fuel cycle begins with extracting uranium from the earth by underground mining, open-pit mining, or *in-situ* solution (ISL) mining.[7] Uranium ore extracted from underground or open-pit mines is milled into a fine powder and leached to isolate a U_3O_8 solution. ISL mining skips these steps by leaching the U directly from the ground by pumping either sulfuric acid or carbonate solutions into U rich soil to directly extract a U_3O_8 solution. The leached solutions are then dried to form solid U_3O_8 called yellow cake. The U extracted from the ground naturally has a 0.7% ^{235}U percent composition. For use in the nuclear reactors in the U.S, it needs to be enrich to a 3-5% ^{235}U content – so called low-enriched uranium (LEU).[13] This is accomplished by converting the U_3O_8 into gaseous UF_6, which undergoes gas centrifugation to isolate the streams of enriched uranium (>0.7% ^{235}U) and depleted uranium (<0.7% ^{235}U).[7, 14] Once enriched, the UF_6 is convert to UO_2, compressed into pellets and assembled into rods. Bundles of these fuel rods are then loaded into reactors for use.

In the reactor, the fissile ^{235}U undergoes the fission chain reaction and produces much of the heat used to generate electricity. While the ^{238}U present in the fuel has a low fission probability, it can undergo neutron capture to form ^{239}U, which undergoes a β^- decay to ^{239}Np ($t_{1/2}$ = 23.5 min), which upon a second β^- decay ($t_{1/2}$ = 2.35 days) and generates ^{239}Pu – a radionucleus of major concern for nuclear weapons proliferation. Similar neutron capture

decay paths lead to the generation of transuranic products (Np, Pu, Am, and Cm). After 2-5 years, the majority of fissile ^{235}U is consumed and the spent fuel is removed from the reactors. The ^{238}U in the fuel is barely consumed and makes up ~95% of the SNF.[15] The rest of the SNF consists of 3-4% of fission products (Tc, Mo, I, Cs, Nd, Sm and others), 0.9% Pu, and 0.1% minor actinides (Np, Am, Cm).[15]

The SNF from the reactor continues to give off heat immediately after removal due to the fission products undergoing rapid α, β, and γ decay to more stable isotopes, thus needs to be stored in cooling pools for 5-10 years.[12] At this point the SNF is reprocessed or put directly into longer term storage.

The gold standard SNF reprocessing method is the Plutonium Uranium Redox EXtraction (PUREX) process (Figure 1.1). This process uses a biphasic liquid-liquid extraction to isolate both U and Pu from the fission and minor actinides products.[16] The first step is to dissolve the solid fuel rods in ~7 M nitric acid. An organic kerosene solution of tributyl phosphate (TBP) is mixed with the aqueous layer, extracting the uranyl (UO_2^{2+}) and Pu^{4+} into the organic phase. The Pu^{4+} is then subsequently isolated by adding a reducing agent to generate Pu^{3+} and extracted into a fresh aqueous phase. The UO_2^{2+} left in the kerosene is then back extracted into a dilute nitric acid solution. Recycling UO_2^{2+} for use in reactors a second time reduces the amount of high level waste (HLW) volume generated by up to 80%.[12] This lowers the space needed for long-term HLW storage as well as the amount of mining required to make new fuel rods.

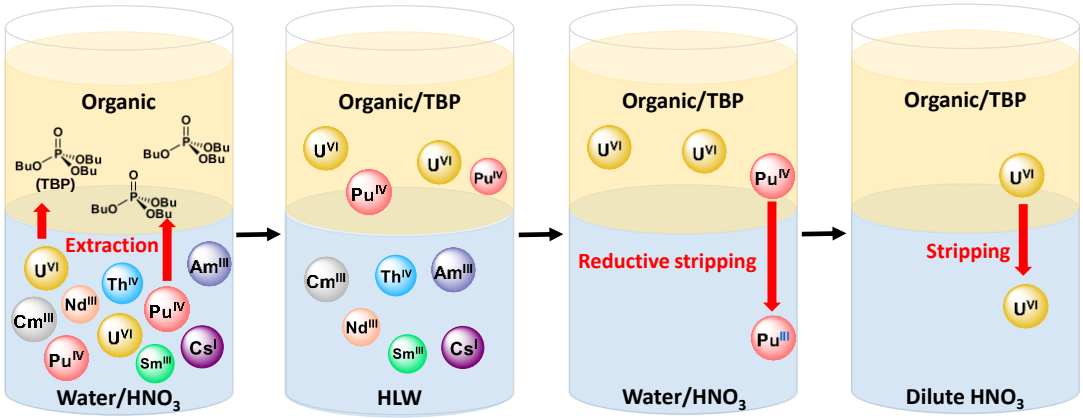

Figure 1.1: PUREX process

Many major global stakeholders, including the U.S., however do not use the PUREX process, due to the concerns of weapons proliferation from generating pure Pu streams.[17, 18] They instead use a once through approach to the nuclear fuel cycle, where the SNF is not reprocessed but stored as is, typically on-site in dry casks for 50-100 years, before it is deemed safe to transfer to a long-term storage site.[12]

The end of the nuclear fuel cycle is the same for both the once- and twice-through approaches, with the leftover waste being deposited into deep geological repositories for long-term storage. These sites are built into geologically stable area formations beneath groundwater with impervious rocks to abate liquid or gas contamination, bolstered by added engineered barriers.[19] Many of these sites are also engineered with removal in mind, as potential advancements to nuclear fuel cycle and reprocessing may make it advantageous to recycle the SNF in the future.[17]

1.2. Grid Energy Storage

1.2.1. Overview

Development of grid scale energy storage systems (ESS) contrasts sharply with nuclear power. These are systems used to store energy when demand is low and supply energy when demand is high or production is not possible.[20] This is especially important in a grid reliant on renewable energy sources such as wind and solar, which are intermittent in nature. Mismatches in electric supply and demand leads to curtailment at times of excessive supply, where energy production is cut back simply due to a lack of demand. The development and implementation of ESS will allow excess energy produced by green sources to be stored for later use rather than being curtailed.

The performance and economics of ESS plays a key role in their commercialization and widespread adoption. The capital cost, life cycle, and energy density are among the most important factors when developing an ESS. The cost per kilowatt hour of storage ($/kWh) is typically used as the benchmark for the capital costs of the system. The U.S. Department of Energy (DOE) target is $100/kWh for ESS wide-scale deployment.[21] The reliability and durability of ESS is an important factor for the lifetime cost of these systems, with a minimum goal of lasting 15 year and >4000 deep cycles of operation.[20] The energy density of these systems is on the lower end of importance for ESS systems, but does plays a role when implementing them in urban areas with limited space.

A variety of different energy storage methods have been demonstrated for ESS applications including physical (pumped hydro, compressed air, flywheels), thermal (molten salt), chemical (hydrogen), and electrochemical (batteries). [20, 22, 23] Pumped hydro currently provides the majority of grid energy storage capacity,[24] but electrochemical devices likely will

be the leading technology in the coming future as they are more scalable and versatile than pumped hydro and the other ESS.

1.2.2. Redox Flow Battery

Redox flow batteries (RFBs) are a highly configurable ESS with the advantage of decoupling the total power and total energy separate from each other.[25] This means that the energy output from the battery is scalable to the demand of the grid, separate from the storage capacity of the battery. This separation arises from using the potential difference of charge carriers dissolved in solution, rather than solid electrodes. The dissolved catholyte and anolyte charge carriers are stored in external reservoirs and pumped across flow field electrode to charge/discharge RFBs (Figure 1.2).[25] The storage capacity of RFBs can be scaled by altering the storage tank capacity, while the power output can be scaled by increasing the number/area of the electrodes.

Membranes are a major component of RFBs that play a major role in the stability and cost of the battery. They prevent the crossover of the charge carriers but allow for ion exchange between sides to balance charges. Crossover of the electrolyte species, anolyte to catholyte side and vice versa, must be prevented as it leads to reduced capacity and lifetime of batteries. The cation exchange membrane Nafion is a commonly used membranes in RFB that works well to prevent crossover, but is costly ranging from US$500-100/$m^2$.[26] This high cost can contribute up to 20% of the total battery cost of an RFB.[27]

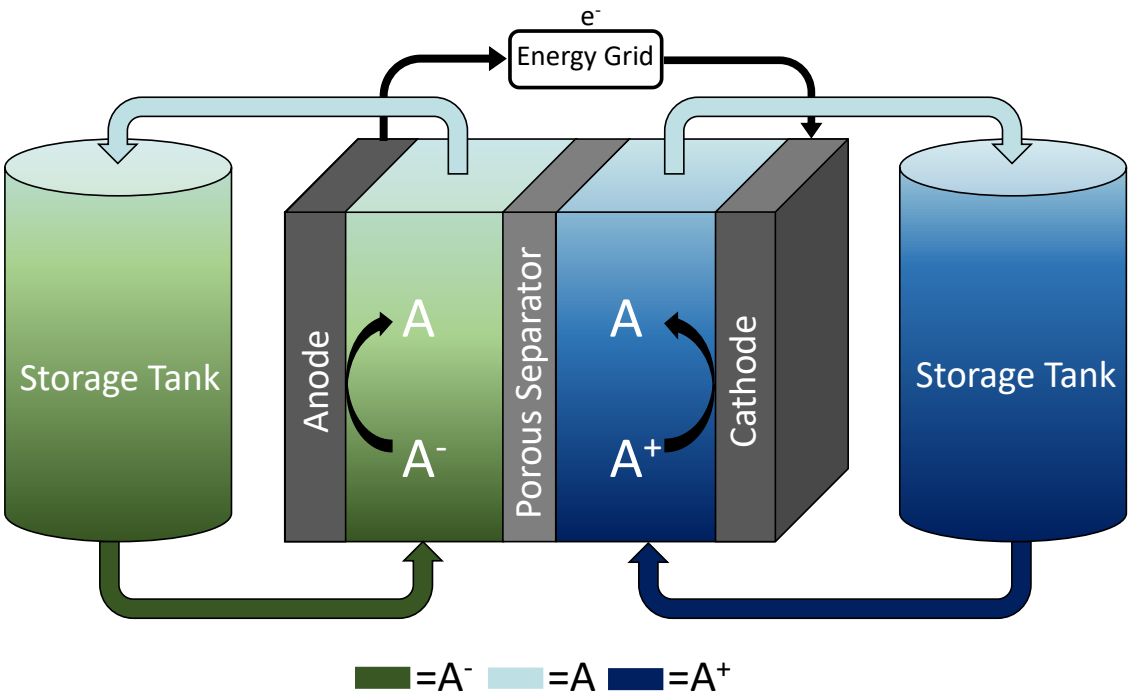

Figure 1.2: Symmetric Redox Flow Battery (RFB) scheme

Charge carriers play an even more critical role in RFBs stability, energy density, and cost. When choosing or designing charge carriers for RFB applications an important decision is deciding if a symmetric or non-symmetric charge carriers will be used.[25] Non-symmetric batteries use different charge carriers for the catholyte and anolyte, which affords the benefit of flexibility in choice of charge carriers but leaves them prone to capacity loss from crossover. Symmetric RFBs on the other hand, have the same charge carrier for both sides of the battery undergoing separate redox reactions (Figure 1.2). Since they serve as both the catholyte and anolyte, symmetric charge carriers need at least three stable different oxidation states that are soluble and have a significant difference in redox potential. Achieving these three requirements is difficult but results in a battery resilient to crossover. Crossover of symmetric charge carriers will cause short-term effects to the capacity of the battery, but the long-term effects can be mitigated in various ways. One method is to periodically mix the two

electrolyte tanks together to even out concentrations, regenerating the capacity of the battery.[28] Another method is to regularly reverse the polarity of the battery, by switching the anolyte side to serve as the catholyte side and vice versa.[29] This can mitigate crossover that occurs from chemical potential gradients.

Early RFB charge carrier research centered on metal and halogen ions, with the first modern RFB being developed by NASA in the early 1970's using an iron/chromium system.[30] This system used a non-symmetric approach with the Fe^{2+}/Fe^{3+} couple (0.77 V vs SHE) at the cathode and Cr^{2+}/Cr^{3+} couple (-0.41 V vs SHE) at the anode. The kinetics of the iron couple were fast, but the battery suffered from the slow kinetics of chromium redox. As a result, the chromium couple required either heat or an electro-catalyst to be used in a RFB. [25, 30] Solving this issue exposed a larger issue with the battery as the crossover of chromium into the iron side and vice versa led to degradation of the battery.

Currently, vanadium redox flow batteries (VRB) are among the most developed RFBs. VRBs use a symmetric approach with V^{4+}/V^{5+} couple (1 V vs SHE) at the cathode and V^{2+}/V^{3+} couple (-0.26 V vs SHE) at the anode.[25] VRBs have achieved MWh scale installations, but still have drawbacks preventing them from being fully economically viable.[31] The material cost of vanadium alone contributes ~$300/kWh to the total cost of the system, significantly higher than the DOE goals.[21] On top of that, low solubility of 2.0 M in acidic aqueous condition limits the energy density to 20-30 Wh/L.[30] The toxicity and corrosiveness of the VO^{+}/VO_2^{+} species is also of concern when scaled up to larger volumes.

1.3. Scope of Thesis

The main objective of this graduate research was the development redox active molecules that worked in tandem with conductive carbons. While reprocessing spent nuclear

fuel and redox flow batteries are drastically different, the redox active compounds for both systems utilized conductive carbon as both π-π stacking sources and paths of electron transfer to enhance their properties.

The first half of this work focuses on the selective capture of actinides from aqueous simulated SNF. In Chapter 2, the biphasic systems, previously developed by Megan Keener, Camden Hunt and Tim Carroll, was applied to an aqueous simulated SNF solution to measure *nido*-$^{PO}Cb^{2-}$ selectivity for UO_2^{2+} capture. I would like to acknowledge that Megan Keener started the selectivity work and did the majority of the synthesis and characterization data of the metal *nido*-$^{PO}Cb^{2-}$ complexes. My role in the project was to optimize conditions for the capture/release experiments and develop the ICP-OES analysis conditions for the simulated SNF solutions. In Chapter 3, I heterogenized the capture system by developing carborane (^{PO}Cb, ^{PO}Cb-Pyr) functionalized carbon electrodes. These electrodes demonstrated carborane based heterogeneous electrochemical behaviour and had the ability to selectively capture actinides out of aqueous solutions.

The second half of this work focuses on the development of symmetric charge carriers for RFB applications. In Chapter 4, various metal phthalocyanine complexes are demonstrated as stable charge carriers when paired with conductive carbon additives. I would like to acknowledge that Camden Hunt was the first to develop this system and Madeline Peterson contributed to the further development of the system. My work was centered on cycling and characterizing the commercially available unsubstituted metal phthalocyanines. In Chapter 5, we pursued metal cyclam complexes as solution based symmetric charge carrier but encountered stability issues with the Ni(+I) species.

At the time of writing this, portions of this thesis in Chapters 2 [32] and 4 [33, 34] are published and portions of Chapter 3 have been submitted for publication.[35]

1.4. References

(1) H.-O. Pörtner, D. C. R., M. Tignor, E.S. Poloczanska, K. Mintenbeck, A. Alegría, M. Craig, S. Langsdorf, S. Löschke, V. Möller, A. Okem, B. Rama. *Climate Change 2022: Impacts, Adaptation and Vulnerability*; Intergovernmental Panel on Climate Change, 2022. DOI: 10.1017/9781009325844.

(2) Masson-Delmotte, V., P. Zhai, A. Pirani, S.L. Connors, C. Péan, S. Berger, N. Caud, Y. Chen, L. Goldfarb, M.I. Gomis, M. Huang, K. Leitzell, E. Lonnoy, J.B.R.; Matthews, T. K. M., T. Waterfield, O. Yelekçi, R. Yu, and B. Zhou. *Climate Change 2021: The Physical Science Basis*; IPCC, 2021. DOI: 10.1017/9781009157896.

(3) *Global Energy Review* International Energy Agenecy, 2021. https://www.iea.org/reports/global-energy-review-2021.

(4) Hannah Ritchie, M. R., Pablo Rosado. CO_2 and Greenhouse Gas Emissions. *Our World in Data* **2020**.

(5) Nelson, A.-G. D.; Bray, T. H.; Stanley, F. A.; Albrecht-Schmitt, T. E. Periodic Trends in Actinide Phosphonates: Divergence and Convergence between Thorium, Uranium, Neptunium, and Plutonium Systems. *Inorg. Chem.* **2009**, *48* (10), 4530-4535. DOI: 10.1021/ic900484w.

(6) Rose, D. J. Nuclear Eclectic Power. *Science* **1974**, *184* (4134), 351-359. DOI: 10.1126/science.184.4134.351.

(7) *Nuclear explained*. Energy Information Administration 2022. https://www.eia.gov/energyexplained/nuclear/ (accessed.

(8) IAEA. *Nuclear Power and the Paris Agreement*. 2016. https://www.iaea.org/sites/default/files/16/11/np-parisagreement.pdf (accessed 2021 2/5/2021).

(9) Hannah Ritchie, M. R., Pablo Rosado. Energy. *Our World in Data* **2022**.

(10) *Safety of Nuclear Power Reactors*. World Nuclear Association 2022. (accessed.

(11) Ewing, R. C. Long-term storage of spent nuclear fuel. *Nat. Mater.* **2015**, *14* (3), 252-257. DOI: 10.1038/nmat4226.

(12) Rodríguez-Penalonga, L.; Moratilla Soria, B. Y. A Review of the Nuclear Fuel Cycle Strategies and the Spent Nuclear Fuel Management Technologies. In *Energies*, 2017; Vol. 10.

(13) Bruno, J.; Ewing, R. C. Spent Nuclear Fuel. *Elements* **2006**, *2* (6), 343-349. DOI: 10.2113/gselements.2.6.343 (acccessed 12/15/2022).

(14) Edwards, C. R.; Oliver, A. J. Uranium processing: A review of current methods and technology. *JOM* **2000**, *52* (9), 12-20. DOI: 10.1007/s11837-000-0181-2.

(15) Kumari, I.; Kumar, B. V. R.; Khanna, A. A review on UREX processes for nuclear spent fuel reprocessing. *Nucl. Eng. Des.* **2020**, *358*, 110410. DOI: https://doi.org/10.1016/j.nucengdes.2019.110410.

(16) Lanham, W. B.; Runion, T. C. *PUREX PROCESS FOR PLUTONIUM AND URANIUM RECOVERY*; United States, 1949. https://www.osti.gov/biblio/4165457 https://www.osti.gov/servlets/purl/4165457DOI: 10.2172/4165457

Other Information: Decl. with deletions Apr. 18, 1960. Orig. Receipt Date: 31-DEC-60.

(17) OECD. *The Economics of the Back End of the Nuclear Fuel Cycle*; 2014. DOI: doi:https://doi.org/10.1787/9789264208520-en.

(18) Glatz, J.-P. 6.11 - Spent Fuel Dissolution and Reprocessing Processes. In *Comprehensive Nuclear Materials (Second Edition)*, Konings, R. J. M., Stoller, R. E. Eds.; Elsevier, 2020; pp 305-326.

(19) OECD; Agency, N. E. *Advanced Nuclear Fuel Cycles and Radioactive Waste Management*; 2006. DOI: doi:https://doi.org/10.1787/9789264024861-en.

(20) Yang, Z.; Zhang, J.; Kintner-Meyer, M. C. W.; Lu, X.; Choi, D.; Lemmon, J. P.; Liu, J. Electrochemical Energy Storage for Green Grid. *Chem. Rev.* **2011**, *111* (5), 3577-3613. DOI: 10.1021/cr100290v.

(21) DOE. *Energy Storage Grand Challenge Cost and Performance Assessment 2020*; DOE/PA-0204; 2020. https://www.energy.gov/energy-storage-grand-challenge/downloads/2020-grid-energy-storage-technology-cost-and-performance.

(22) Venkataramani, G.; Parankusam, P.; Ramalingam, V.; Wang, J. A review on compressed air energy storage – A pathway for smart grid and polygeneration. *Renew. Sustain. Energy Rev.* **2016**, *62*, 895-907. DOI: https://doi.org/10.1016/j.rser.2016.05.002.

(23) Enescu, D.; Chicco, G.; Porumb, R.; Seritan, G. Thermal Energy Storage for Grid Applications: Current Status and Emerging Trends. In *Energies*, 2020; Vol. 13.

(24) Rehman, S.; Al-Hadhrami, L. M.; Alam, M. M. Pumped hydro energy storage system: A technological review. *Renew. Sustain. Energy Rev.* **2015**, *44*, 586-598. DOI: https://doi.org/10.1016/j.rser.2014.12.040.

(25) Weber, A. Z.; Mench, M. M.; Meyers, J. P.; Ross, P. N.; Gostick, J. T.; Liu, Q. Redox flow batteries: a review. *J. Appl. Electrochem.* **2011**, *41* (10), 1137-1164. DOI: 10.1007/s10800-011-0348-2.

(26) Janoschka, T.; Martin, N.; Martin, U.; Friebe, C.; Morgenstern, S.; Hiller, H.; Hager, M. D.; Schubert, U. S. An aqueous, polymer-based redox-flow battery using non-corrosive, safe, and low-cost materials. *Nature* **2015**, *527* (7576), 78-81. DOI: 10.1038/nature15746.

(27) Prifti, H.; Parasuraman, A.; Winardi, S.; Lim, T. M.; Skyllas-Kazacos, M. Membranes for Redox Flow Battery Applications. In *Membranes*, 2012; Vol. 2, pp 275-306.

(28) Luo, Q.; Li, L.; Wang, W.; Nie, Z.; Wei, X.; Li, B.; Chen, B.; Yang, Z.; Sprenkle, V. Capacity Decay and Remediation of Nafion-based All-Vanadium Redox Flow Batteries. *ChemSusChem* **2013**, *6* (2), 268-274, https://doi.org/10.1002/cssc.201200730. DOI: https://doi.org/10.1002/cssc.201200730 (acccessed 2023/03/29).

(29) Potash, R. A.; McKone, J. R.; Conte, S. M.; Abruña, H. c. D. On the Benefits of a Symmetric Redox Flow Battery. *J. Electrochem. Soc.* **2016**, *163*.

(30) Pan, F.; Wang, Q. Redox Species of Redox Flow Batteries: A Review. In *Molecules*, 2015; Vol. 20, pp 20499-20517.

(31) Minke, C.; Kunz, U.; Turek, T. Techno-economic assessment of novel vanadium redox flow batteries with large-area cells. *J. Power Sources* **2017**, *361*, 105-114. DOI: https://doi.org/10.1016/j.jpowsour.2017.06.066.

(32) Keener, M.; Mattejat, M.; Zheng, S.-L.; Wu, G.; Hayton, T. W.; Ménard, G. Selective electrochemical capture and release of uranyl from aqueous alkali, lanthanide, and actinide mixtures using redox-switchable carboranes. *Chem. Sci.* **2022**, *13* (12), 3369-3374, 10.1039/D1SC07070C. DOI: 10.1039/D1SC07070C.

(33) Hunt, C.; Mattejat, M.; Anderson, C.; Sepunaru, L.; Ménard, G. Symmetric Phthalocyanine Charge Carrier for Dual Redox Flow Battery/Capacitor Applications. *ACS Appl. Energy Mater.* **2019**, *2* (8), 5391-5396. DOI: 10.1021/acsaem.9b01317.

(34) Mattejat, M.; Peterson, M.; Chakraborty, A.; Ménard, G. Dyeing to Carry Charge: Commercial Phthalocyanine Dyes as Charge Carriers for Redox Flow Battery Applications. *Energy Fuels* **2023**, *37* (1), 785-790. DOI: 10.1021/acs.energyfuels.2c03389.

(35) Mattejat, M. Selective heterogeneous capture and release of actinides using carborane-functionalized electrodes. *Chemcomm* **2023** *Submitted*.

Chapter 2 Selective Biphasic Uranyl Extraction

2.1. Introduction

2.1.1. Selective Uranyl Recycling from Spent Nuclear Fuel

The SNF from nuclear reactors contains approximately 95% uranium, making up the majority of the volume and mass of SNF.[1] This uranium present in SNF can be recycled and reused in nuclear reactors again. Recycling the uranium significantly reduces the amount of nuclear waste needed to be stored long-term, as well as the long-term disposal of radioactive waste. Additionally, U is a finite resource on our planet with the terrestrially available U deposits predicated to be depleted in a century at our current consumption rates or as soon as 40 years if demand increases.[2] Recycling U from SNF can significantly reduce the need for mining, preserving the longevity of the resource and lowering the environmental impact of manufacturing the fuel.[3]

To recycle uranium, it must be isolated from the 4% fission products, 0.9% plutonium and 0.1% minor actinides also present in SNF.[1] The standard industrial method is the PUREX process, which was developed in the U.S. during the 1950's but is now only used by France, India and Russia.[4] The PUREX process is not globally used due to the concerns of nuclear weapon proliferation that could occur from the generation of pure Pu streams.[5, 6] This has led for a push for the development of extraction process that solely isolate uranium. The U.S. initiated in 2006 the Global Nuclear Energy Partnership (GNEP), now called International Framework for Nuclear Energy (IFNEC), to advance the development and deployment of nuclear fuel cycle technologies that reduce the threat of proliferation.[7]

The UREX (URanium EXtraction) process was develop to isolate U from SNF while leaving Pu behind.[1] The UREX process starts in the same way as the PUREX by dissolving the fuel rods in nitric acid, but differs with the rest of the steps. Instead of adding a TBP

kerosene solution, a TBP n-dodecane solution is layered on top of the nitric acid solution extracting U and technetium (Tc).[8] Complexant and reductant agents are added to prevent the extraction of Pu and Np to the organic phase. Tc is subsequently stripped form the organic solution using high concentrations of nitric acid. The U is then isolated into a fresh aqueous phase by adding dilute nitric acid. Variations of the UREX process and other similarly related processes have been developed, but none have become economically viable due to their cost and complexity.[1, 9-12] Improved systems that are able to solely isolate U from SNF that are cost effective still need to be developed.

2.1.2. Uranyl Capture and Release using Redox-Switchable Carboranes

Carboranes are well-studied polyhedral structures that contain electron delocalized covalent bonding networks with boron, carbon, and hydrogen atoms.[13, 14] They have a wide variety of applications such as in medicine, nanoscale engineering, luminescence, energy storage, and radioactive waste recovery.[13, 15, 16] Icosahedral carborane structures are known to be very stable and have interesting electrochemical properties. The icosahedral $C_2B_{10}H_{12}$ carborane has three isomers based on the carbon positions being *ortho*, *meta* or *para* to each other. Carboranes can be denoted as *closo* or *nido* depending on the structure and framework electrons. *Closo* denotes a carborane that is a closed polyhedron with all the faces being triangular. *Nido* on the other hand denotes a carborane missing one of the vertices from the structure. The clusters geometry can also be explained by the relationship between the number of electrons involved in the bonding of the clusters framework, i.e. framework electrons, and the number of vertices the cluster has, *n*. If the cluster has $2n+2$ framework electrons it is a *closo*-polyhedron, while if it has $2n+4$ framework electrons the structure will be *nido*. The *closo-ortho*-$B_{10}C_2H_{12}$ carborane can undergo a two electron reduction that will break the C–

C bond to form the *nido*-anion.[13, 17] The *nido-ortho*-$B_{10}C_2H_{12}$ can be oxidized back the *closo-ortho*-$C_2B_{10}H_{12}$. Our group hypothesized this reversible structural change could be used for capture and release of metals of interest.

Our group tested this theory with UO_2^{2+} coordination first, as a mechanism for potential SNF reprocessing.[18] Diphenyl phosphine oxide groups were attached to both of the carbon positions on *ortho*-$C_2B_{10}H_{12}$ to synthesize 1,2-$(Ph_2PO)_2$-1,2-$C_2B_{10}H_{10}$ (**^{PO}Cb**). Phosphine oxide moieties are known to be high affinity ligating groups for UO_2^{2+} and are used in most reprocessing systems.[1, 4, 19] Cyclic voltammetry (CV) showed that the two electron reduction to *nido*-**^{PO}Cb^{2-}** and subsequent oxidation back *closo*-**^{PO}Cb** was quasi-reversible with a reduction potential of -0.994 V vs Fc/Fc^+ in acetonitrile (MeCN). **^{PO}Cb^{2-}** was also chemically synthesized by using decamethylcobaltocene and shown to coordinate in a 2:1 and 1:1 fashion with UO_2^{2+} (Figure 2.1). *In-situ* capture and release were demonstrated by electrochemically generating the **^{PO}Cb^{2-}** in the presence of UO_2^{2+} and tracking the products by ^{31}P NMR spectroscopy. UO_2^{2+} was released by electrochemical oxidation back to **^{PO}Cb**.

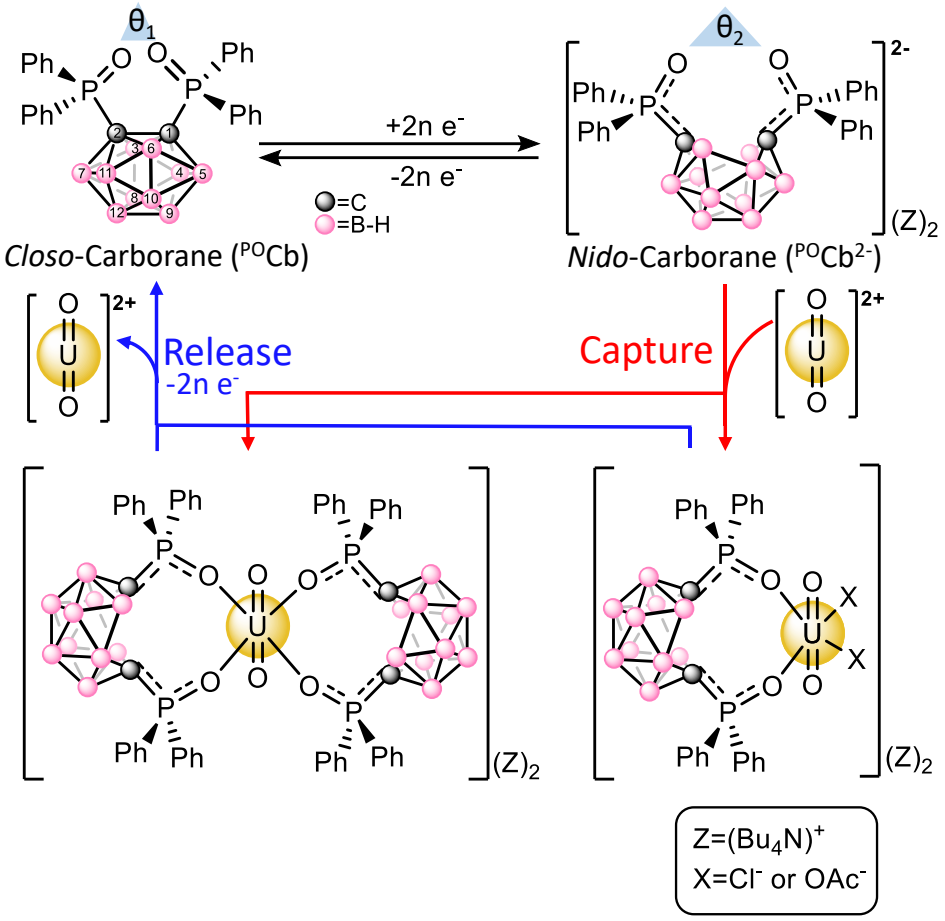

Figure 2.1: Scheme for UO_2^{2+}capture and release with ^{PO}Cb

A biphasic extraction system, similar to the PUREX and UREX systems, was then demonstrated using the redox-switchable **^{PO}Cb** (Figure 2.2). [18] UO_2^{2+} dissolved in a NaOAc-buffered aqueous solution was extracted into an organic dichloroethane (DCE) phase containing an electrochemically generated **^{PO}Cb^{2-}**. The loss of UO_2^{2+} in the aqueous layer was tracked by UV-Vis spectroscopy. The organic layer was then electrochemically oxidized to regenerate the **^{PO}Cb**, releasing the UO_2^{2+}. The released UO_2^{2+} was subsequently back extracted into a fresh NaOAc-buffered aqueous solution, its presence confirmed by UV-Vis spectroscopy.

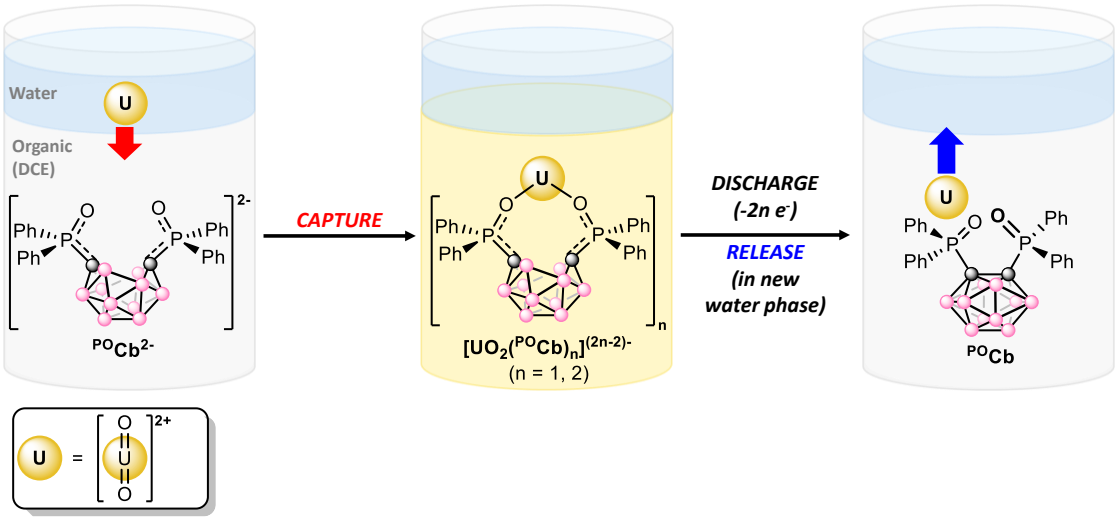

Figure 2.2: Biphasic extraction of UO_2^{2+} with ^{PO}Cb

We wanted to explore if the biphasic system using the **$^{PO}Cb^{2-}$** was selectve for UO_2^{2+} from an mixed aqueous solution of alkali, lanthanide, and actinide metals closely mimicking SNF streams. The choice of metals, and the reasons for using each, are as follows: 1) natural abundance $^{133}Cs^{+}$ (100%) was used to mimic the highly radiotoxic ^{137}Cs isotope which is responsible for much of the human health, environmental, and hot SNF disposal issues[20-22]; 2) Nd^{3+} and Sm^{3+} were chosen due to their abundance in SNF[21] and as lanthanide analogs to U and Pu, respectively[23-25]; 3) Th^{4+} was used also due to its abundance in SNF,[21] and because it functions as a Pu^{4+} surrogate in light of our inability to handle this highly controlled element in house.[26-28] Herein, we describe both the coordination chemistry of **$^{PO}Cb^{2-}$** to these individual metals, as well as the highly selective electrochemical capture of UO_2^{2+} with **$^{PO}Cb^{2-}$** from the mixed-metal aqueous solution to an organic phase. The electrochemical release of UO_2^{2+} to a fresh aqeous layer is also described (Figure 2.3).

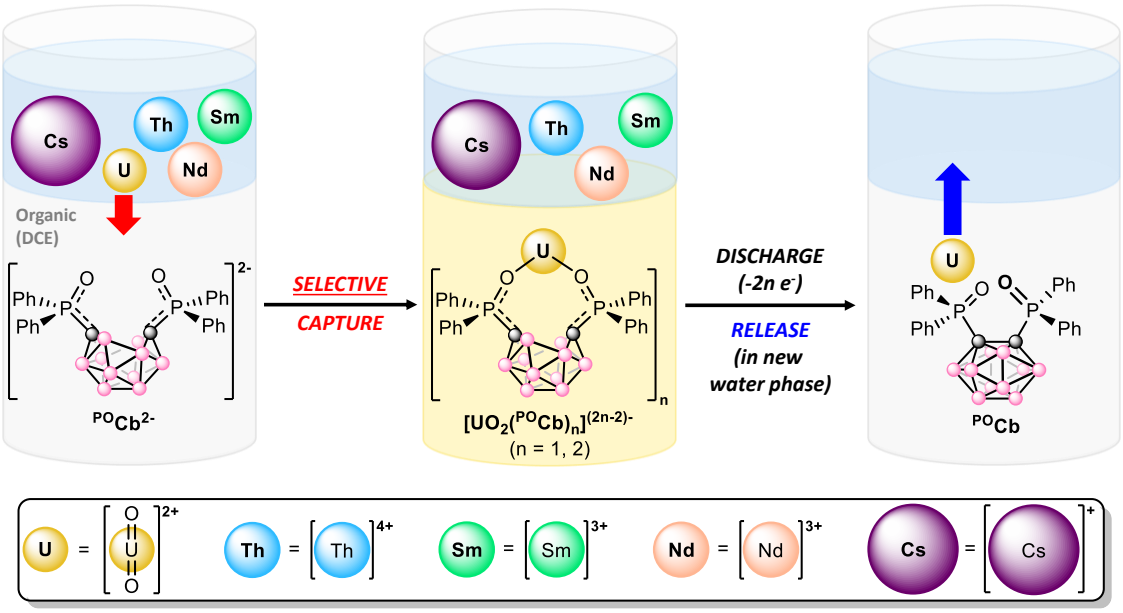

Figure 2.3: Selective biphasic extraction of UO_2^{2+} from simulated spent nuclear fuel

2.2. Results and Discussion

2.2.1. Synthesis and Characterization

Much of the synthetic and characterization work for this project was conducted by Megan Keener. I synthesized both the **[CoCp*$_2$]$_3$[Nd(^{PO}Cb)$_3$]** and **[CoCp*$_2$]$_2$[Th(^{PO}Cb)$_3$]** to acquire the EAs for both structures and the solid-state crystal structure for **[CoCp*$_2$]$_3$[Nd(^{PO}Cb)$_3$]**.

The coordination chemistry of the ^{PO}**Cb**$^{2-}$ ligand was investigated using the previously reported [CoCp*$_2$]$^+$ salt, **[CoCp*$_2$]$_2$[^{PO}Cb]** (Cp* =η^5-C_5Me_5),[18] in tandem with the nitrate salts of Cs^+, Nd^{3+}, Sm^{3+}, and Th^{4+}. All complexes were synthesized following an analogous synthetic procedure in MeCN. The Cs complex was generated by addition of an equimolar solution of **[CoCp*$_2$]$_2$[^{PO}Cb]** to a solution of $CsNO_3$ in MeCN at r.t. Following the selective recrystallization and separation of the [CoCp*$_2$][NO_3] byproduct, the desired product was

isolated and unambiguously identified by single crystal X-ray diffraction (XRD) studies as the dimeric salt, **[[CoCp*$_2$][Cs(^{PO}Cb)]]$_2$** (Figure 2.4a). The symmetric dimer features a central diamond-shaped core structure with two Cs atoms at the apical positions held in place by oxide donors from each ligand (Cs1–O(1, 1′) = 2.9893(18), 3.0844(19) Å), as well as Cs–H–B bonds[29, 30] (Cs1–B(3, 3′) = 3.681(3), 3.631(3) Å; Cs1–H(3, 3′) = 2.924, 3.08(3) Å). Other interactions outside the diamond core are provided by the additional oxide donor (Cs1–O2 = 2.9356(18) Å), as well as an additional B contact (Cs1–B4′ = 3.726(3) Å). We note that a Cs–H (3.199 Å) contact arising from a phenyl *meta*-C–H bond of an adjacent dimer is also observed, generating a polymeric structure (Figure 2.4b). The *nido* **^{PO}Cb^{2-}** ligand charged state is maintained as indicated by the long C1–C2 distance (2.862 Å),[18] which is well outside the range of a C–C bond. Together, we tentatively assign a coordination number (CN) of 9 to the large Cs cation. Due to its symmetry, identical bond metrics are found for Cs1′. The bonding types and lengths, the polymeric structure, and the assigned CN are similar to previously reported data.[29-32] Lastly, while the solid-state structure displays inequivalent P=O donor groups in the **^{PO}Cb^{2-}** ligands, we note that the diamagnetic complex displays a single resonance in the ^{31}P NMR spectrum at 31.7 ppm in MeCN-d_3 indicating higher symmetry in solution, perhaps due to the breakup of the polymeric structure initiated by the coordinating solvent.

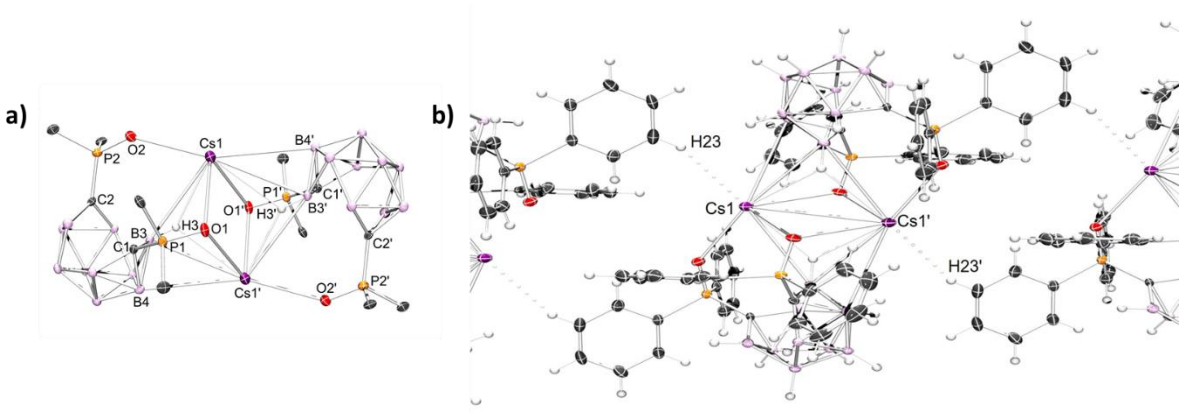

Figure 2.4: Solid-state molecular structures obtained by XRD studies of: a) $[[CoCp^{*}_{2}][Cs(^{PO}Cb)]]_2$ with **[**$CoCp^{*}_{2}]^+$ counter cations, co-crystallized solvent molecules, and all H atoms omitted for clarity b) $[[CoCp^{*}_{2}][Cs(^{PO}Cb)]]_2$ displaying polymeric structure through long Cs1-H23 contacts (3.199 Å). $[CoCp^{*}_{2}]^+$ counter cations are omitted for clarity.

The lanthanide (Nd^{3+}, Sm^{3+}) and actinide (Th^{4+}) complexes were next synthesized using an identical procedure. Three equivalents of **$[CoCp^{*}_{2}]_2[^{PO}Cb]$** were added to one equivalent of $M(NO_3)_n$ (M = Nd, Sm (n = 3); Th (n = 4)) in MeCN at r.t. The $[CoCp^{*}_{2}][NO_3]$ byproduct was again selectively crystallized and separated prior to isolation of the final products, which were all unambiguously identified by single crystal XRD studies as: **$[CoCp^{*}_{2}]_3[Nd(^{PO}Cb)_3]$** (Figure 2.5a); **$[CoCp^{*}_{2}]_3[Sm(^{PO}Cb)_3]$** (Figure 2.5b), and; **$[CoCp^{*}_{2}]_2[Th(^{PO}Cb)_3]$** (Figure 2.5c). All complexes have a central 6-coordinate metal center in pseudo-octahedral geometries. Average M–O bond distances of 2.327 Å (Nd), 2.315 Å (Sm), and 2.297 Å (Th) are similar to reported values[33-39] and follow an expected periodic trend based on decreasing ionic radii and increasing ionic charge (for Th). Long carborane C–C distances (average 2.86 Å) in each case are again indicative of a *nido* $^{PO}Cb^{2-}$ configuration.[18] The solid-state structure of the previously reported UO_2^{2+} complex, $[CoCp^{*}_{2}]_2[UO_2(^{PO}Cb)_2]$, is also shown in Figure 2.5d as a comparison to the new complexes reported here.

Spectroscopically, both lanthanide complexes, $[CoCp^{*}_{2}]_3[Nd(^{PO}Cb)_3]$ and $[CoCp^{*}_{2}]_3[Sm(^{PO}Cb)_3]$, display ^{31}P NMR resonances at 140.6 and 27.9 ppm, respectively. These values are notably different from each other, likely due to varying paramagnetism, as well as from the diamagnetic $[CoCp^{*}_{2}]_2[Th(^{PO}Cb)_3]$ (51.3 ppm) and $[CoCp^{*}_{2}]_2[UO_2(^{PO}Cb)_2]$ (52.0 ppm) complexes.[18]

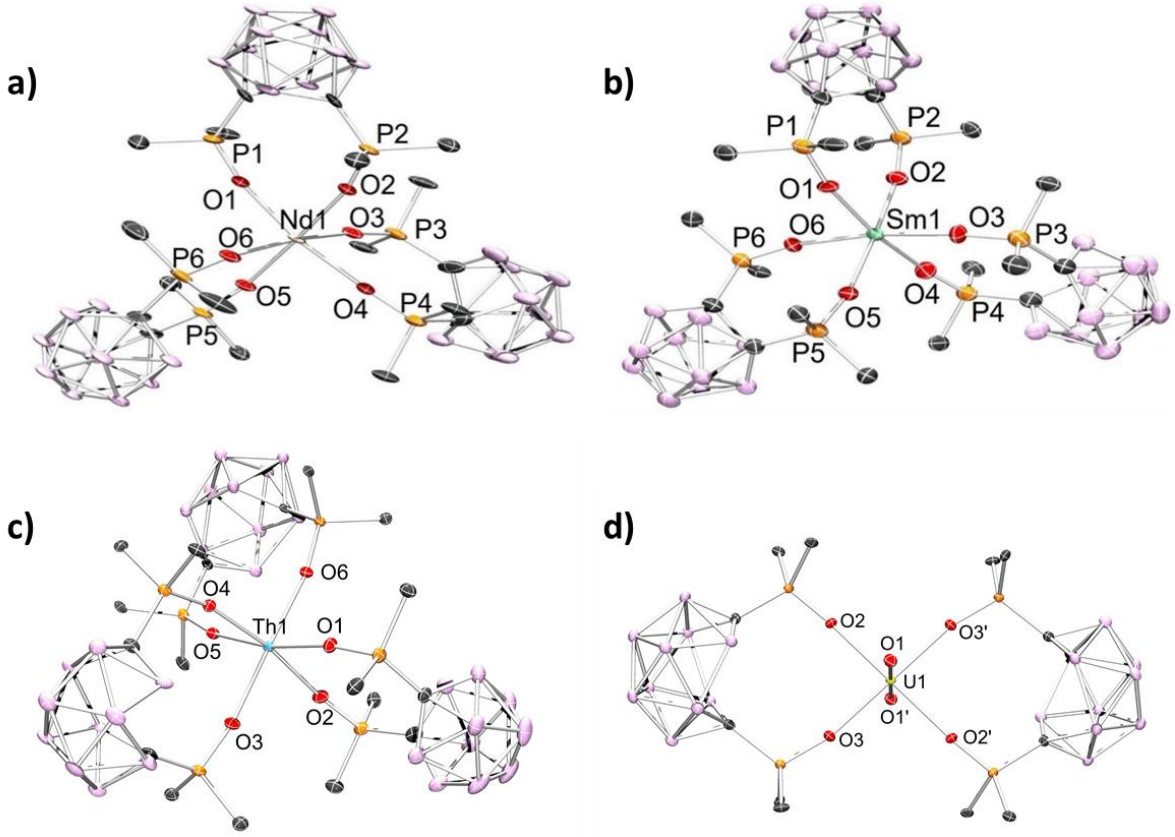

Figure 2.5: Solid-state molecular structures obtained by XRD studies of: a) $[CoCp^{*}_{2}]_3[Nd(^{PO}Cb)_3]$; b) $[CoCp^{*}_{2}]_3[Sm(^{PO}Cb)_3]$; c) $[CoCp^{*}_{2}]_2[Th(^{PO}Cb)_3]$, and; d) $[CoCp^{*}_{2}]_2[UO_2(^{PO}Cb)_2]$.[18] $[CoCp^{*}_{2}]^{+}$ counter cations, phenyl C–H linkages, co-crystallized solvent molecules, and all H atoms omitted for clarity.

2.2.2. Biphasic Extraction

Building on our previous work (Figure 2.1),[18] we investigated the selective electrochemical capture of UO_2^{2+} from mixed aqueous alkali (Cs^+), lanthanide (Nd^{3+}, Sm^{3+}), and actinide (Th^{4+}, UO_2^{2+}) solutions mimicking in part SNF.[40] Mixed-metal aqueous stock solutions were first prepared by dissolving equimolar quantities of $CsNO_3$, $Nd(NO_3)_3(THF)_3$, $Sm(NO_3)_3(THF)_3$, $Th(NO_3)_4(H_2O)_x$, and $UO_2(NO_3)_2(THF)_2$ in Milli-Q deionized water either with a NaOAc buffer (0.5 M, pH = 5.2) or without (pH = 2.6). The use of a buffer in the former was used for two reasons: 1) to mimic our previous results which required the use of a buffer to control for the pH-dependent extinction coefficient (ε) of UO_2^{2+} which was previously monitored by UV-Vis spectroscopy,[18, 41, 42] and; 2) to compare the extraction efficacy of our system at varying pH values. In contrast to our previous work, [18] we used inductively-coupled plasma optical emission spectrometry (ICP-OES) to directly, and more accurately, measure trace metal concentrations in the aqueous phases pre-extraction (pre-X), post-extraction (post-X), and following back-extraction (back-X) of UO_2^{2+} (*vide infra*).

Three separate 1,2-dichloroethane (DCE) solutions were next loaded with **^{PO}Cb** (1 equiv), $[PPN][PF_6]$ (0.5 equiv; $[PPN]^+ = [Ph_3P{=}N{=}PPh_3]^+$) as internal standard for NMR spectroscopy (*vide infra*), and $[Bu_4N][PF_6]$ (0.1 M) as supporting electrolyte and were loaded into one of two compartments of divided H-cells. Each counter compartment was loaded with a heterogeneous carbon additive (Ketjenblack) which served as a capacitive buffer[18, 43] and which was mixed in DCE with 0.1 M $[Bu_4N][PF_6]$. All H-cells were configured with physical glass-frit separators and contained reticulated vitreous carbon electrodes on each side (Figure 2.6). We note that each of these experiments were run in triplicate.

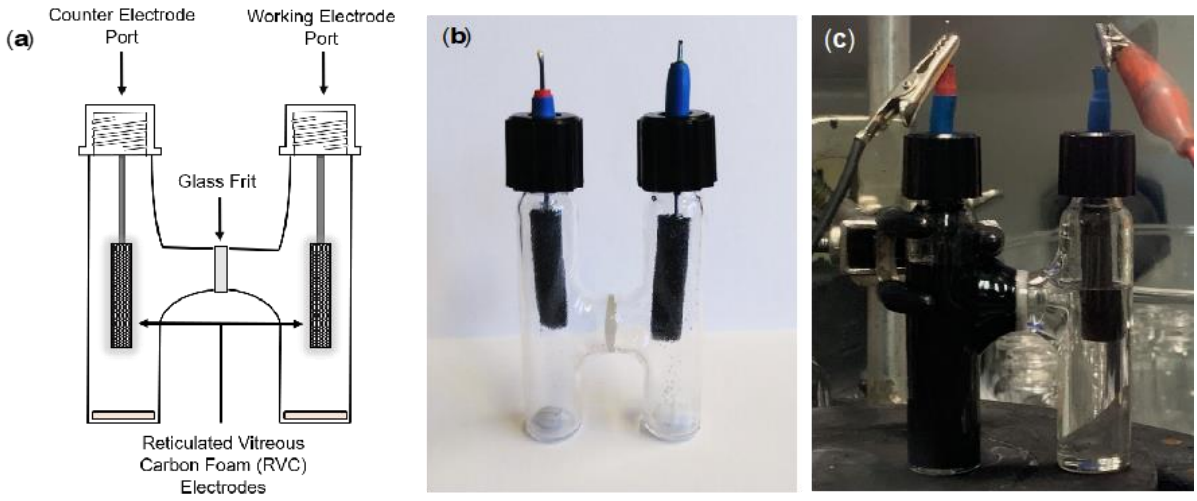

Figure 2.6: H-Cell design. (a) Schematic of the two-compartment H-cell used for the biphasic electrochemical separation and recovery of UO_2^{2+}. (b) Picture of the two-compartment H-cell used for the biphasic electrochemical separation and recovery of UO_2^{2+}. (c) Experimental setup of H-cell (before charging) used for the biphasic separation and recovery.

The ^{PO}**Cb** solutions were electrochemically reduced by galvanostatic bulk electrolysis (GBE) to a theoretical state-of-charge (SOC) of ca. 77% assuming a 100% coulombic efficiency (Figure 2.7). Subsequent analyses of the carborane solutions by unlocked $^{31}P\{^{1}H\}$ NMR spectroscopy revealed the clean conversion of ^{PO}**Cb** to the reduced *nido*-carborane, ^{PO}**Cb**$^{2-}$, each in approximate 76% yield and in line with the SOC (Figure 2.8-10). We note a loss of ca. 10% of combined carborane resonances (^{PO}**Cb** and ^{PO}**Cb**$^{2-}$) following charging and relative to the starting solutions and internal standard, perhaps due to unknown electrochemical side reactions.

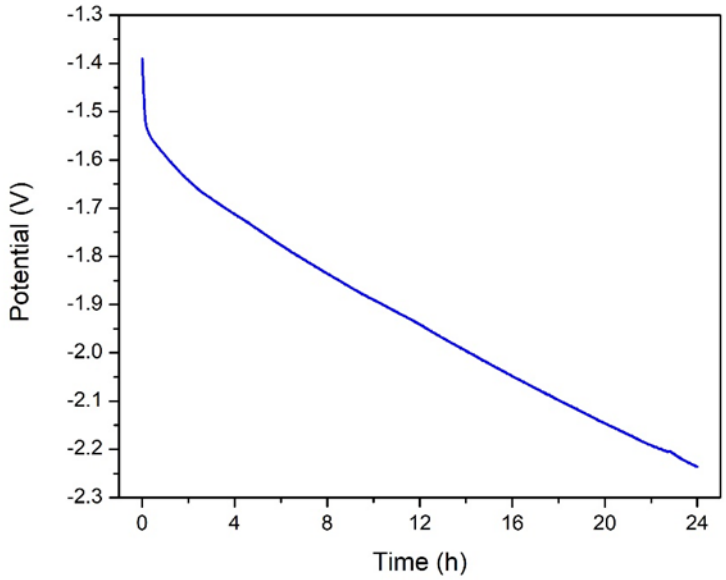

Figure 2.7: Charging curve for the electrochemical capture of UO_2^{2+}. A charging current of -107.1 μA was applied for a total of -9.25 C of charge transferred, resulting in a 76% SOC after 24 h assuming 100% columbic efficiency.

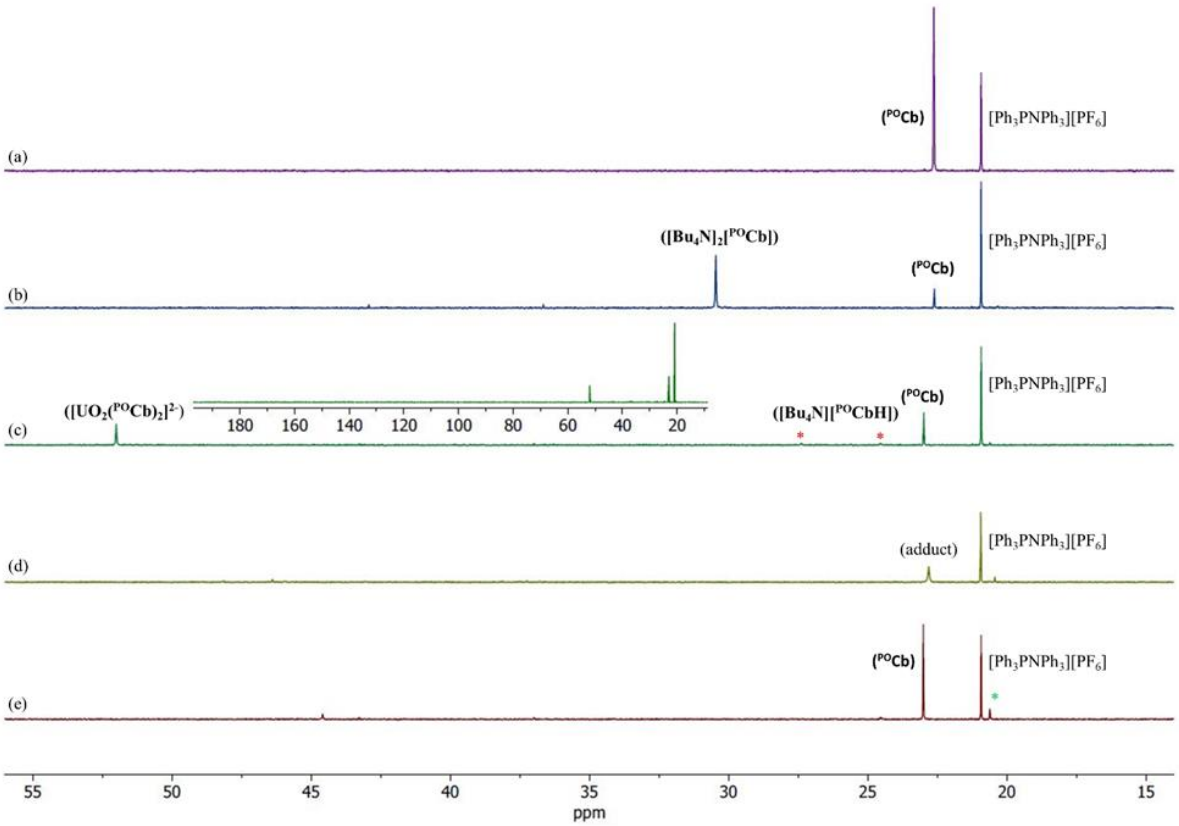

Figure 2.8: $^{31}P\{^{1}H\}$ NMR spectra for the electrochemical capture and release of UO_2^{2+} from a 1.25 equiv mixed metal aqueous solution. (a) Initial unlocked $^{31}P\{^{1}H\}$ NMR spectrum of ^{PO}Cb and $[Ph_3PNPPh_3][PF_6]$ in DCE. (b) $^{31}P\{^{1}H\}$ NMR spectrum of the DCE layer following GBE charging generating the reduced $[^{PO}Cb]^{2-}$ and some residual ^{PO}Cb. (c) $^{31}P\{^{1}H\}$ NMR spectrum of DCE layer following the selective UO_2^{2+} capture from the aqueous layer containing $UO_2(NO_3)_2(THF)_2$, $Th(NO_3)_4{\bullet}H_2O$, $Nd(NO_3)_3THF_3$, $Sm(NO_3)_3THF_3$, and $CsNO_3$ (pH = 2.6), indicating the formation of $[UO_2(^{PO}Cb)_2]^{2-}$, as well as some minor ^{PO}Cb and $[Bu_4N][^{PO}CbH]$ (denoted as *****). No resonances attributable to the captured metal anions, $[Cs(^{PO}Cb)]^-$ (31.7 ppm), $[Nd(^{PO}Cb)_3]^{3-}$ (140.6 ppm), $[Sm(^{PO}Cb)_3]^{3-}$ (27.9 ppm), or $[Th(^{PO}Cb)_3]^{2-}$ (51.3 ppm), are observed (inset). (d) $^{31}P\{^{1}H\}$ NMR spectrum of the DCE layer following GBE discharging revealing a very broad resonance at 23 ppm which we attribute to

an adduct of UO_2^{2+} with ^{PO}Cb.[18] (e) $^{31}P\{^1H\}$ NMR spectrum of the DCE layer following UO_2^{2+} release by mixing with Milli-Q water after 15 h and revealing the free carborane **^{PO}Cb** (major), as well as an unknown by-product at 20 ppm, marked by *.

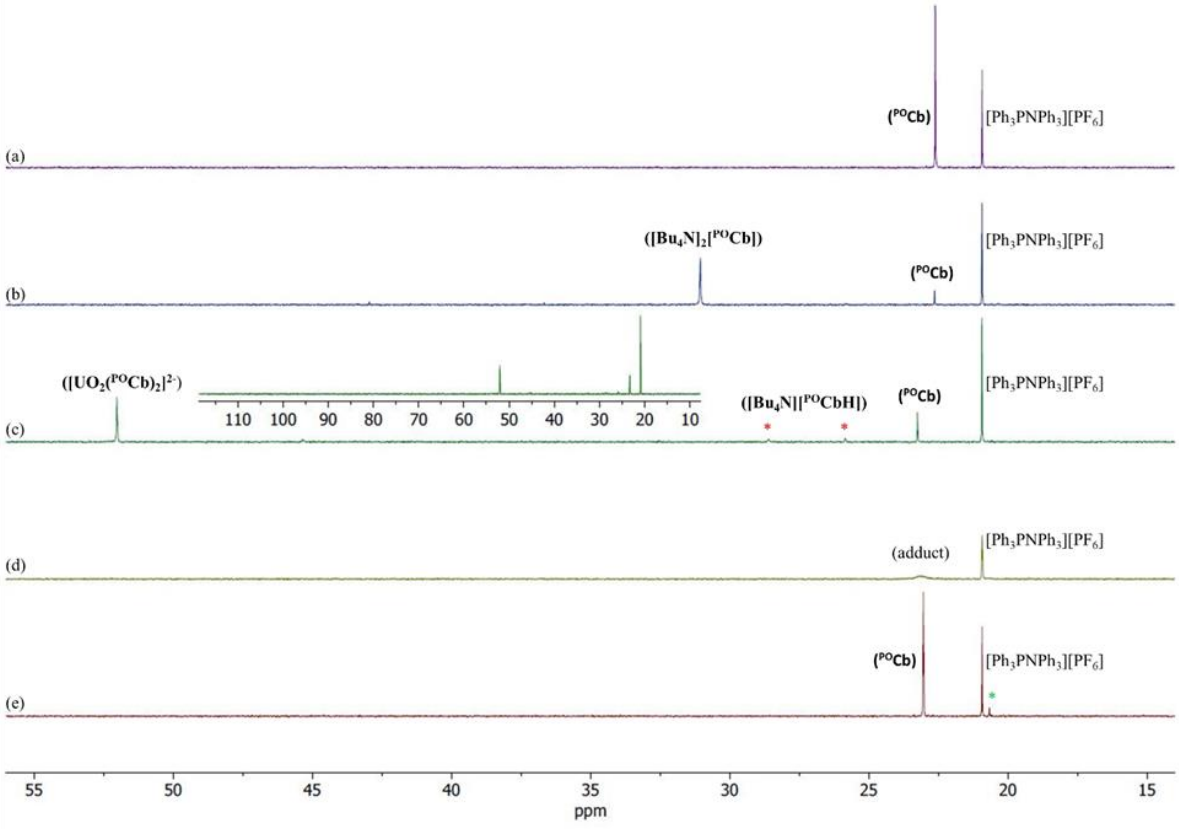

Figure 2.9: $^{31}P\{^1H\}$ NMR spectra for the electrochemical capture and release of UO_2^{2+} from a 1.25 equiv mixed metal buffered aqueous solution. (a) Initial unlocked $^{31}P\{^1H\}$ NMR spectrum of ^{PO}Cb and $[Ph_3PNPPh_3][PF_6]$ in DCE. (b) $^{31}P\{^1H\}$ NMR spectrum of the DCE layer following GBE charging generating the reduced $[^{PO}Cb]^{2-}$ and some residual ^{PO}Cb. (c) $^{31}P\{^1H\}$ NMR spectrum of DCE layer following the selective UO_2^{2+} capture from the aqueous layer containing $UO_2(NO_3)_2(THF)_2$, $Th(NO_3)_4{\bullet}H_2O$, $Nd(NO_3)_3THF_3$, $Sm(NO_3)_3THF_3$, and $CsNO_3$ in 0.5 M NaOAc buffer (pH = 5.4), indicating the formation of $[UO_2(^{PO}Cb)_2]^{2-}$, as well as some minor ^{PO}Cb and $[Bu_4N][^{PO}CbH]$ (denoted as *). No resonances attributable to the

captured metal anions, $[Cs(^{PO}Cb)]^-$ (31.7 ppm), $[Nd(^{PO}Cb)_3]^{3-}$ (140.6 ppm), $[Sm(^{PO}Cb)_3]^{3-}$ (27.9 ppm), or $[Th(^{PO}Cb)_3]^{2-}$ (51.3 ppm), are observed (inset). (d) $^{31}P\{^1H\}$ NMR spectrum of the DCE layer following GBE discharging revealing a very broad resonance at 23 ppm which we attribute to an adduct of UO_2^{2+} with ^{PO}Cb.[18] (e) $^{31}P\{^1H\}$ NMR spectrum of the DCE layer following UO_2^{2+} release by mixing with fresh NaOAc buffered solution (0.1 M) after 15 h and revealing the free carborane ^{PO}Cb (major), as well as an unknown by-product at 20 ppm, marked by *.

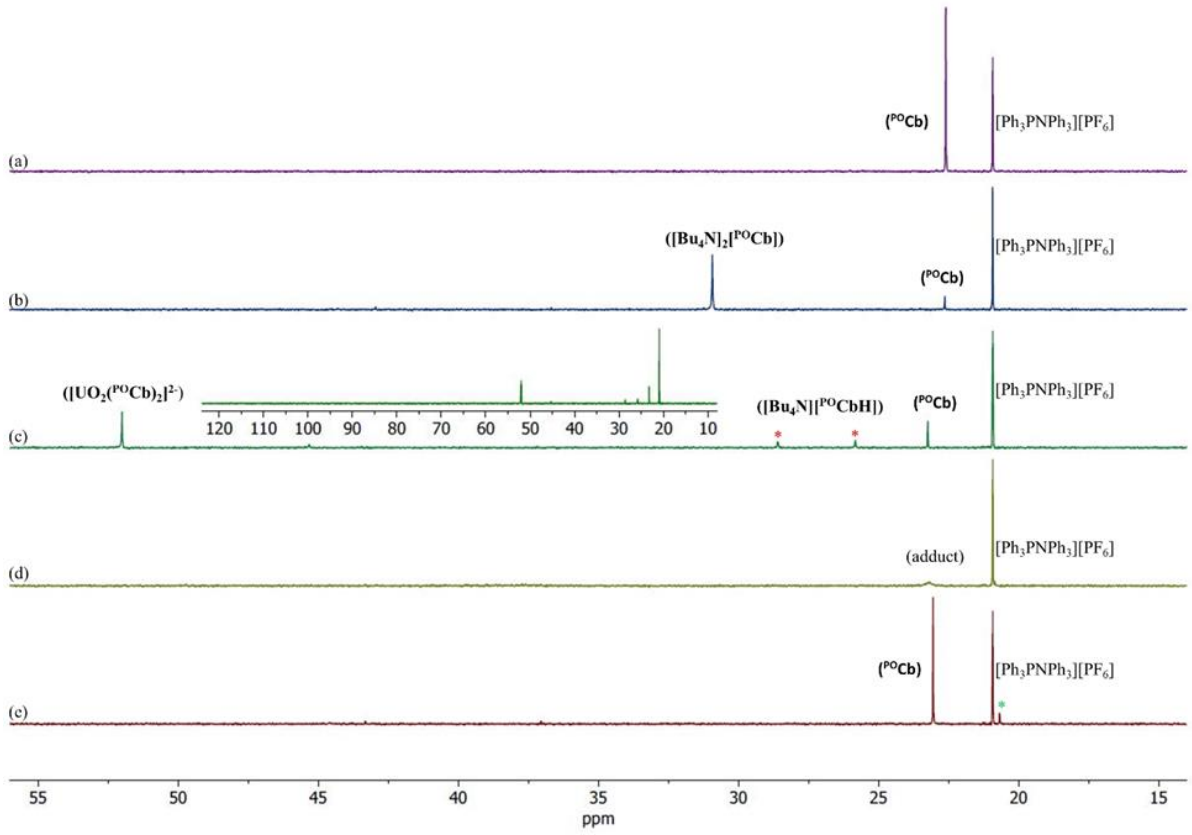

Figure 2.10: $^{31}P\{^1H\}$ NMR spectra for the electrochemical capture and release of UO_2^{2+} from a 0.6 equiv mixed metal buffered aqueous solution. (a) Initial unlocked $^{31}P\{^1H\}$ NMR spectrum of ^{PO}Cb and $[Ph_3PNPPh_3][PF_6]$ in DCE. (b) $^{31}P\{^1H\}$ NMR spectrum of the DCE layer following GBE charging generating the reduced $[^{PO}Cb]^{2-}$ and some residual ^{PO}Cb. (c)

$^{31}P\{^{1}H\}$ NMR spectrum of DCE layer following the selective UO_2^{2+} capture from the aqueous layer containing $UO_2(NO_3)_2(THF)_2$, $Th(NO_3)_4 \bullet H_2O$, $Nd(NO_3)_3THF_3$, $Sm(NO_3)_3THF_3$, and $CsNO_3$ in 0.5 M NaOAc buffer (pH = 5.4), indicating the formation of $[UO_2(^{PO}Cb)_2]^{2-}$, as well as some minor ^{PO}Cb and $[Bu_4N][^{PO}CbH]$ (denoted as *****). No resonances attributable to the captured metal anions, $[Cs(^{PO}Cb)]^-$ (31.7 ppm), $[Nd(^{PO}Cb)_3]^{3-}$ (140.6 ppm), $[Sm(^{PO}Cb)_3]^{3-}$ (27.9 ppm), or $[Th(^{PO}Cb)_3]^{2-}$ (51.3 ppm), are observed (inset). (d) $^{31}P\{^{1}H\}$ NMR spectrum of the DCE layer following GBE discharging revealing a very broad resonance at 23 ppm which we attribute to an adduct of UO_2^{2+} with ^{PO}Cb.[18] (e) $^{31}P\{^{1}H\}$ NMR spectrum of the DCE layer following UO_2^{2+} release by mixing with fresh NaOAc buffered solution (0.1 M) after 15 h and revealing the free carborane ^{PO}Cb (major), as well as an unknown by-product at 20 ppm, marked by *****.

Each charged solution was then removed from its respective H-cell and mixed with either: 1) a non-buffered (pH = 2.6) aqueous mixed-metal solution with ca. 1.25 equiv of each metal relative to $\mathbf{^{PO}Cb^{2-}}$; 2) a NaOAc-buffered aqueous mixed-metal solution with ca. 1.25 equiv of each metal relative to $^{PO}Cb^{2-}$, or; 3) a NaOAc-buffered (pH = 5.2) aqueous mixed-metal solution with ca. 0.60 equiv of each metal relative to $^{PO}Cb^{2-}$. Significant yellowing of the organic phases was observed after 1.5 h of rapid biphasic mixing (Figure 2.3).

The aqueous mixed-metal phases were analyzed by ICP-OES prior to mixing with the organic phases (pre-X), following biphasic mixing (post-X), as well as following back-X (*vide infra*). Analysis of the non-buffered solution (Figure 2.11) post-X revealed an average decrease in UO_2^{2+} concentration of 20.7%, with minimal observed changes to the concentrations of Th^{4+}, Nd^{3+}, Sm^{3+}, and Cs^+ relative to pre-X. The minor decreases in the concentrations of these latter metals were within error to the observed changes in the controls

which were performed in parallel using identical aqueous and organic solutions (without ^{PO}Cb or $^{PO}Cb^{2-}$), as observed by the hashed bars in Figure 2.11-13. In contrast to this non-buffered solution, analysis of the buffered solution containing ca. 1.25 equiv of each metal (Figure 2.12) post-X revealed an improved extraction of UO_2^{2+} with an average decrease in concentration of 59.7% relative to pre-X. While extraction of Th^{4+}, Nd^{3+}, Sm^{3+}, and Cs^{+} also increased here relative to the non-buffered solution, the observed changes were again within error and consistent with the control experiments, thus suggesting that the observed extraction was not driven by coordination to $^{PO}Cb^{2-}$. We next probed the effect of modifying the $^{PO}Cb^{2-}$: metal ratios. We note that the observed ratios of $^{PO}Cb^{2-}$:UO_2^{2+} are either 1:1[18] (as with Cs^{+}) or 2:1, whereas all other complexes reported here (Th^{4+}, Sm^{3+}, Nd^{3+}) are 3:1. Reducing the mixed-metal aqueous buffered solution concentration to ca. 0.6 equiv of each metal to $^{PO}Cb^{2-}$ revealed an increased post-X extraction of UO_2^{2+} – 71.6% relative to pre-X (Figure 2.13) – compared to the 1.25 equiv extraction (Figure 2.12). While no significant changes in Nd^{3+}, Sm^{3+}, and Cs^{+} concentrations were observed relative to the controls, we did observe a slight decrease in Th^{4+} concentration (9.2% vs. pre-X) which was greater than the control (1.6%) and beyond the detection error limit. These data suggest that while $^{PO}Cb^{2-}$ may drive the extraction of some Th^{4+} under these higher ratios, the selectivity for UO_2^{2+} dominates as evidenced by the calculated separation factor (*SF*), derived from the distribution ratios of metals: $SF_{U/Th} = 25$.[44]

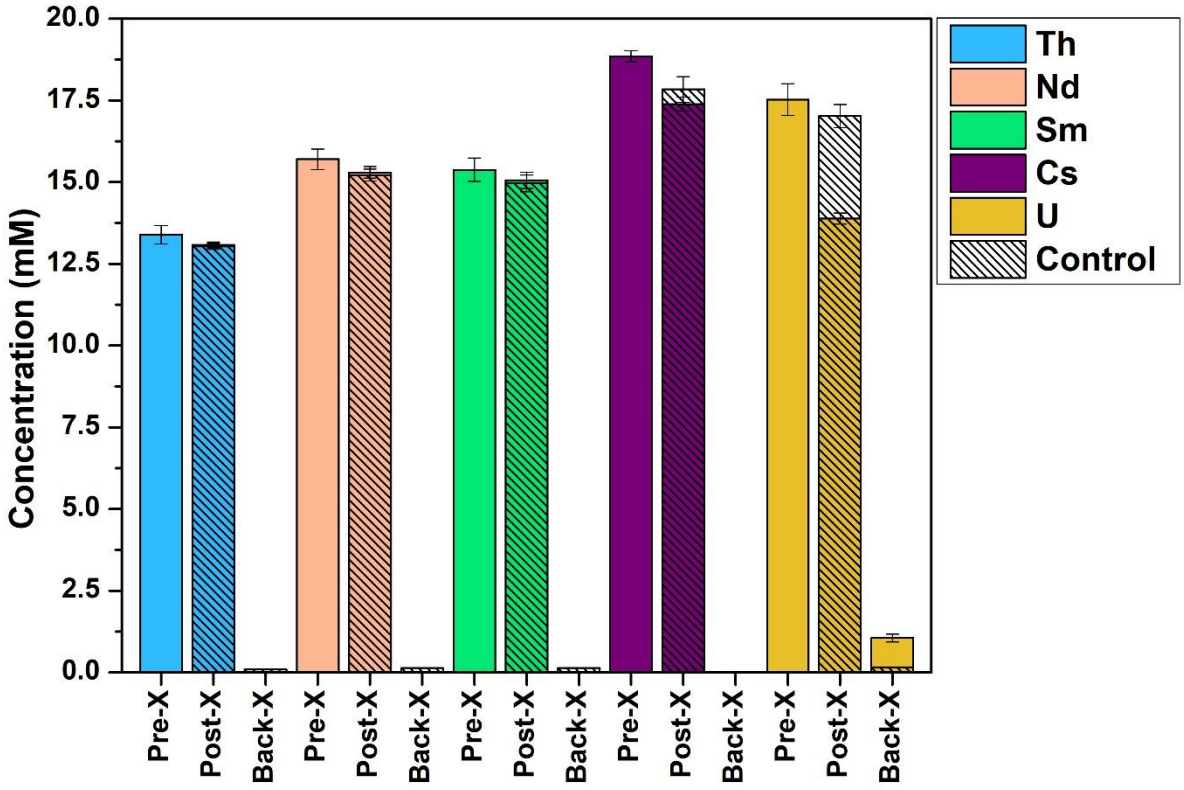

Figure 2.11: ICP-OES results of a non-buffered (pH = 2.6) aqueous mixed-metal solution with ca. 1.25 equiv of each metal

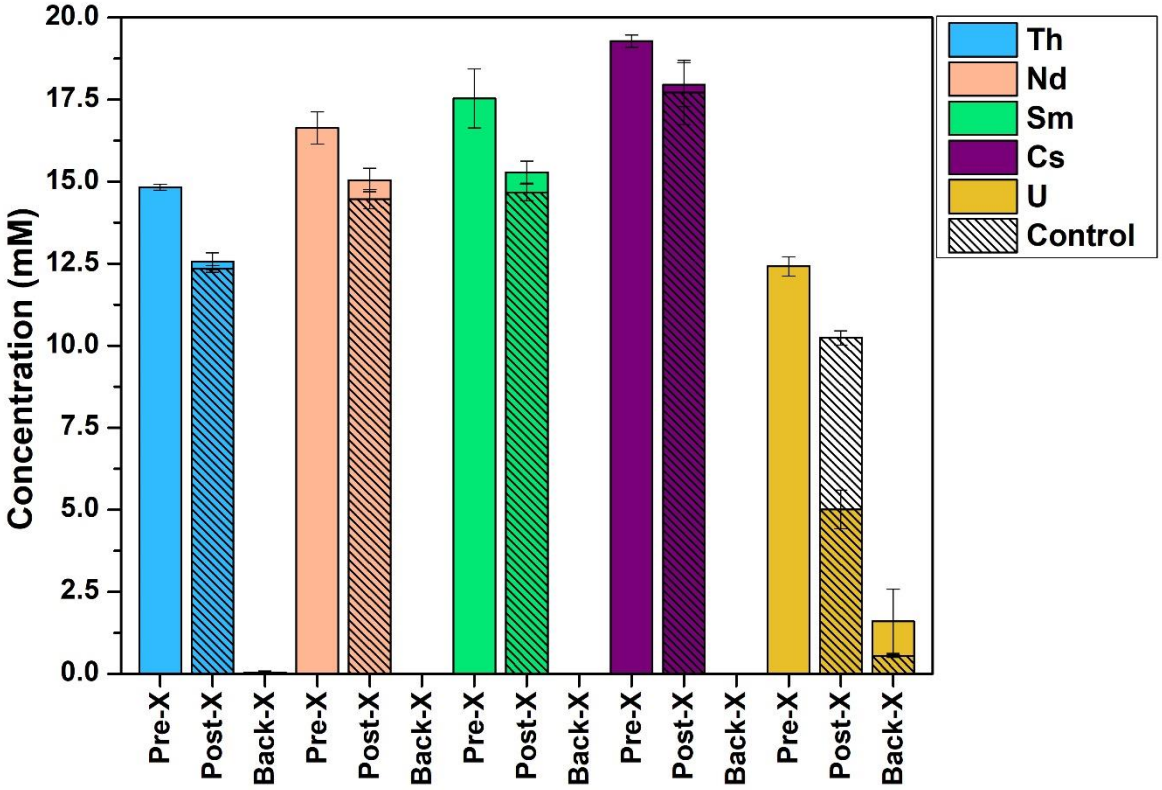

Figure 2.12: ICP-OES results of a NaOAc-buffered (pH = 5.2) aqueous mixed-metal solution with ca. 1.25 equiv of each metal

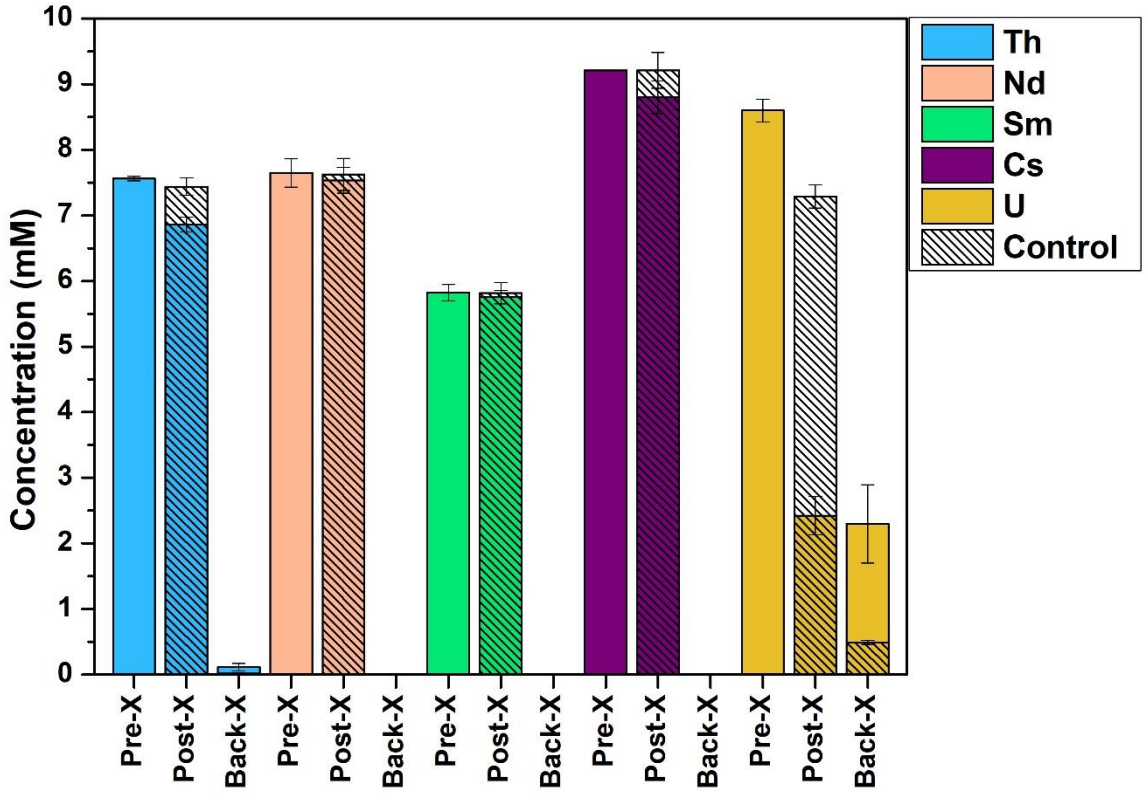

Figure 2.13: ICP-OES results of a NaOAc-buffered (pH = 5.2) aqueous mixed-metal solution with ca. 0.6 equiv of each metal

In each experiment, the organic phases were analyzed by $^{31}P\{^{1}H\}$ NMR spectroscopy prior to GBE, following GBE, following extraction (post-X stage), following GBE discharge (*vide infra*), and following back-X (Figure 2.8-10). Post-X spectrum is shown in Figure 2.8-10c and revealed the clean formation of (integrated ratios relative to initially formed ^{PO}**Cb**$^{2-}$ are in parentheses): a main product at 52.0 ppm (54%), residual ^{PO}**Cb** (18%), and minor new byproduct peaks (28%). The main new resonance at 52.0 ppm in DCE matches the chemical shift of the *bis*-carborane complexe, **[CoCp*$_2$]$_2$[UO$_2$(^{PO}Cb)$_2$]**, in MeCN-d_3 and referenced to $[PPN]^+$ (this salt is insoluble in DCE). Given that the ICP-OES-determined quantity of captured UO_2^{2+} is 0.50 equiv and 0.49 equiv relative to the electrochemically generated

^{PO}Cb^{2-} (1.0 equiv) for the buffered 1.25 equiv (Figure 2.12) and 0.60 equiv (Figure 2.13) reactions, respectively, we propose that the resonance at 52.0 ppm most likely represents the *bis*-ligated anion, **[UO$_2$(^{PO}Cb)$_2$]$^{2-}$**. Together, these results indicate that electrochemically generated **^{PO}Cb^{2-}** *selectively* captures UO_2^{2+} from a mixed alkali, lanthanide, and actinide aqueous phase.

The release of extracted UO_2^{2+} was next probed electrochemically (Figure 2.3). The DCE phase containing the extracted UO_2^{2+} was separated from the aqueous phase and returned to the H-cell where it was galvanostatically discharged to achieve a theoretical final SOC of ca. 0% (Figure 2.14). The DCE layer was next removed from the H-cell and a fresh, buffered (0.1 M NaOAc) or non-buffered aqueous solution was mixed with it rapidly for 15 h. Analysis of the aqueous layers by ICP-OES revealed the back-X of 22-38% of UO_2^{2+} relative to post-X values, with similar values observed regardless of the use of buffered or non-buffered aqueous solutions (Figure 2.11-13). The highest UO_2^{2+} back-X observed were in the 0.6 equiv separations (ca. 38%), wherein concurrent back-X of Th^{4+} was also observed, albeit in smaller quantities (ca. 16%) relative to post-X (Figure 2.13). With the exception of this case, the back-X of all metals except UO_2^{2+} was negligible compared to the controls. Further analysis of the DCE layer by $^{31}P\{^1H\}$ NMR spectroscopy revealed the clean conversion back to the starting *closo*-carborane, ^{PO}Cb (**Figure 2.8**-10e), as well as a minor unknown byproduct at 20.2 ppm (ca. 10% of total carborane peaks). These results demonstrate the clean, electrochemical back-X of selectively captured UO_2^{2+} to an aqueous phase.

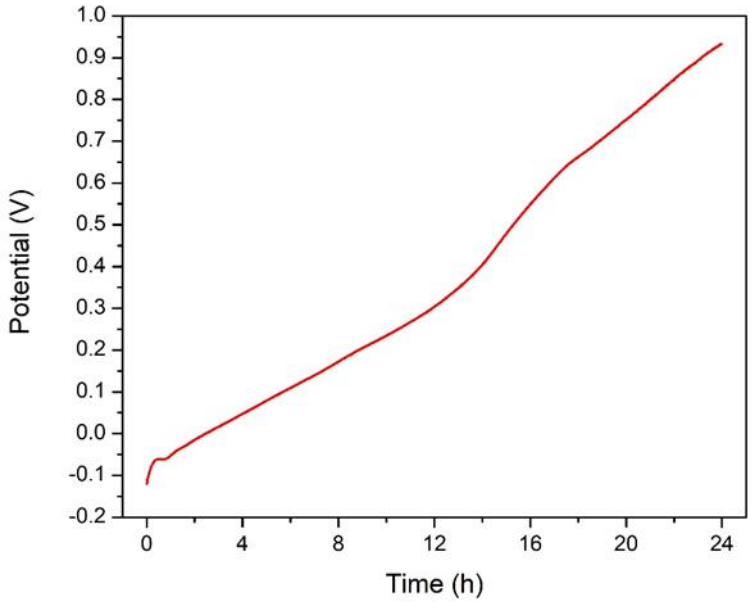

Figure 2.14: Discharging curve for the electrochemical release of UO_2^{2+}. A discharging current of 107.1 μA was applied for a total of ca. 9.25 C of charge transferred, resulting in a 0% SOC after 24 h assuming 100% columbic efficiency.

2.3. Summary

In summary, this chapter demonstrated the selective biphasic electrochemical capture and release of UO_2^{2+} from mixed-metal aqueous media using the redox-switchable ^{PO}**Cb**/^{PO}**Cb**$^{2-}$ system. If Th^{4+} holds as a proper analog for Pu^{4+}, this system has the potential to make significant impact on nuclear fuel recycling process. Further investigation into the reason for the selectivity is ongoing.

2.4. Experimental

2.4.1. Materials and Physical Measurements

General Considerations

All manipulations were performed under an atmosphere of dry, oxygen-free N_2 or Ar by means of standard Schlenk or glovebox techniques (MBraun, equipped with a -38 °C freezer, or VAC gloveboxes). Hexanes, pentane, dichloromethane (DCM), and benzene were dried on an MBraun solvent purification system. Acetonitrile ($–H_3$ and $–D_3$) was dried over CaH_2 for several days prior to distillation. THF was dried over sodium benzophenone and distilled. 1,2-Dichloroethane (DCE) was initially distilled followed by drying over CaH_2 for several days prior to a second distillation and subsequent storage on activated 4 Å molecular sieves. $[Bu_4N][Cl]$ was purchased from Fisher Scientific. $[Th(NO_3)_4•H_2O]$ was purchased from Stream Chemicals. *Ortho*-carborane was purchased from Boron Specialties and sublimed before use. Ph_2PCl was purchased from Aldrich and vacuum distilled prior to use. $CsNO_3$ and decamethylcobaltocene ($CoCp^*_2$) were purchased from Aldrich. $CoCp^*_2$ was purified by filtration through Celite using pentane, followed by recrystallization from pentane at -38 °C over several days. $[Bu_4N][PF_6]$ was purchased from Oakwood Chemicals and purified by twice recrystallizing from hot ethanol. The recrystallized product was then washed with cold water, cold ethanol, and pentane prior to drying at 100 °C under vacuum for 24 h. Sodium acetate (NaOAc) buffers (0.1 and 0.5 M) were prepared from a stock solution purchased from Aldrich (pH 4.9) and adjusted to pH 5.4 using NaOH. The pH value was confirmed using a pH meter. Ketjenblack® EC-600JD (KB) was purchased from a private supplier. $UO_2(NO_3)_2(THF)_2$,[45] $Nd(NO_3)_3(THF)_3$,[46] KC_8,[47] $[Ph_3PNPPh_3][PF_6]$,[48] and compounds ^{PO}**Cb**, **[CoCp*$_2$]$_2$[^{PO}Cb]**, and **[Bu$_4$N]$_2$[^{PO}Cb]** were prepared using literature procedures.[18]

Physical Measurements

NMR spectra were obtained on a Varian Unity Inova 500 MHz or Agilent Technologies 400 MHz spectrometer and referenced to residual solvent resonances of acetonitrile (MeCN-d_3). Unlocked spectra were collected with the ^{2}H lock turned off. Gradient shimming including Z1 to Z5 was done with the strong ^{1}H signal in the samples using a shim map generated with the same or similar sample with equal sample volume. Chemical shifts (δ) are recorded in ppm. All ^{11}B NMR spectra were processed using MestReNova software in order to reduce background signal with a linewidth of approximately 3000 Hz from the Pyrex NMR tubes. The NMR time-domain data were first left-shifted to discard the first ~0.1 ms. To correct the linear phase change, linear prediction (LP) is used to fill the initial discarded data before Fourier transform or an appropriate linear phase correction is applied to the frequency domain data after Fourier transform. T_1 relaxation values for ^{31}P nuclei were determined using the inversion-recovery method. The delay times after the 180-degree inversion pulse varied up to the maximum of 5 times of the expected T_1 values. T_1 values for complexes **^{PO}Cb**, **[CoCp$^*_2$]$_2$[^{PO}Cb]**, **[Bu$_4$N]$_2$[^{PO}Cb]**, **[CoCp$^*_2$]$_2$[UO$_2$Cl$_2$^{PO}Cb]**, **[CoCp$^*_2$]$_2$[UO$_2$(^{PO}Cb)$_2$]**, and [Ph$_3$PNPPh$_3$][PF$_6$] were determined in our previous report.[18]

Elemental analyses (C, N, H) were recorded at the University of California, Berkeley using a Perkin Elmer 2400 Series II combustion analyser.

Galvanostatic Bulk Electrolysis cycling experiments were carried out using a Metrohm Autolab PGSTAT128N potentiostat/galvanostat and carried out inside an Ar glovebox. The full experimental setup for both the mono- and biphasic cycling experiments is described below.

X-ray crystallography data for **[CoCp*$_2$]$_3$[Nd(^{PO}Cb)$_3$]**, were collected at the University of California, Santa Barbara on a Bruker KAPPA APEX II diffractometer equipped with an APEX II CCD detector using a TRIUMPH monochromator with a Mo Kα X-ray source (α = 0.71073 Å). The crystals were mounted on a cryoloop under Paratone-N oil, and all data were collected at 100(2) K using an Oxford nitrogen gas cryostream system. A hemisphere of data was collected using ω scans with 0.5° frame widths. Data collection and cell parameter determination were conducted using the SMART program. Integration of the data frames and final cell parameter refinement were performed using SAINT software. Absorption correction of the data was carried out using SADABS. Structure determination was done using direct or Patterson methods and difference Fourier techniques. All hydrogen atom positions were idealized and rode on the atom of attachment. Structure solution, refinement, graphics, and creation of publication materials were performed using SHELXTL or OLEX2.

Inductively Coupled Plasma-Optical Emission Spectroscopy (ICP-OES) was performed on an Agilent 5800 and used to determine the concentrations of Th, Nd, Sm, Cs, and U in aqueous solutions. Nitric acid (Thermo Scientific, ICP-OES grade for trace metal analysis, ACS testing specifications, LOT 211316) and deionized water (Milli-Q, 18.2 MΩ.cm) were used for sample preparation and dilution. A seven-point calibration curve was made by serial dilution (100- 0.01 ppm) of a custom multi-element certified reference material from High Purity Standards in 2% nitric acid. The emissions lines used were Th (269.242 nm, 274.716 nm, 283.730 nm), Nd (401.224 nm, 406.108 nm, 410.945 nm, 430.357 nm), Sm (356.827 nm, 359.259 nm, 360.949 nm, 446.734 nm), Cs (697.327 nm) and U (263.553 nm, 367.007 nm, 385.957 nm). The calibrations curves for Th, Nd, Sm and U all had $R^2 > 0.9999$. A six-point

calibration curve was used for Cs with a R^2> 0.998, due to an interference in the 0.01 ppm standard.

2.4.2. Synthesis of Compounds

Synthesis of ^{PO}Cb: Step 1) A solution of *n*-BuLi in hexanes (2.5 M, 2.1 eq, 6 mL) was dropwise added to a solution of *o*-carborane (1 eq., 7.16 mmol) in ~100 mL of dry diethyl ether at -78 ^{o}C resulting in a cloudy white solution. The solution was warmed to room temp and stirred for an additional 30 minutes. The solution was cooled back down to -78 ^{o}C and Ph_2PCl (2 eq., 3.85 mL) was dropwise added to the solution. After stirring for 30 minutes, the solution was brought to room temperature and stirred for an additional 30 minutes. The solution was then warmed to a reflux for 30 minutes. The Solution was subsequently cooled to 0 ^{o}C and water (10 mL) slowly added. The product was filtered over a glass frit and washed with an additional 10 mL of water and 7 mL of diethyl ether. The product was dried under vacuum at 100 ^{o}C for 2 hours before being recrystallized from toluene/hexanes to obtain a 58% yield of [(1,2-$(Ph_2P)_2$-1,2-$C_2B_{10}H_{10}$)] (2.13 g). **^{1}H NMR** (400 MHz, $CDCl_3$): δ 7.06–7.47 (m, 20H); 0.98–2.66 (broad, 10H). ^{11}B NMR (400 MHz, $CDCl_3$): δ −0.40, −9.42. **^{11}B{^{1}H} NMR** (400 MHz, $CDCl_3$): δ −0.40, −7.21, −9.42. ^{31}P{^{1}H} NMR (400 MHz, $CDCl_3$): δ 7.88. Step 2) A solution of H_2O_2 (30% in water, 0.75 mL) was added dropwise to a solution of [(1,2-$(Ph_2P)_2$-1,2-$C_2B_{10}H_{10}$)] (from step 1) (0.912 g, 0.8 mmol) in THF (20 ml). The reaction was stirred for 3 h at room temperature. the reaction was discontinued by addition of chloroform. The mixture was washed with water and brine, the phases were separated, and the organic layer was dried with Na_2SO_4. The solvent was removed, and the solid was slowly recrystallized from acetonitrile to yield a colourless crystalline solid. The solid was dried under vacuum at 80 °C for several hours (0.464 mmol, 58% yield). **^{1}H NMR** (400 MHz,

MeCN-d_3): δ 7.99 (m, 8H), 7.63 (m, 4H), 7.54 (m, 8H), 2.5 (broad s, 10H). **^{11}B and ^{11}B{^{1}H}** NMR (400 MHz, MeCN-d_3): δ 0.66, −8.75. **^{31}P{^{1}H} NMR** (400 MHz, MeCN-d_3): δ 22.8.

Synthesis of [CoCp$^*_2$]$_2$[^{PO}Cb]: A 20-ml vial equipped with a magnetic stir bar was charged with **^{PO}Cb** (30.45 mg, 0.056 mmol) and 6 ml of benzene. In a separate vial, recrystallized CoCp$^*_2$ (37 mg, 0.112 mmol, 2.0 equiv.) was dissolved in 4 ml of benzene and added dropwise to the stirring solution of **^{PO}Cb**. Upon addition, a yellow solid immediately precipitated from the reaction mixture, and the mixture was stirred for an additional 4 h at room temperature. Stirring was discontinued and the solid was allowed to settle to the bottom of the vial. The supernatant was filtered over a celite plug. The solids were washed with benzene (3 × 6 ml) and each washing was filtered over the same celite plug. The remaining solids were then dissolved in a minimal amount of MeCN (2 ml) and filtered on the same celite plug into a new vial. The MeCN filtrate was collected, and the volatiles were removed *in vacuo*, yielding a shiny golden-yellow solid (63.9 mg, 0.053 mmols, 95% yield). **^{1}H NMR** (400 MHz, MeCN-d_3): δ 8.05 (broad m, 8H), 7.24 (broad s, 12H), 1.62 (s, 60H). **^{11}B and ^{11}B{^{1}H}** NMR (400 MHZ, MeCN-d_3): δ 20.24, −0.62, −18.46, −22.06. **^{31}P{^{1}H} NMR** (400 MHz, MeCN-d_3): δ 29.8.

Synthesis of [CoCp$^*_2$]$_3$[Nd(^{PO}Cb)$_3$]: A 20 mL vial equipped with a magnetic stir bar was charged with **[CoCp$^*_2$]$_2$[^{PO}Cb]** (36.0 mg, 0.03 mmol) and 2 mL of MeCN. In a separate vial, [Nd$(NO_3)_3$(THF)$_3$] (5.4 mg, 0.01 mmol) was dissolved in 2 mL of MeCN and then added dropwise to the stirring solution of **[CoCp$^*_2$]$_2$[^{PO}Cb]**, where the solution went from golden to bright yellow. The solution remained homogenous, and the reaction was stirred at room temperature for 2 h. The volatiles were removed *in vacuo,* yielding a yellow powder. The

powder was washed with THF (8 mL), and the mixture was transferred onto a bed of Celite on a glass frit. The yellow solid was washed with additional THF (3 x 2 mL). The filter was then dissolved in MeCN into a new vial. The MeCN filtrate was collected, and the volatiles removed *in vacuo*, yielding a yellow powder. Residual $[CoCp^*_2][NO_3]$ was removed from this crude yellow solid by repeated selective recrystallizations (2-3 times) by vapor diffusion of Et_2O into a concentrated pyridine solution of the crude solid at -38 °C. The supernatant was then transferred, and the volatiles removed yielding a yellow solid (18.2 mg, 0.0066 mmol, 66 % yield). Single crystals suitable for XRD studies were grown by vapor diffusion of Et_2O into a saturated MeCN solution of **$[CoCp^*_2]_3[Nd(^{PO}Cb)_3]$** at room temperature. **^{1}H NMR** (400 MHz, MeCN-d_3): δ 9.82 (broad m, 14H); 7.64 (m, 15H); 7.34 (m, 8H); 5.42 (s, 8H); 4.13 (s, 15H); 1.68 (s, 90H). Note: Carborane B–H resonances are too broad to be observed. **^{11}B{^{1}H} NMR** (128 MHz, MeCN-d_3): δ 0.17; -17.57. **^{31}P{^{1}H} NMR** (162 MHz, MeCN-d_3): δ 140.6. *Anal. Calcd*. for $C_{130}H_{168}N_6B_{30}O_6P_6Co_2Nd$: C, 58.20; H, 6.31; N, 3.13. *Found*: C, 58.39; H, 6.96; N, 3.13.

Synthesis of $[CoCp^*_2]_2[Th(^{PO}Cb)_3]$: A 20 mL vial equipped with a magnetic stir bar was charged with **$[CoCp^*_2]_2[^{PO}Cb]$** (24.0 mg, 0.02 mmol) and 2 mL of MeCN. In a separate vial, $[Th(NO_3)_4•H_2O]$ (3.4 mg, 0.0066 mmol) was dissolved in 1 mL of MeCN and then added dropwise to the stirring solution of **$[CoCp^*_2]_2[^{PO}Cb]$**, where the solution went from golden to bright yellow. After stirring for 5 minutes, a yellow solid began to precipitate from the reaction mixture. The mixture was stirred at room temperature for an additional 2 h. Stirring was discontinued, and the mixture was filtered on Celite and yielding a yellow solid and a yellow filtrate. The solvent was removed from the yellow filtrate yielding a yellow solid. Residual $[CoCp^*_2][NO_3]$ was removed from this crude yellow solid by repeated selective

recrystallizations (2-3 times) by vapor diffusion of Et_2O into a concentrated pyridine solution of the crude solid at -38 °C. The supernatant was then transferred, and the volatiles removed yielding a yellow solid (7.1 mg, 0.0029 mmol, 44 % yield). Single crystals suitable for XRD studies were grown by vapor diffusion of Et_2O into a saturated MeCN solution of **[CoCp$^*_2$]$_2$[Th(^{PO}Cb)$_3$]** at room temperature. **^{1}H NMR** (400 MHz, MeCN-d_3): δ 7.95 (m, 12H); 7.84 (m, 12H); 7.09 (m, 18H); 6.87 (t, 6H); 6.15 (m, 12H); 1.69 (s, 60H). Note: Carborane B–**H** resonances are too broad to be observed. **^{11}B{^{1}H} NMR** (128 MHz, MeCN-d_3): δ 0.85; -17.57. **^{31}P{^{1}H} NMR** (162 MHz, MeCN-d_3): δ 51.32. *Anal. Calcd*. for $C_{115}H_{141}B_{30}Co_2O_6P_6Th$: C, 55.7; H, 5.73. *Found*: C, 54.09; H, 5.72.

2.4.3. Biphasic Electrochemical Capture and Release

Conditions: Two-electrode galvanostatic bulk electrolysis (GBE) was performed in an argon glovebox utilizing a two compartment H-cell with a glass frit separator, a stir bar in each compartment, and reticulated vitreous carbon (RVC) foam electrodes for both the working and counter electrodes (Figure 2.6) The RVC foam electrodes consisted of a ~5 cm steel rod inserted into 100 PPI Duocel® RVC foam core (length ~3 cm; diameter ~3 mm), with a tap bore (length ~5 mm; diameter ~2 mm), which was filled with molten gallium to fuse the steel connector to the RVC foam. Each electrode has an end-to-tip resistance of < 10 Ω. The RVC electrodes were rinsed with methanol and dried under reduced pressure overnight prior to use. The Ketjenblack used was dried for 48 h in a 175 ^{o}C oven and ground in a glass mortar and pestle under inert atmosphere prior to use.[18]

Reduction (Charging): The counter compartment consisted of 300 mg of Ketjenblack suspended in 8 mL of a 0.1 M solution of $[Bu_4N][PF_6]$ in DCE. The working compartment consisted of **^{PO}Cb** (34.3 mg, 0.063 mmol, 1.0 equiv) and $[Ph_3PNPPh_3][PF_6]$ (21.7 mg, 0.032

mmol, 0.5 equiv) dissolved in 6 mL of a 0.1 M solution of $[Bu_4N][PF_6]$ in DCE. An initial $^{31}P\{^1H\}$ NMR spectrum was obtained of the DCE layer. A charging current of -107.1 μA with a -9.25 C charge cutoff was utilized, resulting in a ca. 76% SOC after 24 h assuming 100% columbic efficiency (Figure 2.7). Upon completion, the working compartment solution was analyzed by $^{31}P\{^1H\}$ NMR spectroscopy to reveal the formation of **$[^{PO}Cb]^{2-}$** with some remaining **^{PO}Cb** (b, Figure 2.8-10). Based on $[Ph_3PNPPh_3][PF_6]$, the amount of **$[^{PO}Cb]^{2-}$** was determined to be 0.0479 mmol (76% yield). The working compartment solution was then removed from the H-cell and placed in a 20 mL vial for subsequent selective UO_2^{2+} capture chemistry.

Selective UO_2^{2+} Capture: A 60 mL plastic bottle was loaded with either 0.39 or 0.19 mmols of $Th(NO_3)_4•H_2O$, $Nd(NO_3)_3THF_3$, $Sm(NO_3)_3THF_3$, $CsNO_3$ and crystalline $UO_2(NO_3)_2(THF)_2$ and dissolved in 25 mL of Milli-Q water or a 0.5 M NaOAc buffered solution resulting in a bright yellow-green stock solution (Milli-Q pH=2.6, and 0.5 M NaOAc pH=5.4). A 5 mL aliquot of the stock solution (1.25 or 0.6 equiv) was added dropwise without stirring to the DCE solution containing the electrochemically reduced **$^{PO}Cb^{2-}$**. After addition, the mixture was allowed to stir for 1.5 h, resulting in a bright yellow organic phase and a pale yellow-green aqueous phase. Stirring was discontinued and the organic and aqueous phases were separated using a small separatory funnel. A 0.5 mL aliquot was taken from the yellow DCE layer and transferred to an NMR tube. An unlocked $^{31}P\{^1H\}$ NMR spectrum was collected indicating the formation of **$[UO_2X_2{}^{PO}Cb]^{2-}$** (X = NO_3^- or OAc^- due to the mixed anion composition of the aqueous phase), as well as some **^{PO}Cb** and **$[Bu_4N][^{PO}CbH]$**, but no resonances attributable to the captured metal anions, **$[Cs(^{PO}Cb)]^-$**, **$[Nd(^{PO}Cb)_3]^{3-}$**,

[Sm(^{PO}Cb)$_3$]$^{3-}$, or **[Th(^{PO}Cb)$_3$]$^{2-}$** (c, Figure 2.8-10). The NMR solution was returned to the 20 mL vial.

Oxidation (Discharging): The DCE layer was returned to the H-cell and GBE was used to discharge (oxidize) the carborane, initiating UO_2^{2+} release. A discharging current of 107.1 μA with a 9.25 C charge cutoff was utilized resulting in a final SOC of ca. 0 % (Figure 2.14, assuming 100% columbic efficiency and no loss of material during the biphasic capture). Upon completion, a 0.5 mL aliquot was taken from the pale yellow DCE layer and transferred to an NMR tube. An unlocked $^{31}P\{^1H\}$ NMR spectrum was collected indicating a very broad signal between 35–40 ppm which we attribute to an adduct of UO_2^{2+} with **^{PO}Cb** (d, Figure 2.8-10).[18] The NMR sample and working compartment solutions were combined and placed in a 20 mL vial for subsequent release chemistry.

UO_2^{2+} recovery: The 20 mL vial containing the electrochemically discharged DCE solution was equipped with a stir bar and a 5 mL solution of 0.1 M NaOAc buffer or Milli-Q water was added dropwise to it. The mixture was allowed to stir for 15 h, resulting in a bright-yellow aqueous phase and a colorless organic layer. A 0.5 mL aliquot was taken from the colorless DCE layer and transferred to an NMR tube. An unlocked $^{31}P\{^1H\}$ NMR spectrum was collected indicating the clean formation of ^{PO}Cb, $[Ph_3PNPPh_3][PF_6]$, and a small unknown by-product at 20.1 ppm (denoted as *) (e, Figure 2.8-10).

Control: 5 mL of the stock solution was stirred with 6 mL of a 0.1 M solution of $[Bu_4N][PF_6]$ in DCE for 1.5 hours. The aqueous solution was isolated from the DCE layer and saved for analysis by ICP-OES. The DCE layer was then stirred with either 0.1 M NaOAc buffer or Milli-Q water for 15 h. The aqueous solution was isolated from the DCE layer and saved for analysis by ICP-OES.

2.5. Reference

(1) Kumari, I.; Kumar, B. V. R.; Khanna, A. A review on UREX processes for nuclear spent fuel reprocessing. *Nucl. Eng. Des.* **2020**, *358*, 110410. DOI: https://doi.org/10.1016/j.nucengdes.2019.110410.

(2) *Uranium 2020: Resources, Production and Demand*; NUCLEAR ENERGY AGENCY, 2020.

(3) Poinssot, C.; Bourg, S.; Ouvrier, N.; Combernoux, N.; Rostaing, C.; Vargas-Gonzalez, M.; Bruno, J. Assessment of the environmental footprint of nuclear energy systems. Comparison between closed and open fuel cycles. *Energy* **2014**, *69*, 199-211. DOI: https://doi.org/10.1016/j.energy.2014.02.069.

(4) Lanham, W. B.; Runion, T. C. *PUREX PROCESS FOR PLUTONIUM AND URANIUM RECOVERY*; United States, 1949. https://www.osti.gov/biblio/4165457 https://www.osti.gov/servlets/purl/4165457DOI: 10.2172/4165457
Other Information: Decl. with deletions Apr. 18, 1960. Orig. Receipt Date: 31-DEC-60.

(5) OECD. *The Economics of the Back End of the Nuclear Fuel Cycle*; 2014. DOI: doi:https://doi.org/10.1787/9789264208520-en.

(6) Glatz, J.-P. 6.11 - Spent Fuel Dissolution and Reprocessing Processes. In *Comprehensive Nuclear Materials (Second Edition)*, Konings, R. J. M., Stoller, R. E. Eds.; Elsevier, 2020; pp 305-326.

(7) *International Framework for Nuclear Energy Cooperation*. World Nuclear Association, https://world-nuclear.org/information-library/current-and-future-generation/international-framework-for-nuclear-energy-coopera.aspx (accessed.

(8) Vandegrift, G. F.; Regalbuto, M. C.; Aase, S. B.; Bakel, A. J.; Battisti, T. J.; Bowers, D. L.; Byrnes, J. P.; Clark, M. A.; Cummings, D. G.; Emery, J. W.; et al. Designing and Demonstration of the UREX+ Process Using Spent Nuclear Fuel. 2004.

(9) Choi, S.; Nam, H. O.; Ko, W. I. Environmental life cycle risk modeling of nuclear waste recycling systems. *Energy* **2016**, *112*, 836-851. DOI: https://doi.org/10.1016/j.energy.2016.06.127.

(10) Borges Silverio, L.; Lamas, W. d. Q. An analysis of development and research on spent nuclear fuel reprocessing. *Energy Policy* **2011**, *39* (1), 281-289. DOI: https://doi.org/10.1016/j.enpol.2010.09.040.

(11) Lyseid Authen, T.; Adnet, J.-M.; Bourg, S.; Carrott, M.; Ekberg, C.; Galán, H.; Geist, A.; Guilbaud, P.; Miguirditchian, M.; Modolo, G.; et al. An overview of solvent extraction processes developed in Europe for advanced nuclear fuel recycling, Part 2 — homogeneous recycling. *Sep. Sci. Technol.* **2022**, *57* (11), 1724-1744. DOI: 10.1080/01496395.2021.2001531.

(12) Geist, A.; Adnet, J.-M.; Bourg, S.; Ekberg, C.; Galán, H.; Guilbaud, P.; Miguirditchian, M.; Modolo, G.; Rhodes, C.; Taylor, R. An overview of solvent extraction processes developed in Europe for advanced nuclear fuel recycling, part 1 — heterogeneous recycling. *Sep. Sci. Technol.* **2021**, *56* (11), 1866-1881. DOI: 10.1080/01496395.2020.1795680.

(13) *Carboranes (Second Edition)*; Academic Press, 2011. DOI: https://doi.org/10.1016/B978-0-12-374170-7.00019-7.

(14) Heying, T. L.; Ager, J. W., Jr.; Clark, S. L.; Mangold, D. J.; Goldstein, H. L.; Hillman, M.; Polak, R. J.; Szymanski, J. W. A New Series of Organoboranes. I. Carboranes from the

Reaction of Decaborane with Acetylenic Compounds. *Inorg. Chem.* **1963**, *2* (6), 1089-1092. DOI: 10.1021/ic50010a002.

(15) Fisher, S. P.; Tomich, A. W.; Lovera, S. O.; Kleinsasser, J. F.; Guo, J.; Asay, M. J.; Nelson, H. M.; Lavallo, V. Nonclassical Applications of closo-Carborane Anions: From Main Group Chemistry and Catalysis to Energy Storage. *Chem. Rev.* **2019**, *119* (14), 8262-8290. DOI: 10.1021/acs.chemrev.8b00551.

(16) Plesek, J. Potential applications of the boron cluster compounds. *Chem. Rev.* **1992**, *92* (2), 269-278. DOI: 10.1021/cr00010a005.

(17) Núñez, R.; Tarrés, M.; Ferrer-Ugalde, A.; de Biani, F. F.; Teixidor, F. Electrochemistry and Photoluminescence of Icosahedral Carboranes, Boranes, Metallacarboranes, and Their Derivatives. *Chem. Rev.* **2016**, *116* (23), 14307-14378. DOI: 10.1021/acs.chemrev.6b00198.

(18) Keener, M.; Hunt, C.; Carroll, T. G.; Kampel, V.; Dobrovetsky, R.; Hayton, T. W.; Ménard, G. Redox-switchable carboranes for uranium capture and release. *Nature* **2020**, *577* (7792), 652-655. DOI: 10.1038/s41586-019-1926-4.

(19) Zhang, Y.; Duan, W.; Yang, Y.; Jian, T.; Qiao, Y.; Ren, G.; Zhang, N.; Zheng, L.; Yan, W.; Wang, J.; et al. Involvement of 5f Orbitals in the Covalent Bonding between the Uranyl Ion and Trialkyl Phosphine Oxide: Unraveled by Oxygen K-Edge X-ray Absorption Spectroscopy and Density Functional Theory. *Inorg. Chem.* **2022**, *61* (1), 92-104. DOI: 10.1021/acs.inorgchem.1c02236.

(20) Wu, Y.; Zhang, X.; Kim, S.-Y.; Wei, Y. Simultaneous separation and recovery of Cs(I) and Sr(II) using a hybrid macrocyclic compounds loaded adsorbent. Kinetic, equilibrium and dynamic adsorption studies. *J. Nucl. Sci. Technol.* **2016**, *53* (12), 1968-1977. DOI: 10.1080/00223131.2016.1175979.

(21) Carbol, P.; Wegen, D. H.; Wiss, T.; Fors, P.; Jegou, C.; Spahiu, K. 6.13 - Spent Nuclear Fuel as Waste Material. In *Comprehensive Nuclear Materials (Second Edition)*, Konings, R. J. M., Stoller, R. E. Eds.; Elsevier, 2020; pp 347-386.

(22) Denecke, M. A.; Bryan, N.; Kalmykov, S.; Morris, K.; Quinto, F. Sources and Behaviour of Actinide Elements in the Environment. In *Experimental and Theoretical Approaches to Actinide Chemistry*, Gibson, J. K., Jong, W. A. Eds.; Wiley, 2018; pp 378-444.

(23) Clark, A. E.; Yang, P.; Shafer, J. C. Coordination of Actinides and the Chemistry Behind Solvent Extraction. In *Experimental and Theoretical Approaches to Actinide Chemistry*, Gibson, J. K., Jong, W. A. Eds.; Wiley, 2018; pp 237-282.

(24) Arliguie, T.; Belkhiri, L.; Bouaoud, S.-E.; Thuéry, P.; Villiers, C.; Boucekkine, A.; Ephritikhine, M. Lanthanide(III) and Actinide(III) Complexes $[M(BH_4)_2(THF)_5][BPh_4]$ and $[M(BH_4)_2(18\text{-crown-}6)][BPh_4]$ (M = Nd, Ce, U): Synthesis, Crystal Structure, and Density Functional Theory Investigation of the Covalent Contribution to Metal-Borohydride Bonding. *Inorg. Chem.* **2009**, *48* (1), 221-230. DOI: 10.1021/ic801685v.

(25) Rivière, C.; Nierlich, M.; Ephritikhine, M.; Madic, C. Complexation Studies of Iodides of Trivalent Uranium and Lanthanides (Ce and Nd) with 2,2‘-Bipyridine in Anhydrous Pyridine Solutions. *Inorg. Chem.* **2001**, *40* (17), 4428-4435. DOI: 10.1021/ic001411j.

(26) Lahrouch, F.; Sofronov, O.; Creff, G.; Rossberg, A.; Hennig, C.; Den Auwer, C.; Di Giorgio, C. Polyethyleneimine methylphosphonate: towards the design of a new class of macromolecular actinide chelating agents in the case of human exposition. *Dalton Trans.* **2017**, *46* (40), 13869-13877, 10.1039/C7DT02643A. DOI: 10.1039/C7DT02643A.

(27) Bingham, P. A.; Hand, R. J.; Stennett, M. C.; Hyatt, N. C.; Harrison, M. T. The Use of Surrogates in Waste Immobilization Studies: A Case Study of Plutonium. *MRS Proceedings* **2011**, *1107*, 421. DOI: 10.1557/PROC-1107-421 From Cambridge University Press Cambridge Core.

(28) Gorden, A. E. V.; Xu, J.; Raymond, K. N.; Durbin, P. Rational Design of Sequestering Agents for Plutonium and Other Actinides. *Chem. Rev.* **2003**, *103* (11), 4207-4282. DOI: 10.1021/cr990114x.

(29) Hosmane, N. S.; Demissie, T.; Zhang, H.; Maguire, J. A.; Lipscomb, W. N.; Baumann, F.; Kaim, W. Synthesis and Crystal Structure of the First Polymeric Cesium Compound of a Carborane Ligand System. *Organometallics* **1998**, *17* (3), 293-295. DOI: 10.1021/om970938+.

(30) Oki, A. R.; Sokolova, O.; Gilbes, B.; Aduroja, A.; Abdelaziz, G.; Emge, T. J. A novel cesium–carborane cluster: synthesis and structure of $[Cs_5–(C_2B_9H_{12})_4Cl]_n$. *Inorg. Chem. Commun.* **2002**, *5* (9), 694-697. DOI: https://doi.org/10.1016/S1387-7003(02)00538-5.

(31) Neufeld, R.; Michel, R.; Herbst-Irmer, R.; Schöne, R.; Stalke, D. Introducing a Hydrogen-Bond Donor into a Weakly Nucleophilic Brønsted Base: Alkali Metal Hexamethyldisilazides (MHMDS, M=Li, Na, K, Rb and Cs) with Ammonia. *Chem. Eur. J.* **2016**, *22* (35), 12340-12346. DOI: https://doi.org/10.1002/chem.201600833.

(32) Ojeda-Amador, A. I.; Martínez-Martínez, A. J.; Kennedy, A. R.; O'Hara, C. T. Structural Studies of Cesium, Lithium/Cesium, and Sodium/Cesium Bis(trimethylsilyl)amide (HMDS) Complexes. *Inorg. Chem.* **2016**, *55* (11), 5719-5728. DOI: 10.1021/acs.inorgchem.6b00839.

(33) Berthet, J.-C.; Nierlich, M.; Ephritikhine, M. A comparison of analogous 4f- and 5f-element compounds: syntheses and crystal structures of triphenylphosphine oxide complexes of lanthanide(III) and uranium(III) triflates and iodides $[MX_2(OPPh_3)_4][X]$ (X=OTf and M=Ce or U; X=I and M=Nd, Ce, La, U). *Polyhedron* **2003**, *22* (27), 3475-3482. DOI: https://doi.org/10.1016/j.poly.2003.09.008.

(34) Spichal, Z.; Necas, M.; Pinkas, J.; Zdrahal, Z. Binuclear complexes of lanthanides with 1,4-bis(diphenylphosphino)butane dioxide. *Polyhedron* **2006**, *25* (3), 809-814. DOI: https://doi.org/10.1016/j.poly.2005.08.007.

(35) Miyata, K.; Nakagawa, T.; Kawakami, R.; Kita, Y.; Sugimoto, K.; Nakashima, T.; Harada, T.; Kawai, T.; Hasegawa, Y. Remarkable Luminescence Properties of Lanthanide Complexes with Asymmetric Dodecahedron Structures. *Chem. Eur. J.* **2011**, *17* (2), 521-528. DOI: https://doi.org/10.1002/chem.201001993.

(36) Pan, Y.-Z.; Hua, Q.-Y.; Lin, L.-S.; Qiu, Y.-B.; Liu, J.-L.; Zhou, A.-J.; Lin, W.-Q.; Leng, J.-D. A slowly magnetic relaxing Sm^{III} monomer with a D_{5h} equatorial compressed ligand field. *Inorg. Chem. Front.* **2020**, *7* (12), 2335-2342, 10.1039/D0QI00326C. DOI: 10.1039/D0QI00326C.

(37) Korobkov, I.; Arunachalampillai, A.; Gambarotta, S. Cyclometalation and Solvent Deoxygenation during Reduction of a Homoleptic $Th(OAr)_4$ Complex: Serendipitous Formation of a Terminally Bonded Th−OH Function. *Organometallics* **2004**, *23* (26), 6248-6252. DOI: 10.1021/om049369d.

(38) Nelson, A.-G. D.; Bray, T. H.; Stanley, F. A.; Albrecht-Schmitt, T. E. Periodic Trends in Actinide Phosphonates: Divergence and Convergence between Thorium, Uranium,

Neptunium, and Plutonium Systems. *Inorg. Chem.* **2009**, *48* (10), 4530-4535. DOI: 10.1021/ic900484w.

(39) Diwu, J.; Good, J. J.; DiStefano, V. H.; Albrecht-Schmitt, T. E. Self-Assembly of Hexanuclear Clusters of 4f and 5f Elements with Cation Specificity. *Eur. J. Inorg. Chem.* **2011**, *2011* (9), 1374-1377. DOI: https://doi.org/10.1002/ejic.201100066.

(40) Keener, M.; Mattejat, M.; Zheng, S.-L.; Wu, G.; Hayton, T. W.; Ménard, G. Selective electrochemical capture and release of uranyl from aqueous alkali, lanthanide, and actinide mixtures using redox-switchable carboranes. *Chem. Sci.* **2022**, *13* (12), 3369-3374, 10.1039/D1SC07070C. DOI: 10.1039/D1SC07070C.

(41) Quilès, F.; Nguyen-Trung, C.; Carteret, C.; Humbert, B. Hydrolysis of Uranyl(VI) in Acidic and Basic Aqueous Solutions Using a Noncomplexing Organic Base: A Multivariate Spectroscopic and Statistical Study. *Inorg. Chem.* **2011**, *50* (7), 2811-2823. DOI: 10.1021/ic101953q.

(42) Pant, D. D.; Khandelwal, D. P. The absorption and fluorescence spectra of uranyl nitrate solutions at room temperature. *Proc. Natl. Acad. Sci. India A* **1959**, *50* (5), 323-335, journal article. DOI: 10.1007/bf03048924.

(43) Hunt, C.; Mattejat, M.; Anderson, C.; Sepunaru, L.; Ménard, G. Symmetric Phthalocyanine Charge Carrier for Dual Redox Flow Battery/Capacitor Applications. *ACS Appl. Energy Mater.* **2019**, *2*, 5391-5396. DOI: 10.1021/acsaem.9b01317.

(44) Thiele, N. A.; Fiszbein, D. J.; Woods, J. J.; Wilson, J. J. Tuning the Separation of Light Lanthanides Using a Reverse-Size Selective Aqueous Complexant. *Inorg. Chem.* **2020**, *59* (22), 16522-16530. DOI: 10.1021/acs.inorgchem.0c02413.

(45) Reynolds, J. G.; Zalkin, A.; Templeton, D. H. Structure of uranyl nitrate-bis(tetrahydrofuran). *Inorganic Chemistry* **1977**, *16* (12), 3357-3359. DOI: 10.1021/ic50178a078.

(46) Evans, W. J.; Giarikos, D. G.; Workman, P. S.; Ziller, J. W. Utility of Anhydrous Neodymium Nitrate as a Precursor to Extended Organoneodymium Nitrate Networks. *Inorganic Chemistry* **2004**, *43* (18), 5754-5760. DOI: 10.1021/ic049187b.

(47) Lalancette, J. M.; Rollin, G.; Dumas, P. Metals Intercalated in Graphite. I. Reduction and Oxidation. *Canadian Journal of Chemistry* **1972**, *50* (18), 3058-3062. DOI: 10.1139/v72-485 (acccessed 2014/11/20).

(48) Liu, Y.; Ren, W.-M.; Liu, C.; Fu, S.; Wang, M.; He, K.-K.; Li, R.-R.; Zhang, R.; Lu, X.-B. Mechanistic Understanding of Dinuclear Cobalt(III) Complex Mediated Highly Enantioselective Copolymerization of meso-Epoxides with CO2. *Macromolecules* **2014**, *47* (22), 7775-7788. DOI: 10.1021/ma5019186.

Chapter 3 Selective Heterogeneous Capture and Release of Actinides using Carborane-Functionalized Electrodes

3.1. Introduction

The main recycling processes for SNF utilize a biphasic liquid-liquid extractions to separate U from the rest of the waste in SNF.[1, 2] While they work well to isolate U, these approaches can generate excess volumes of radioactive waste. Switching to a heterogeneous system would help reduce the amount of radioactive waste generated from the separation processes.

Heterogeneous capture of UO_2^{2+} has largely been focused on seawater mining, with the two main approaches being functionalized porous sorbents and electrodeposition on functionalized electrodes.[3] Amidoxime and sulfide functionalized sorbent materials have been demonstrated to selectively bind UO_2^{2+} over other ions commonly found in seawater.[4-7] These systems typically are made by adding functional groups to metal organic frameworks or carbon backbones. They can passively capture $UO_2^{2+}$when submerged into aqueous solutions and are typically demonstrated with seawater spiked with various concentrations of UO_2^{2+}. The capture generally is slow, taking days to reach their full saturation of UO_2^{2+}, especially with natural seawater. The relatively slow capture, however, is not a major issue for their application in seawater mining. Theoretically, large towers of these functionalized materials would be deposited into the ocean and retrieved once saturated. Functionalized electrodes for electrodeposition of UO_2^{2+} have also been proposed as a heterogeneous methods for UO_2^{2+} extraction.[8, 9] These systems apply a voltage to a functionalized electrode to reduce U(VI) to U(IV) to deposit it onto the surface of the electrode. Unlike the passive methods, electrodeposition does not have a saturation point and can continue to capture U indefinitely.

We were interested in converting our biphasic system to a heterogeneous method by grafting **^{PO}Cb** onto carbon electrodes. Conversion of homogenous molecularly active

compounds to heterogeneous systems has been widely demonstrated in the catalysis field.[10] Covalent and non-covalent bonding techniques haven been used for this conversion to generate heterogeneous electrocatalysts that are stable, efficient, and retain electrochemical activity.[11] A rapid method of conversion can be achieved using non-covalent interactions such insoluble immobilisation, π-π interactions, and electrostatic interactions with electrodes.

The use of π-π interactions to graft electrocatalysts to electrodes can be accomplished by adding π-π stacking groups to the catalysts.[12-14] π-π stacking refers to the non-covalent bonding between the π orbitals of aromatic rings.[15, 16] These non-covalent forces play a role in the formation of many natural structures such as proteins and DNA, but have also been used to make functionalized surfaces. This method of functionalization affords the benefits of being a non-destructive and a reversible process, with the downsides of having a lack of directional control of the functionalization. These interactions are also relatively weak and materials can lose the functionalized groups from the surface when added to solutions in which the functionalizing groups are highly soluble.[17] Pyrene is often used as a π-π stacking functional group for electrocatalyst and these complexes have been widely shown to retain electrochemical activity when grafted onto electrodes.[12-14]

In the previous chapter, we used a biphasic electrochemical process that selectively captured UO_2^{2+} from simulated SNF (Cs^+, Nd^{3+}, Sm^{3+}, Th^{4+}, UO_2^{2+}) using $^{PO}\mathbf{Cb}^{2-}$ (Figure 3.1a). We wanted to further expand this work and simplify the process by moving to an electrochemical heterogeneous method. We approached this conversion in a similar fashion as molecular catalysts, and made functionalized electrodes using drop casting techniques.[11] These functionalized electrodes demonstrated carborane-based heterogeneous electrochemical behaviour that was enhanced by the inclusion of single-walled carbon

nanotubes (CNTs). The functionalized electrodes were galvanostatically charged and selectively captured and released actinides (Th^{4+}, UO_2^{2+}) from a mixed solutions containing alkali (Cs^+), lanthanide (Nd^{3+}, Sm^{3+}) and actinide (Th^{4+}, UO_2^{2+}) metal ions (Figure 3.1b) as will be described in this chapter.

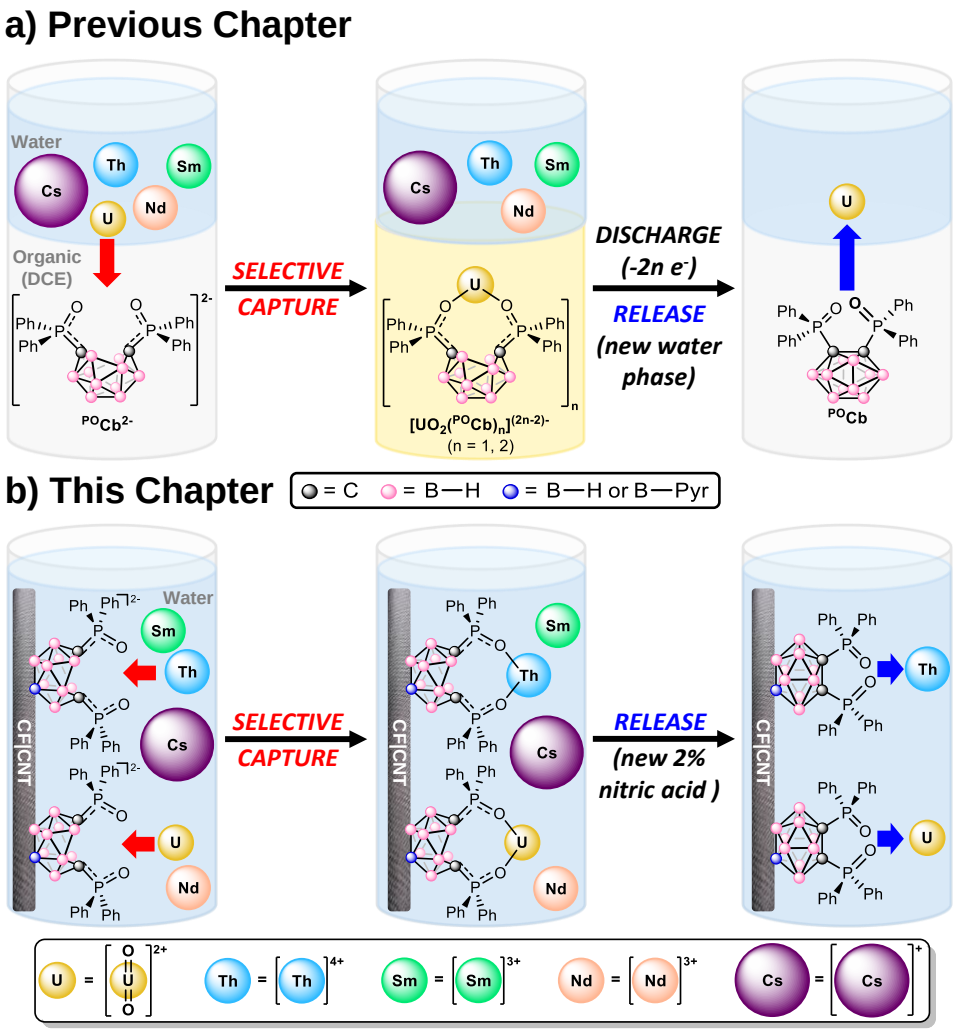

Figure 3.1: Biphasic versus heterogeneous capture schemes. a) selective UO_2^{2+} capture and release using an electrochemical biphasic scheme. b) heterogeneous actinide capture and release using functionalized carbon fiber electrodes (CF|CNT|^{PO}Cb, CF|CNT|^{PO}Cb-Pyr).

3.2. Results and Discussion

3.2.1 Synthesis and Characterization

We were interested in investigating if the addition of a π-π stacking group to the 9-position of the carborane (Figure 2.1) would enable it to adhere to carbon surfaces or pyrene-functionalized surfaces. We decided on the addition of a pyrene group as they have been shown widely in the literature to add π-π interactions to compounds.[11, 17] The synthesis of 9-pyrenyl-*otho*-carborane was achieved by a modified literature synthesis.[18] 9-pyrenyl -*ortho*-carborane was fully characterized by NMR spectroscopy and a solid-state structure was obtained by single-crystal XRD studies (Figure 3.2). In $CDCl_3$, the ^1H NMR spectrum had distinctive aryl peaks from the addition of the pyrene group and two singlets from the carborane C–H peaks around 3.7 ppm. The $^{11}B\{^1H\}$ spectrum showed six distinct boron resonances, which correlated with the symmetry observed in the solid state structure. In the expanded crystal structure, π-π stacking can be observed between the pyrenes attached to the carborane.

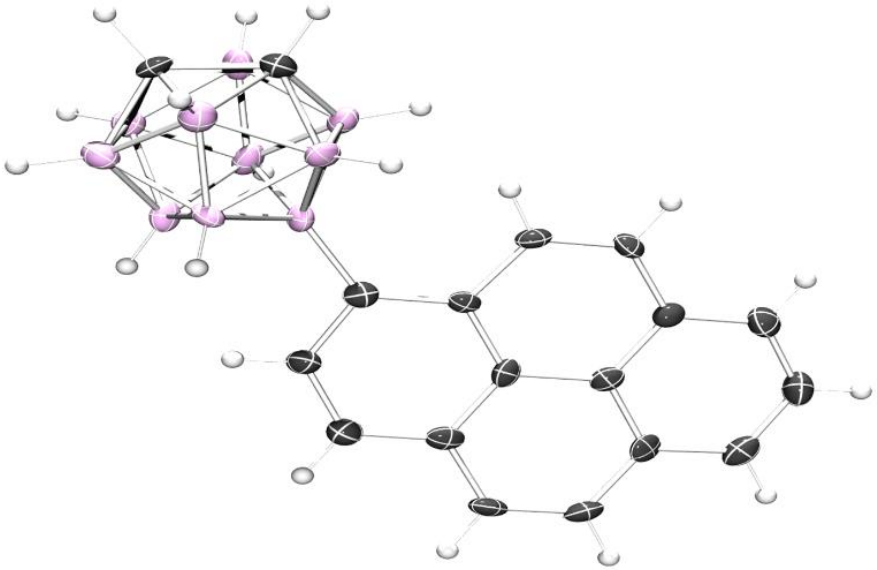

Figure 3.2: Low resolution solid-state molecular structure of 9-pyrenyl-*ortho*-carborane

The addition of the diphenylphosphine groups was achieved using similar conditions to the non-substituted counterpart,[19] but required higher solvent volumes and longer reaction times due to the poor solubility of the 9-pyrenyl-*ortho*-Carborane. 1,2-$(Ph_2P)_2$ -9-pyrenyl-*ortho*-carborane was fully characterized NMR spectroscopy and a solid-state structure was obtained by single-crystal XRD studies (Figure 3.3). The ^{1}H NMR spectrum, in $CDCl_3$, showed the loss of the two singlets form the carborane C–H peaks and the addition of multiplets in the aryl region from the phenyl groups. The ^{11}B and $^{11}B\{^{1}H\}$ spectra had four distinct boron resonances. The $^{31}P\{^{1}H\}$ spectrum displayed two roofed doublets with analogous coupling constants (give value).

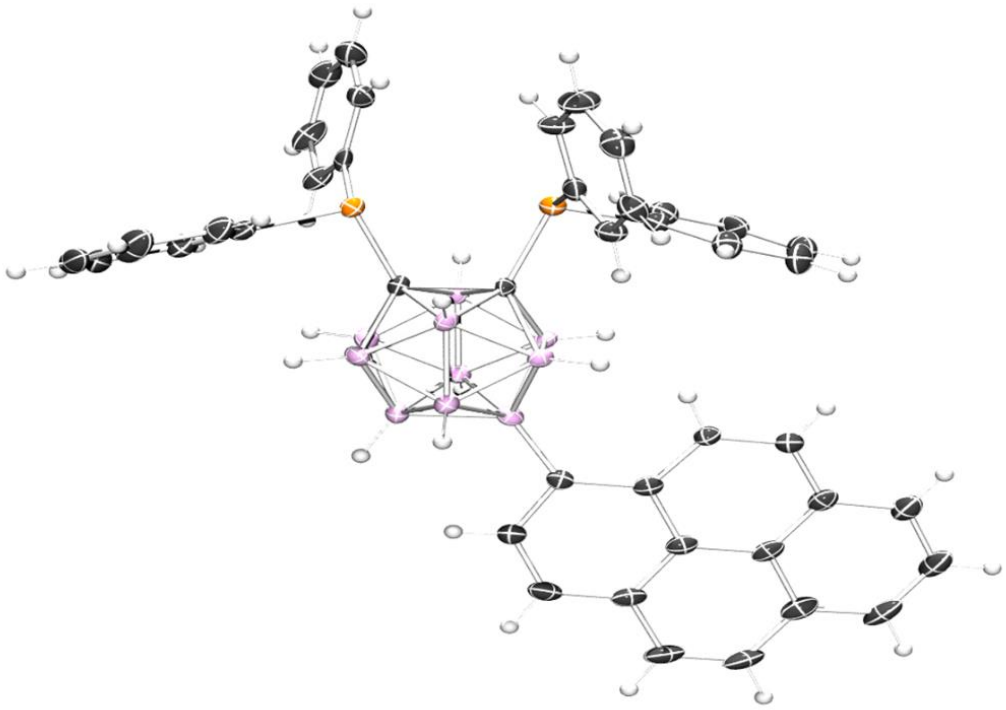

Figure 3.3: Low resolution solid-state molecular structure of 1,2-$(Ph_2P)_2$-9-pyrenyl-*ortho*-carborane

1,2-$(Ph_2PO)_2$-9-pyrenyl-*ortho*-Carborane (**^{PO}Cb-Pyr**) was synthesized using *meta*-chloroperoxybenzoic acid. **^{PO}Cb-Pyr** was characterized by NMR spectroscopy and elemental analysis, but the growth of XRD quality single crystals of **^{PO}Cb-Pyr** was unsuccessful. The ^{1}H NMR spectrum, in $CDCl_3$, remained fairly similar to the 1,2-$(Ph_2P)_2$ -9-pyrenyl-*ortho*-Carborane, but with a slight shift up field for the signals from the pyrene. The ^{11}B and ^{11}B{^{1}H} NMR spectra retained four distinct boron resonances and the ^{31}P{^{1}H} spectrum had two signets at 24.43 and 24.20 ppm.

The **^{PO}Cb-Pyr^{2-}** was obtained by reduction with two equivalences of decamethylcobaltocene ($CoCp_2^*$). **^{PO}Cb-Pyr^{2-}** was characterized by NMR spectroscopy and like **^{PO}Cb-Pyr**, we were unable to obtain XRD quality single crystals. The ^{1}H NMR spectrum,

in MeCN-d_3, revealed an upfield shift in the aromatic pyrene signals. The ^{11}B and $^{11}B\{^1H\}$ spectra had five unique boron resonances shifted downfield. The $^{31}P\{^1H\}$ spectrum shifted up field, with the singlets at 30.13 and 29.62 ppm.

We were interested in finding characterization methods that could potentially be used to show the generation of the *nido* species on the surface of electrodes. Attenuated Total Reflectance Fourier Transform Infrared (ATR-FTIR) spectra were acquired for *closo* and *nido* carborane powders to assess any differences. Carboranes are known to have a distinctive vibrational frequency for the B–H bond stretches around 2600 cm^{-1}, that is dependent on the symmetry and substitution of the carborane.[20]

The ATR-FTIR spectrum for ^{PO}**Cb** revealed multiple B-H stretch peaks centered around 2600 cm^{-1}(Figure 3.4). The ^{PO}**Cb**$^{2-}$ B–H stretches shifted to 2470 cm^{-1} and resolved more towards a singular peak (Figure 3.4). This shift to lower wavenumbers likely occurs due to the increased electron density in the cage lengthening and weakening the B–H bonds.

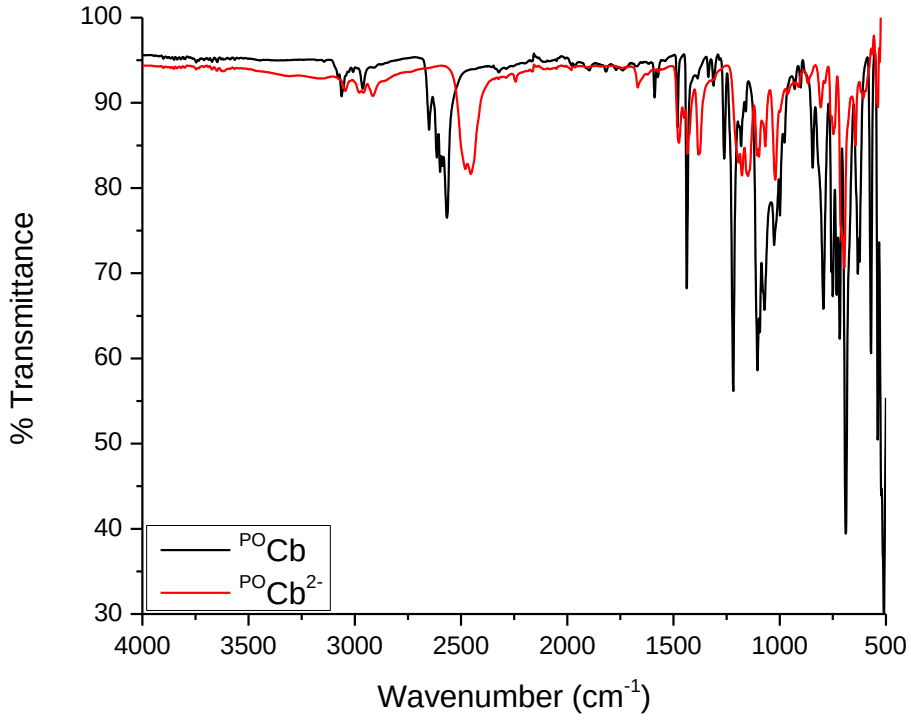

Figure 3.4: ATR-FTIR spectra of powder ^{PO}Cb and ^{PO}Cb^{2-} ([CoCp$_2^*$]$_2$[^{PO}Cb])

The B–H stretches for the *closo/nido* of the **^{PO}Cb-Pyr** had a similar shift as the **^{PO}Cb**. The **^{PO}Cb-Pyr** had multiple B–H stretches centered around 2590 cm^{-1}, while the **^{PO}Cb-Pyr^{2-}** shifted to 2476 cm^{-1} as a singular peak (Figure 3.5). This shift between the *closo/nido* forms could potentially be used as a method for determining if the *nido* species is generated on the surface of electrodes, assuming the electrode does not interfere in that region.

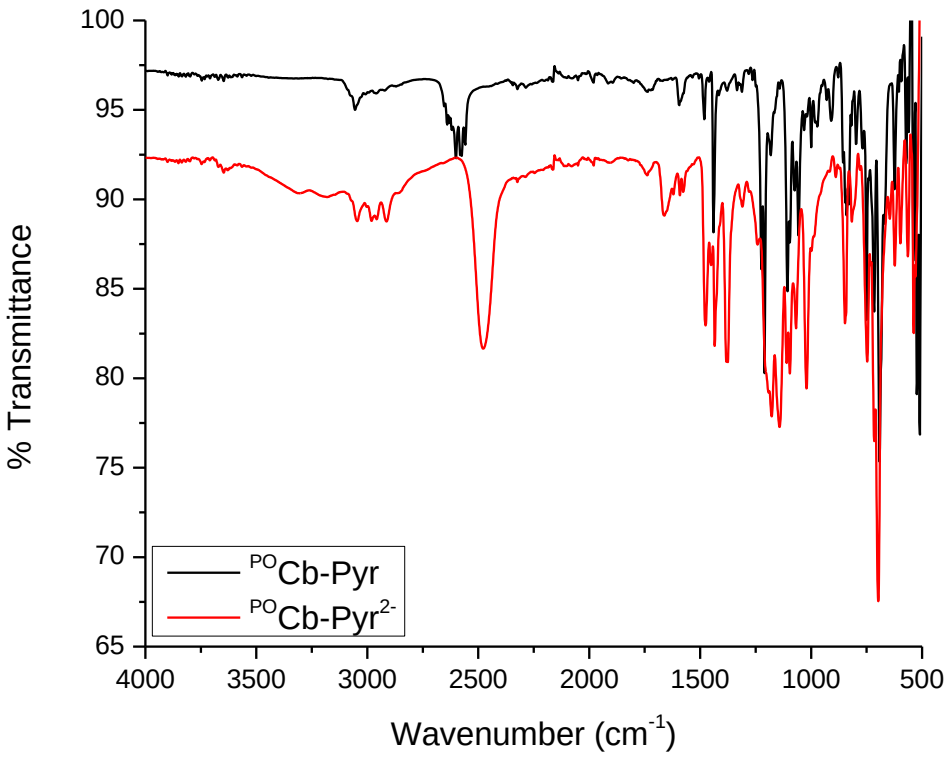

Figure 3.5: ATR-FTIR spectra of powder ^{PO}Cb-Pyr and ^{PO}Cb-Pyr^{2-} ([CoCp$_2^*$]$_2$[^{PO}Cb-Pyr])

Additionally, the B–H stretch of carboranes is Raman active around 2600 cm^{-1}.[20] We acquired the Raman spectrum of **^{PO}Cb**, revealing multiple peaks centered around 2605 cm^{-1} (Figure 3.6). The **^{PO}Cb^{2-}** signal shifted to 2484 cm^{-1} with fewer peaks observed (Figure 3.6), similar to what was observed in the IR spectrum (Figure 3.4). The **^{PO}Cb^{2-}**, however, under these conditions was not very stable, with the sample degrading and leaving a hole where the laser hit. The weak signal and poor stability under the laser suggest this may not be the best approach to characterizing the *nido* generation on the surface of electrodes.

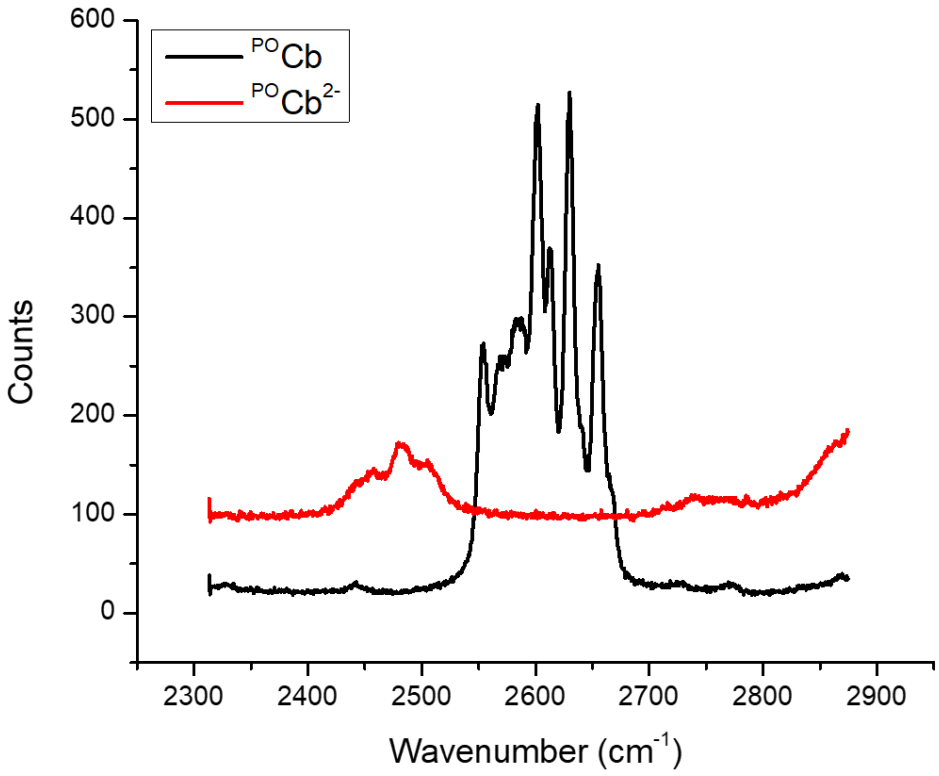

Figure 3.6: Raman spectra of powder ^{PO}Cb and ^{PO}Cb^{2-} ([CoCp$_2^*$]$_2$[^{PO}Cb])

We were interested in electrochemically characterizing **^{PO}Cb-Pyr** to ensure the reversibility for the two-electron reduction to **^{PO}Cb-Pyr^{2-}** and oxidation back to **^{PO}Cb-Pyr**. **^{PO}Cb-Pyr** was only sparingly soluble in organic solvents, so we ran CVs on **^{PO}Cb-Pyr^{2-}**. Since we had not previously taken CVs starting with a *nido* species, we first ran CVs on the unsubstituted **^{PO}Cb^{2-}** to have as comparison.

The CVs of **^{PO}Cb^{2-}** using a GC working electrode matched the CVs for **^{PO}Cb**. [19] It retained the $E_{1/2}$ value of -0.994 V vs Fc/Fc$^+$ in MeCN 0.1 M [Bu$_4$N][PF$_6$](Figure 3.7a). We performed Randles–Ševčík analysis to determine the diffusion coefficients and obtained: 5.19 × 10^{-6} cm^2/s for **^{PO}Cb^{2-}** and 1.75 × 10^{-6} cm^2/s for **^{PO}Cb** (Figure 3.7c-d). The value for the diffusion coefficient of **^{PO}Cb**, however, may be off due to some irreversibility of the complex. The correlation coefficient R^2 for this analysis was low at 0.997 and some break from linearity

can be seen in the plot at the low and high scan rates. We also acquired CVs of the ^{PO}**Cb**$^{2-}$ with a Pt working electrode and observed a more irreversible redox behavior (Figure 3.7b). The peak oxidation potential shifted anodically while the reduction feature is shifted cathodically and was diminished in current. This suggests that the redox of the carborane is not an outer sphere event with the Pt electrode.

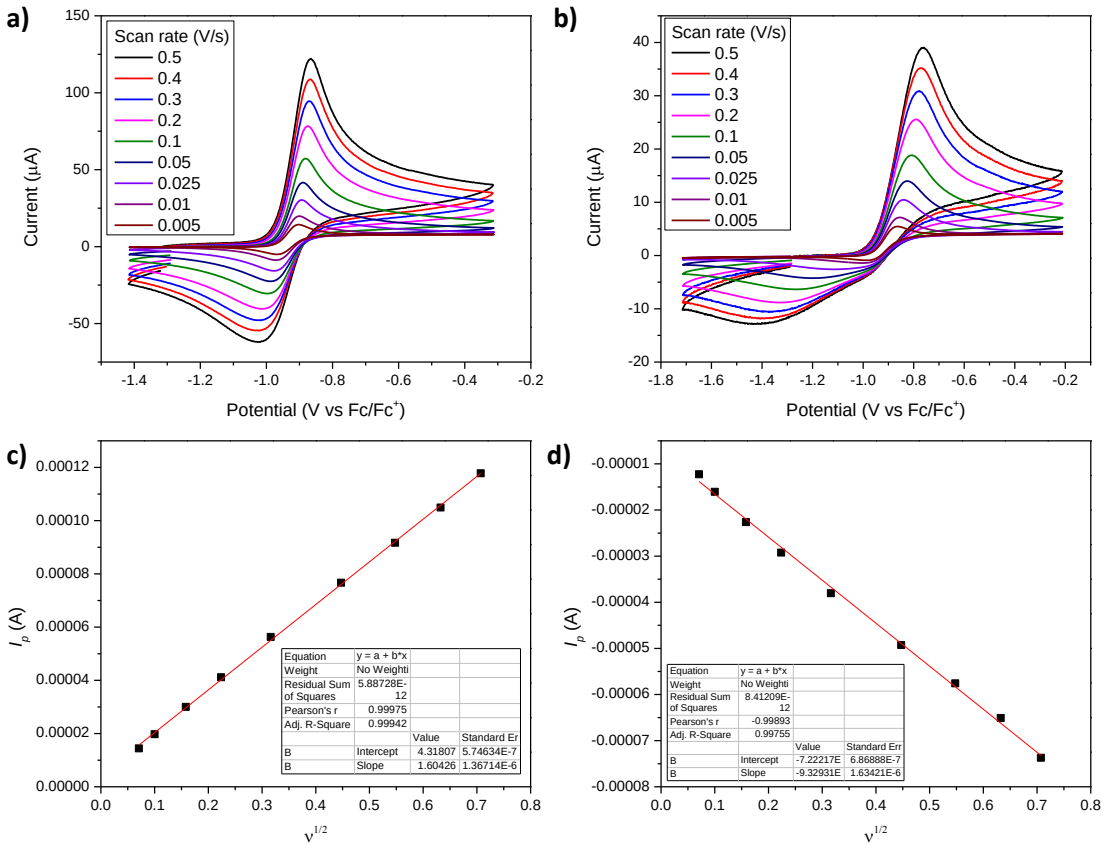

Figure 3.7: CVs of 1.31 mM [$CoCp^*_2$]$_2$[^{PO}Cb] starting at -0.3 V vs OCP taken in MeCN with 0.1 M [Bu_4N][PF_6] supporting electrolyte Pt counter electrode, and Ag/AgOTF reference electrode. a) 3 mm GC electrode b) 2 mm Pt. electrode. c) Randles–Ševčík analysis of oxidation with GC d) Randles–Ševčík analysis of reduction with GC

^{PO}**Cb-Pyr**$^{2-}$ had an $E_{1/2}$ value of -0.879 V vs Fc/Fc^+ in MeCN 0.1 M [Bu_4N][PF_6] using GC (Figure 3.8a), which is slight anodic shift compared to ^{PO}**Cb**$^{2-}$. We also performed a

Randles–Ševčík analysis to determine the diffusion coefficients of 4.82×10^{-6} cm^2/s for the $^{PO}Cb\text{-}Pyr^{2-}$ and 4.06×10^{-6} cm^2/s for the **^{PO}Cb-Pyr** (Figure 3.8c-d). The same issues in the Randles–Ševčík analysis that occurred for the **^{PO}Cb** measurement also happened to the **^{PO}Cb-Pyr**. The CVs taken with the Pt working electrode for **^{PO}Cb-Pyr^{2-}** also became more irreversible like the CVs of $^{PO}Cb^{2-}$ with Pt (Figure 3.8b).

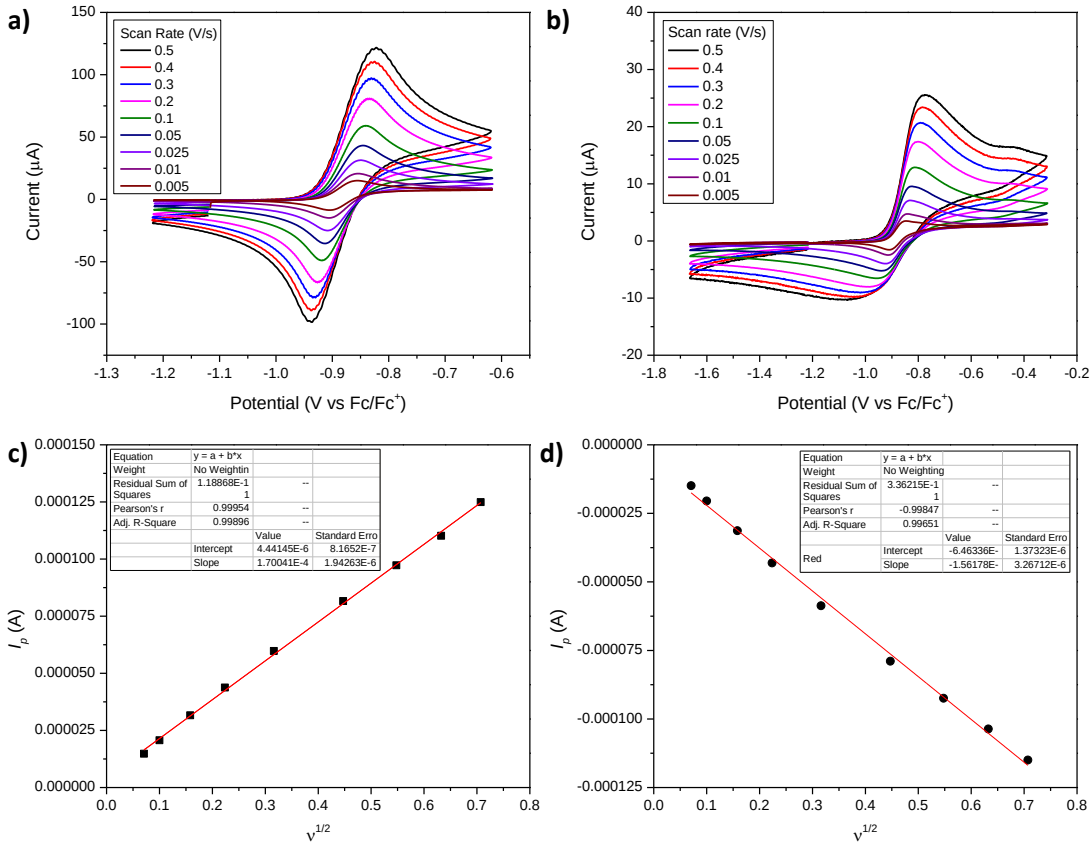

Figure 3.8: CVs of $[CoCp^*_2]_2[^{PO}Cb\text{-}Pyr]$ starting at -0.3 V vs OCP taken in MeCN with 0.1 M $[Bu_4N][PF_6]$ supporting electrolyte Pt counter electrode, and Ag/AgOTF reference electrode. a) 3 mm GC electrode (1.44 mM $[CoCp^*_2]_2[^{PO}Cb\text{-}Pyr]$) b) 2 mm Pt electrode (1.32 mM $[CoCp^*_2]_2[^{PO}Cb\text{-}Pyr]$) c) Randles–Ševčík analysis of oxidation with GC d) Randles–Ševčík analysis of reduction with GC

CVs with UO_2^{2+} and *nido*-carboranes in solution together were ran to test if coordination could be observed by shifts in the redox potentials. We made solutions of approximately 1:1 *nido* carborane to UO_2Cl_2 or $UO_2(NO_3)_2$ in MeCN with 0.1 M $[Bu_4N][PF_6]$ supporting electrolyte. CVs of these solutions were taken using a GC working electrode.

^{PO}**Cb**$^{2-}$ with equimolar UO_2Cl_2 in solution we observed a significant decrease in current response and an anodic shift of the oxidation peak by 0.515 V (Figure 3.9a). The reduction peak also had a diminished current response and shifted anodic by 0.306 V, compared to when no UO_2Cl_2 was present. The decreased current response and change in reduction potential is likely due to the coordination of UO_2Cl_2 to the ^{PO}**Cb**$^{2-}$ in solution. The oxidation of ^{PO}**Cb**$^{2-}$ shifted anodically by 0.408 V when $UO_2(NO_3)_2$ was present (Figure 3.9a). The reduction back, however, differed a lot from the response with UO_2Cl_2. Two separate reduction events were recorded at -0.682 and -1.364 V vs Fc/Fc^+ when $UO_2(NO_3)_2$ was in solution. This may be due to the $UO_2(NO_3)_2$ coordinated species being less reversible or potentially due to a reduction event related to $UO_2(NO_3)_2$.

The shifts in the redox potentials for ^{PO}**Cb-Pyr**$^{2-}$ with equimolar UO_2Cl_2 and $UO_2(NO_3)_2$ were similar to each other. The anodic shift observed for oxidations was 0.407 V for UO_2Cl_2 and 0.435 V for $UO_2(NO_3)_2$ (Figure 3.9b). The reduction events were barely shifted by the addition of UO_2Cl_2 or $UO_2(NO_3)_2$ to the solution. Overall, the *in-situ* coordination of UO_2^{2+} is likely the reason for the shifts in potentials observed for ^{PO}**Cb**$^{2-}$ and ^{PO}**Cb-Pyr**$^{2-}$ with UO_2Cl_2 or $UO_2(NO_3)_2$ present.

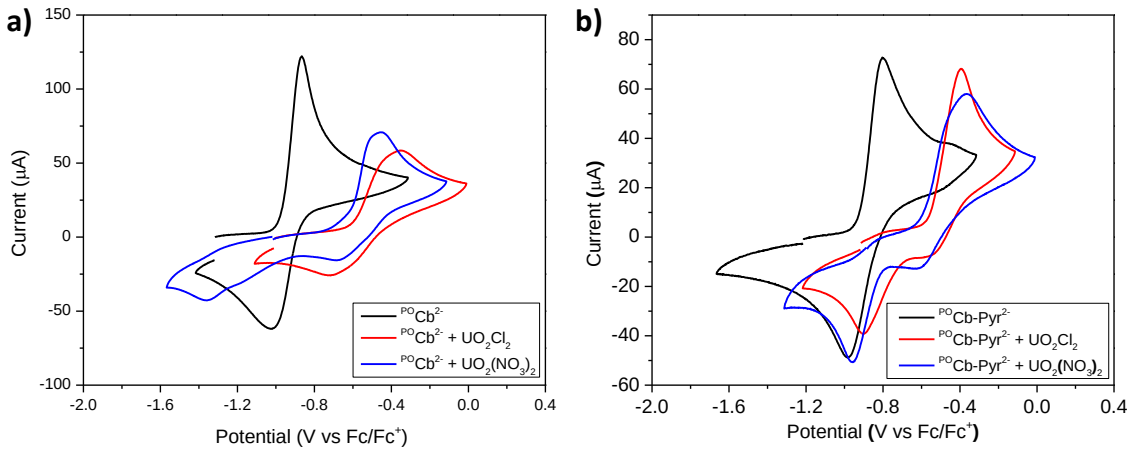

Figure 3.9: CVs of $[CoCp^*_2]_2[^{PO}Cb]$ and $[CoCp^*_2]_2[^{PO}Cb\text{-}Pyr]$ with UO_2^{2+} starting at -0.3 vs OCP with a 0.5 V/s scan rate taken in MeCN with 0.1 M $[Bu_4N][PF_6]$ supporting electrolyte, GC working electrode, Pt counter electrode, and Ag/AgOTF reference electrode. a) 1.31 mM $[CoCp^*_2]_2[^{PO}Cb]$, 1.31 mM $[CoCp^*_2]_2[^{PO}Cb]$ and 1.32 mM UO_2Cl_2, and 1.31 mM $[CoCp^*_2]_2[^{PO}Cb]$ and 1.41 mM $UO_2(NO_3)_2$ b) 1.32 mM $[CoCp^*_2]_2[^{PO}Cb\text{-}Pyr]$, 1.32 mM $[CoCp^*_2]_2[^{PO}Cb\text{-}Pyr]$ and 1.32 mM UO_2Cl_2, and 1.32 mM $[CoCp^*_2]_2[^{PO}Cb\text{-}Pyr]$ and 1.41 mM $UO_2(NO_3)_2$

3.2.2 Indium Tin Oxide Films

We first approached the development of carborane functionalized electrodes using indium tin oxide (ITO) films on glass. This idea was sparked by Jenny Yang's work demonstrating pyrenylferrocene immobilization using π-π interactions onto ITO electrodes with a monolayer of pyrene (ITO|Pyr|Pyrenylferrocene). These ITO|Pyr|Pyrenylferrocene electrodes demonstrated faster electron transfer rates over vinylferrocene covalently bonded to the surface of ITO.[17] We wanted to apply this technique to make an ITO electrode capable of generating the *nido* carborane electrochemically on the surface for heterogeneous capture.

ITO was functionalized with **^{PO}Cb-Pyr** by adapting a literature procedure (Figure 3.10).[17] ITO sheets were first washed by sonicating in DCE, acetone and methanol before transferring them into the glovebox. The ITO was then functionalized to have a layer of pyrene on the surface by heating the ITO to 80 ^{o}C in a 1 mM 1-vinylpyrene toluene solution for 24 hours under nitrogen (ITO|Pyr). This thermal method of functionalization with alkenes and alkynes has been shown to generate covalently bonded monolayers on surfaces rather than polymerization.[21] After 24 hours, the solution is cooled and washed with toluene and DCM to remove excess reagent. The ITO|Pyr was then functionalized further by submerging the electrode into a 1 mM solution of **^{PO}Cb-Pyr** for 12 hours (ITO|Pyr|^{PO}Cb-Pyr). Excess **^{PO}Cb-Pyr** was rinsed of with acetonitrile and vacuum was applied to dry the electrode. The electrodes were characterized by X-ray photoelectron spectroscopy (XPS) to show the presence of the carborane on the electrode.

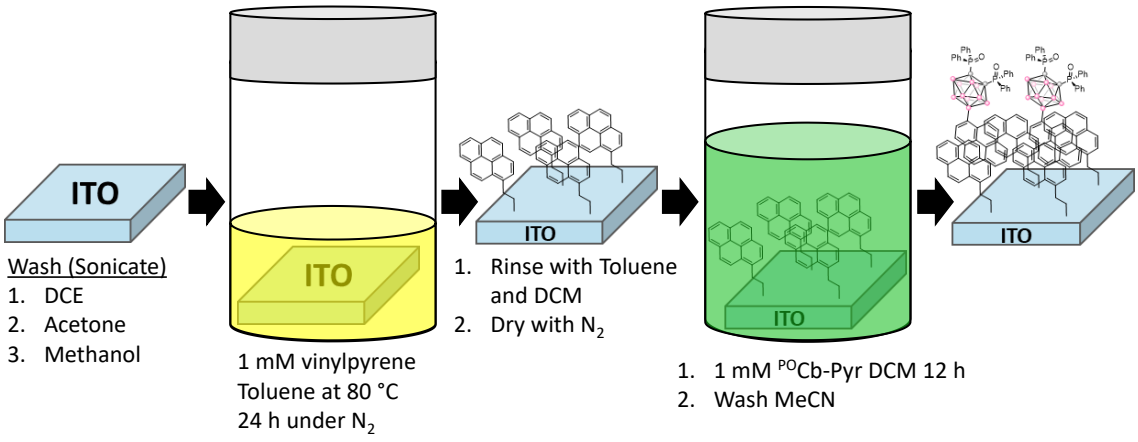

Figure 3.10: Functionalization scheme for ITO to generate ITO|Pyr|^{PO}Cb-Pyr

As a control we took the XPS spectrum of cleaned ITO. The spectrum showed the expected peaks for In, Sn, and O as present (Figure 3.11). Interestingly a Cl contamination is

observed in the spectrum. This may have come from the wash with DCE. The carbon signal is not unexpected as dust is typically present on most samples which gives a source of carbon.

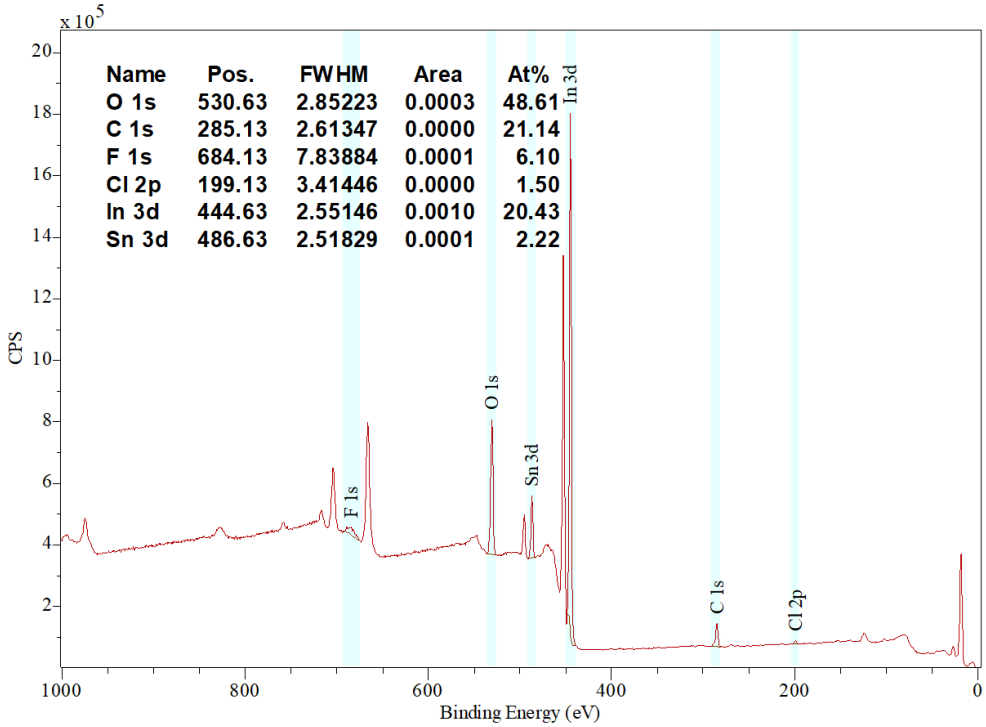

Figure 3.11: XPS spectrum of ITO

The XPS spectrum of the ITO|Pyr sheets had a similar spectrum. The spectrum showed the same expected peaks for In, Sn, and O, as well as the same Cl contamination (Figure 3.12). The counts on the carbon signal did increase slightly which could be due to the increased presence of carbon on the surface from the pyrene attachment or from different levels of dust.

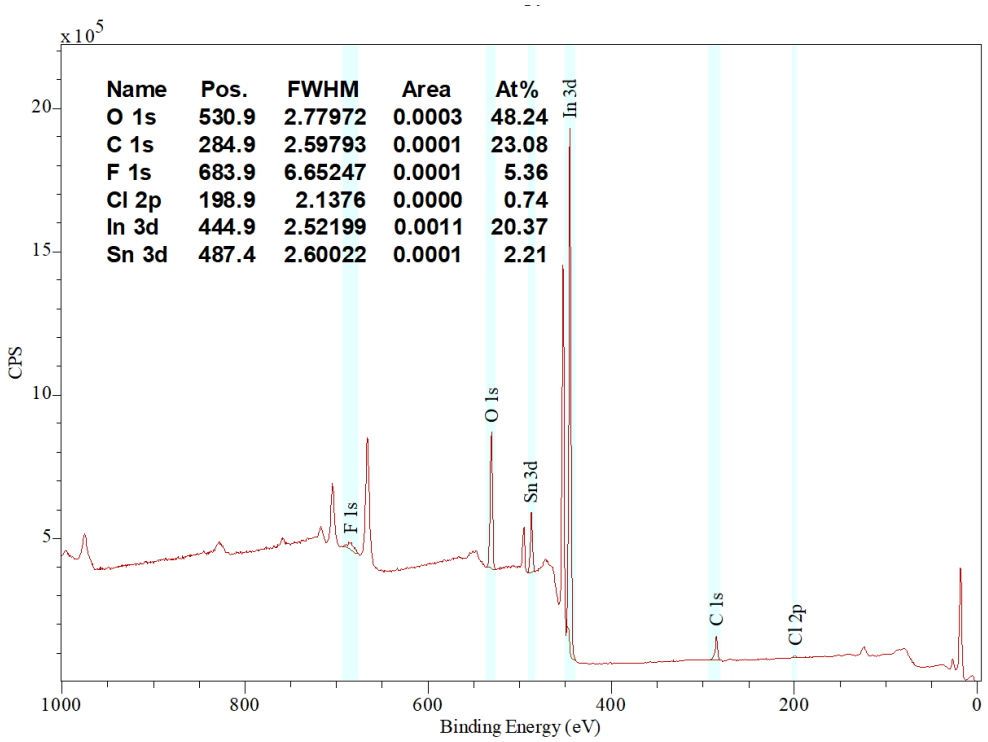

Figure 3.12: XPS spectrum ITO|Pyr

The XPS survey spectrum of ITO|Pyr|^{PO}Cb-Pyr had all the same signals as ITO and ITO|Pyr with the addition of boron and phosphorous signals (Figure 3.13a). We ran a smaller window with higher resolution for 10 scans in the region around B and P signals to better resolve the peaks. In this narrow spectrum, the signals for B and P were more resolved, but the counts were still extremely low likely due to the low amount of **^{PO}Cb-Pyr** on the surface of the electrode (Figure 3.13b).

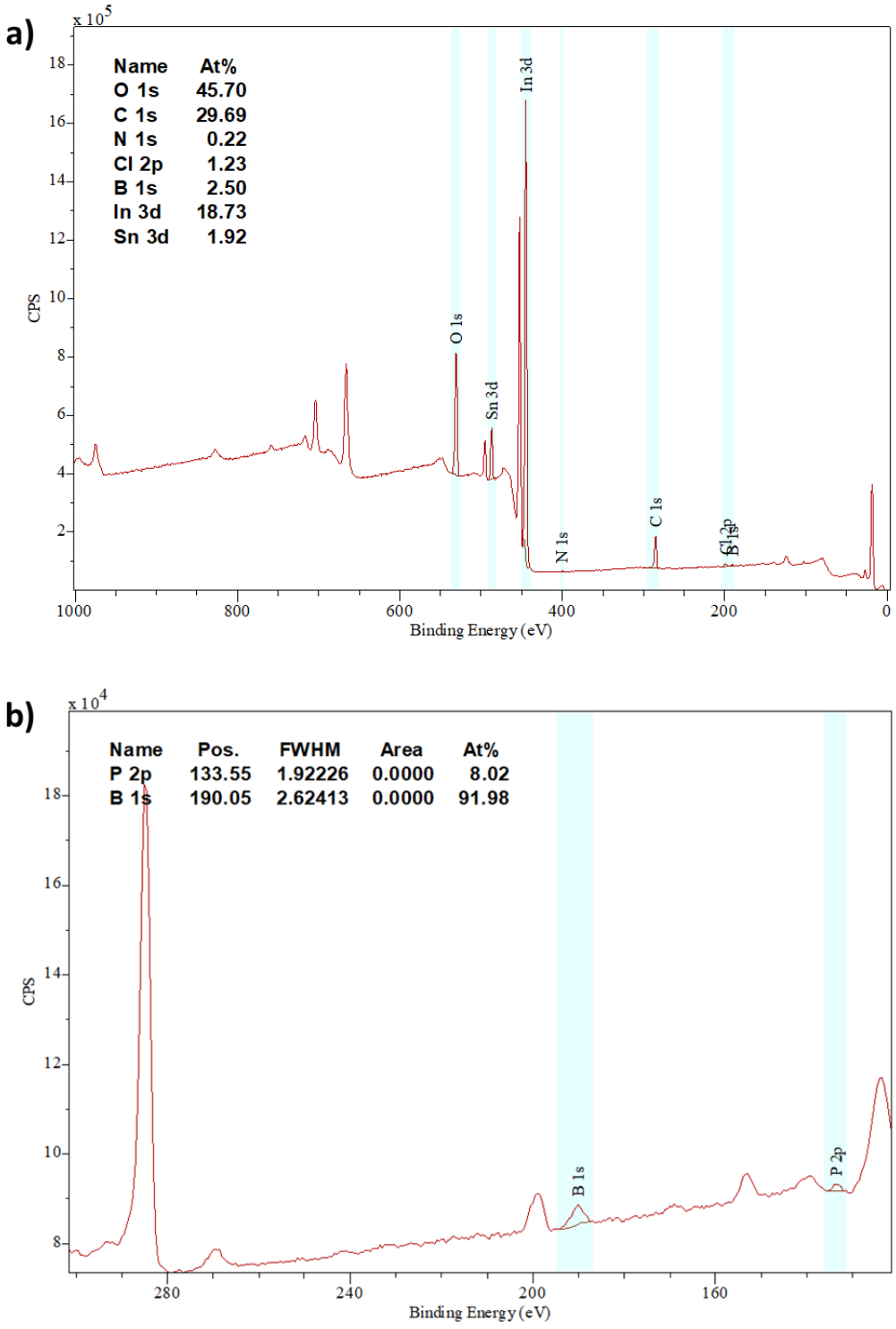

Figure 3.13: XPS Spectra of ITO|Pyr|^{PO}Cb-Pyr a) survey spectrum b) narrow spectrum

CVs were taken on the different ITO electrodes to determine if the **^{PO}Cb-Pyr^{2-}** species could be electrochemically generated on the surface of the ITO|Pyr|^{PO}Cb-Pyr electrode. The CVs of the films were taken in an aqueous 0.1 M KCl solution. The ITO CVs had a high current density and large irreversible redox event (Figure 3.14a). The ITO|Pyr CVs overall had a significantly lower current density compared to the pure ITO and a more defined reductive event around -0.5 V vs SCE and oxidation around -0.25 V vs SCE (Figure 3.14b). The lower current density compared to ITO could be due to slower diffusion of ions to the surface of the electrode due to the addition of the pyrene layer. The reduction and oxidation events observed were not consistent and did not correlate with scan rate. The CVs of ITO|Pyr|^{PO}Cb-Pyr had a similar response to ITO|Pyr, with no clear redox features from **^{PO}Cb-Pyr** (Figure 3.14c).

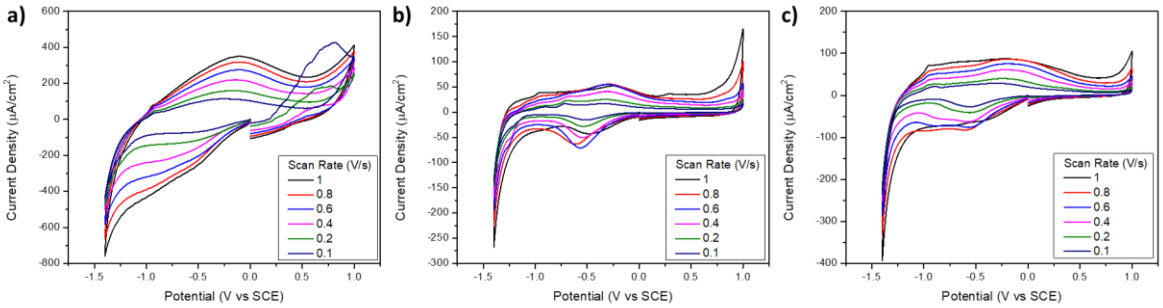

Figure 3.14: CVs of ITO sheets at variable scan rates in an aqueous 0.1 M KCl solution with a Pt counter electrode and SCE reference electrode. a) ITO b) ITO|Pyr c) ITO|Pyr|^{PO}Cb-Pyr

A notable change in coloration of the ITO electrodes was observed after running the CVs in the aqueous solution. Normally when the ITO is transparent when held up to a paper sheet, but after the CVs the electrodes (ITO, ITO|Pyr, and ITO|Pyr|^{PO}Cb-Pyr) turned a brown color on the parts exposed to the aqueous solution (Figure 3.15). This further indicated that

an irreversible redox event is occurring on the ITO. Due lack of an observable redox event from **^{PO}Cb-Pyr**, and the change in structure to the ITO under reductive potentials, the ITO functionalized electrodes were not further pursued.

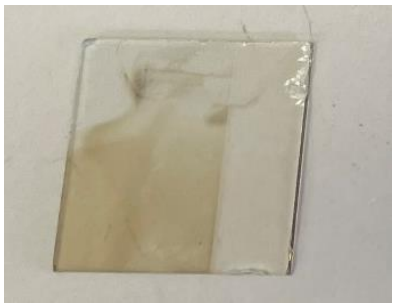

Figure 3.15: ITO electrode after CVs in aqueous solutions

3.2.3 Graphite Functionalization

We next investigated functionalizing graphite powder with **^{PO}Cb-Pyr**. This was accomplished by adding 20 mg of graphite powder to a 1.5 mM **^{PO}Cb-Pyr** chloroform solution and tip sonicating for 30 minutes, while submerged in an ice bath. This solution was then briefly centrifuged to form a pellet of the graphite at the bottom of the centrifuge tube and allow the **^{PO}Cb-Pyr** chloroform solution to be decanted off. The graphite was then washed with DCM to remove excess **^{PO}Cb-Pyr** that did not adhere to the surface of the graphite. The DCM was decanted off after centrifuging again to form a pellet (graphite-^{PO}Cb-Pyr). The isolated graphite-^{PO}Cb-Pyr was then dried under vacuum overnight before an XPS spectrum was taken.

Graphite that underwent the same functionalization process without **^{PO}Cb-Pyr** present had signals for C, N, O and Cl in the XPS spectrum (Figure 3.16a). The XPS spectra of the graphite-^{PO}Cb-Pyr powder showed the addition of B and P to the graphite (Figure 3.16b-c).

Similar to the ITO|Pyr|^{PO}Cb-Pyr XPS spectra, the signals for B and P were extremely low. This suggests only a minimal amount of **^{PO}Cb-Pyr** adhered to the graphite surface during the functionalization process.

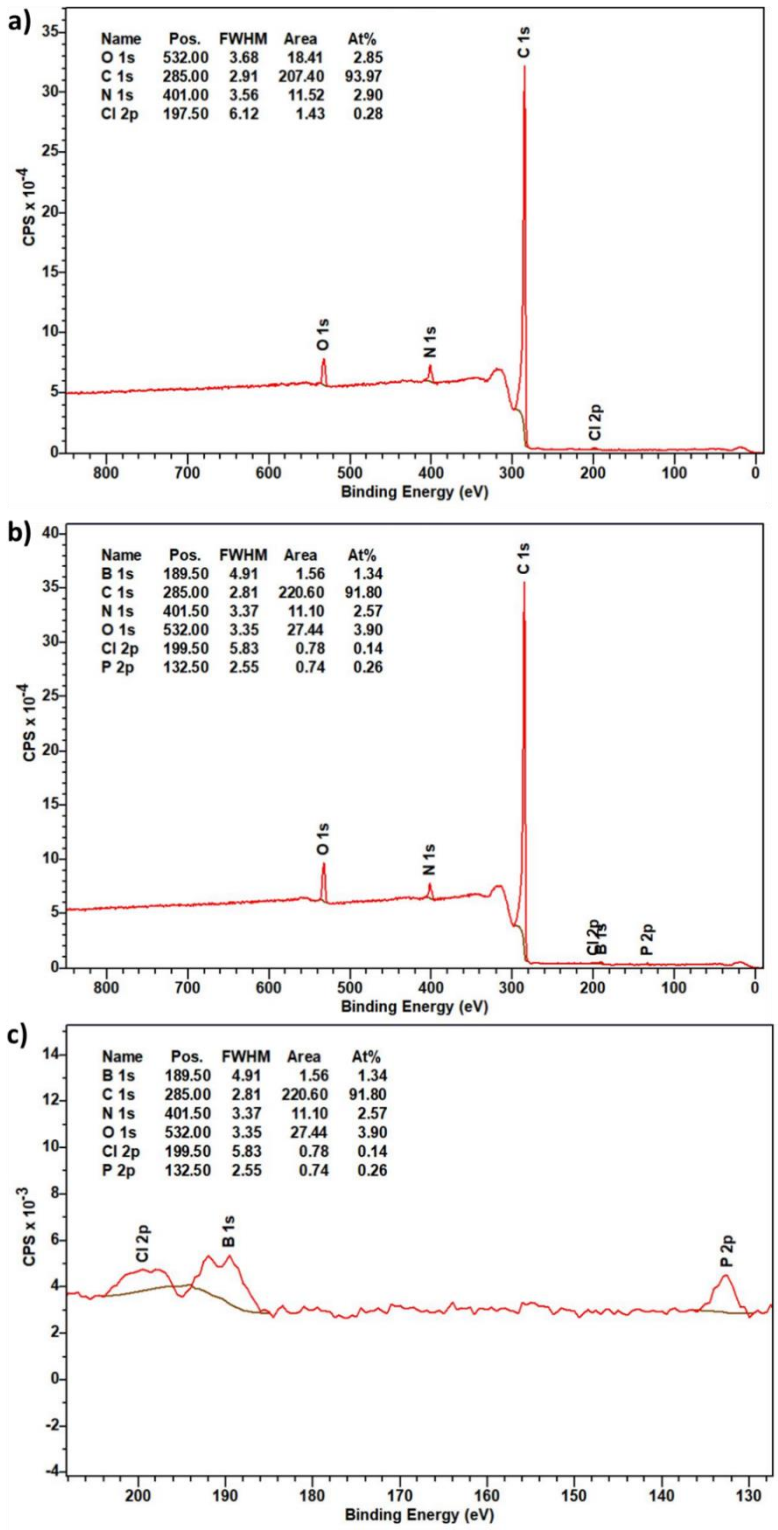

Figure 3.16: XPS spectra of graphite and graphite-^{PO}Cb-Pyr a) Survey spectrum of graphite b) Survey spectrum of graphite-^{PO}Cb-Pyr c) Narrow spectrum of graphite-^{PO}Cb-Pyr

Films of graphite and graphite-^{PO}Cb-Pyr were made on GC working electrodes to determine if the **^{PO}Cb-Pyr** adhered to graphite remained electrochemically active. Graphite and graphite-^{PO}Cb-Pyr were suspended in DCM by sonication. An aliquot of the suspensions were drop casted onto a freshly polished GC working electrodes to add ~2 mg of the graphite or graphite-^{PO}Cb-Pyr to the surface and left to dry open to air (GC|graphite, GC|graphite-^{PO}Cb-Pyr) (Figure 3.17a). These films covered the entire electrode surface including the GC and the plastic insulator around the working area (Figure 3.17b). CVs and DPVs were taken of the films inside a wet glove box in 0.1 M KCl aqueous solutions.

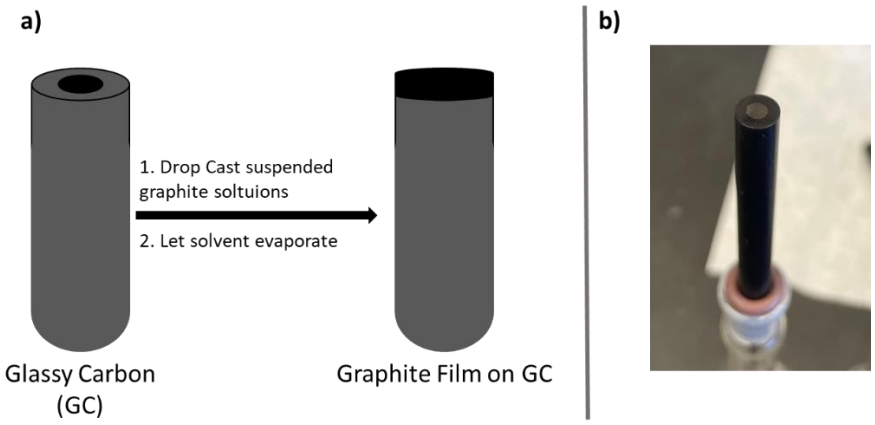

Figure 3.17: Graphite films for CV/DPV a) Scheme for making graphite films b) Picture of graphite film

The CVs of GC|graphite film appeared to be mostly capacitive, with a possible oxidation event around 0.3 V vs SCE (Figure 3.18a). The GC|graphite-^{PO}Cb-Pyr film had a redox couple with an $E_{1/2}$ -0.422 V vs SCE (Figure 3.18b). This redox event had an extremely low current response that was barely above the capacitive current.

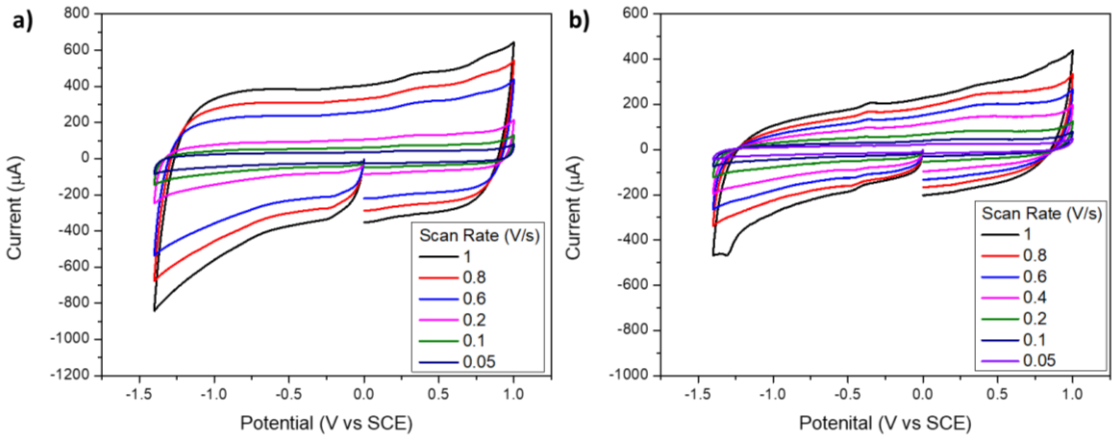

Figure 3.18: CVs of graphite films on GC at variable scan rates in an aqueous 0.1 M KCl solution with a Pt counter electrode and an SCE reference electrode. a) GC|graphite b) GC|graphite-^{PO}Cb-Pyr

The GC|graphite-^{PO}Cb-Pyr redox event was more clearly observed in the DPVs of the film (Figure 3.19b). These CVs and DPVs of GC|graphite-^{PO}Cb-Pyr demonstrated that the heterogenized **^{PO}Cb-Pyr** remained electrochemically active. This suggested that formation of **^{PO}Cb-Pyr^{2-}** on the surface of electrodes was possible. We did not further pursue the functionalization of graphite due to the low loading and current response of **^{PO}Cb-Pyr**.

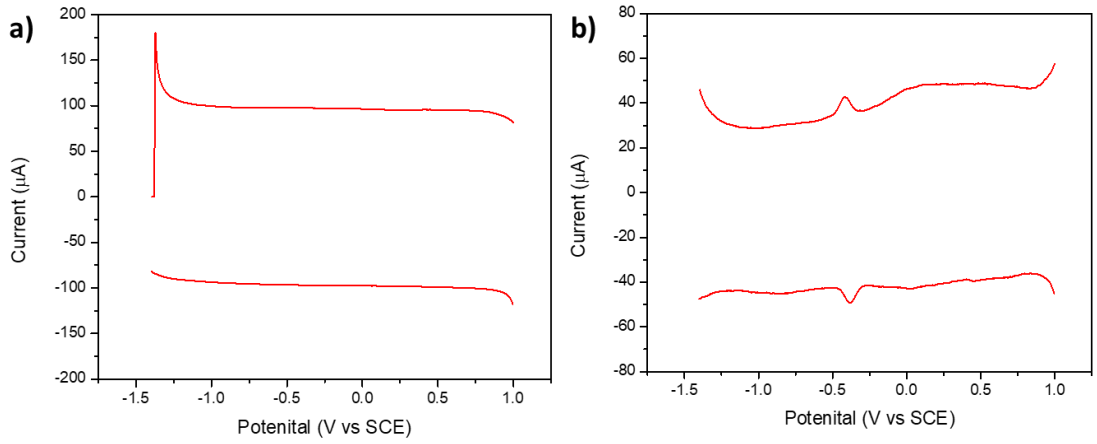

Figure 3.19: DPVs of graphite films on GC in an aqueous 0.1 M KCl solution with a Pt. counter electrode and SCE reference electrode. a) GC|graphite b) GC|graphite-^{PO}Cb-Pyr.

3.2.4 Films on Glassy Carbon and Carbon Fiber

To achieve higher current density responses, we switched to making films of the carboranes directly on electrodes. We used the bottom faces of GC rods that had been polished to a mirror finish (0.1935 cm^2). GC rods were used for these film experiments because the whole area of the film could be exposed to the working electrode. In comparison if the films were made on standard GC working electrodes some of the film would be on the insulator around the actual GC surface and not exposed directly to the working area. Films of carborane were made by drop casting 10 µL of 1 mM carborane (**^{PO}Cb** or **^{PO}Cb-Pyr**) in DCE onto the GC rod surface and left to evaporate open to air (GC|^{PO}Cb or GC|^{PO}Cb-Pyr) (Figure 3.20).

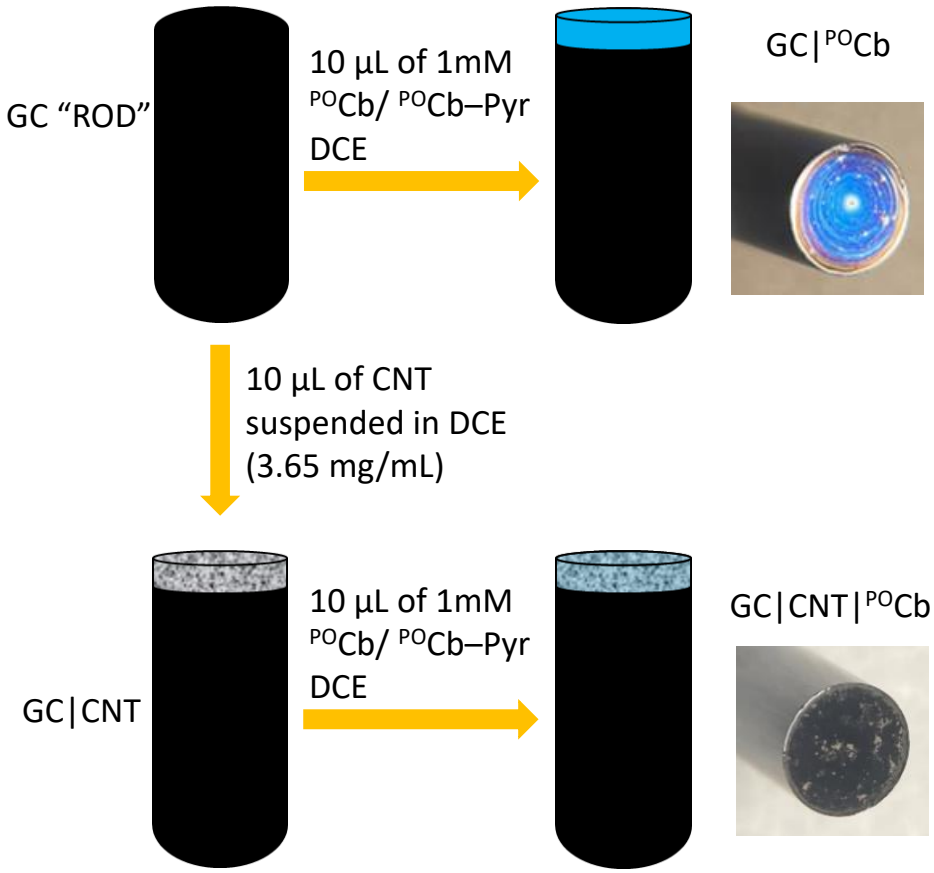

Figure 3.20: Scheme for drop casting films on GC rods with 0.1935 cm^2 working area

Films of single-walled carbon nanotubes (CNTs) on GC were also made using drop casting. CNTs were suspended in DCE by sonication for 30 minutes to produce a 3.65 mg/mL solution. 10 µL of this solution was drop casted onto the GC rod and left to dry open to air (GC|CNT). To these GC|CNT 10 µL of 1 mM carborane (**^{PO}Cb** or **^{PO}Cb-Pyr**) in DCE was drop casted onto the film and left to evaporate open to air (GC|CNT|^{PO}Cb or GC|CNT|^{PO}Cb-Pyr) (Figure 3.20).

Raman spectra of the GC rod and GC|^{PO}Cb films were taken but no differences were observed (Figure 3.21). We adjusted the power and focusing but could not observe the B-H signal like we had previously observed in the spectrum of the powdered **^{PO}Cb** (Figure 3.6).

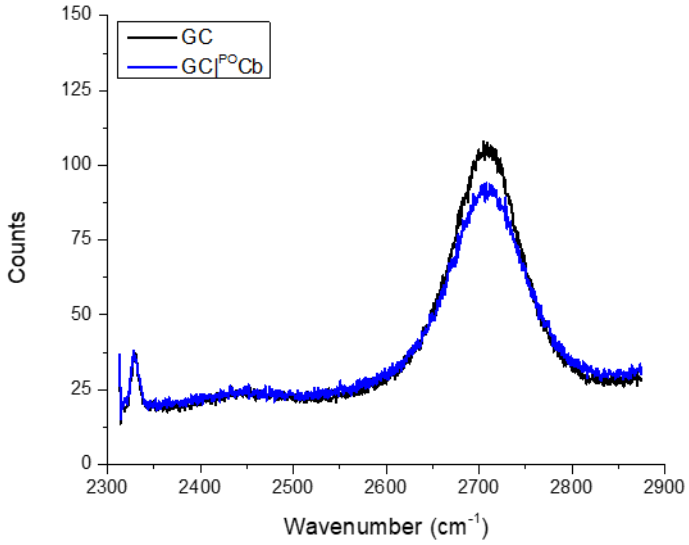

Figure 3.21: Raman spectra of GC and GC|^{PO}Cb film

We turned next to consecutive CVs of the GC|^{PO}Cb films to test the heterogeneous electrochemical behaviour. While the first CV of the film in 0.1 M aqueous KCl showed no evident electrochemical response in the first scan, we observed a quasi-reversible redox feature grow in over 20 scans, with a formal reduction potential ($E_{1/2}$) of -0.55 V vs SCE (Figure 3.22a). This value closely aligns with the solution state reduction potential of **^{PO}Cb** in acetonitrile (-0.994 V vs $Fc^+|Fc$ ≅ -0.594 V vs SCE), upon accounting for the solvent and reference electrode used.[19, 22] In solution, **^{PO}Cb** undergoes a chemically reversible 2 e^- reduction concurrent with C–C bond breaking to form the **^{PO}Cb^{2-}**, which can in turn undergo a 2e^- oxidation back to **^{PO}Cb**.[19] The observed redox events on GC|^{PO}Cb likely corresponds to the heterogeneous analog given the observed potentials. The peak currents also remained relatively stable beyond 20 scans, with a linear dependence on the scan rate, indicative of a non-diffusional Faradaic response (i.e., pseudo-capacitance (Figure 3.36). These CVs demonstrate the GC|^{PO}Cb film is in ionic contact with the bulk aqueous solution – a surprising

phenomenon considering the low polarity and hydrophobicity of *Ortho*-carborane in general.[23-25]

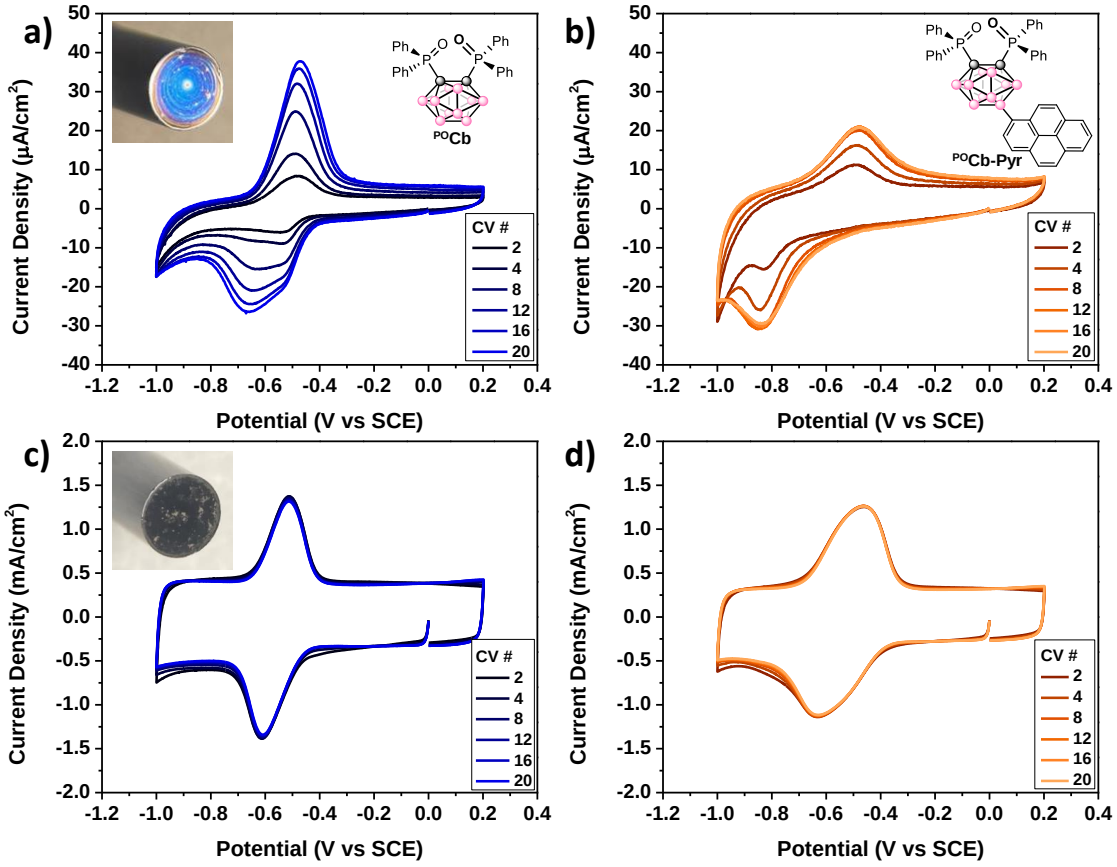

Figure 3.22: CVs of carborane films (10 nmols) on glassy carbon rods in 0.1 M KCl aqueous solutions at a scan rate of 0.1 V/s. a) GC| ^{PO}Cb (picture insert of film) b) GC| ^{PO}Cb-Pyr c) GC|CNT| ^{PO}Cb (picture insert of film) d) GC|CNT| ^{PO}Cb-Pyr.

We were interested in investigating if the addition of π-π stacking capability using **^{PO}Cb-Pyr** would enhance the current density of the films. Films of **^{PO}Cb-Pyr** on a GC electrode (GC|^{PO}Cb-Pyr) had similar electrochemical behaviour to the GC|^{PO}Cb films, but

with lower peak current densities and a higher peak to peak separation of 0.372 V compared to 0.195 V for the GC|^{PO}Cb films (Figure 3.22a-b).

While both GC|^{PO}Cb and GC|^{PO}Cb-Pyr films were successfully generated on GC surfaces and subsequent *closo*↔*nido* redox events were observed, it became clear from the observed current densities (μA/cm^2, Figure 3.22a-b (y-axes)) that there was low surface coverage which would ultimately lead to a poor heterogeneous absorption. To increase the areal density of **^{PO}Cb** on the electrode, we added a layer of single walled carbon nanotubes (CNT) on the GC electrodes. This has been demonstrated with heterogeneous catalyst systems to reduce aggregation and increase dispersion of molecules on the surface, especially for catalysts containing π-π stacking functional groups, such as pyrene.[11, 26] Unlike the previous films, the GC|CNT|^{PO}Cb and GC|CNT|^{PO}Cb-Pyr films did not require conditioning CVs to facilitate the emergence of Faradaic current response. Both the GC|CNT|^{PO}Cb and GC|CNT|^{PO}Cb-Pyr films saw significant increases in current densities (mA/cm^2 vs μA/cm^2) and lower peak to peak separation (0.1 V and 0.174 V, respectively) compared to the non-CNT counter parts (Figure 3.22 c-d vs. a-b). Over the course of 20 CV scans, we noted the GC|CNT|^{PO}Cb-Pyr to be more stable than the GC|CNT|^{PO}Cb film which had a decay in peak current density of the oxidation and reduction that we attribute to the loss of **^{PO}Cb** from the surface. We ascribe the higher stability of the GC|CNT|^{PO}Cb-Pyr film to the π-π stacking with the CNT in the GC|CNT|^{PO}Cb-Pyr film.

We were interested in observing UO_2^{2+} coordination to the films *in-situ* using linear sweep voltammetry (LSV). For each film we first ran 20 CVs consecutively to ensure the stability of the GC|^{PO}Cb film. A reductive sweep LSV from 0 to -1 V vs SCE was used to generate the **^{PO}Cb^{2-}** on the surface of the electrode. A subsequent oxidative LSV from OCP

to 0.4 V vs SCE was run to determine the oxidation potential back to **^{PO}Cb** (-0.456 vs SCE) (Figure 3.23). We planned to expose the **^{PO}Cb^{2-}** generated film to a UO_2^{2+} solution, and run subsequent oxidative LSVs to determine if any shift of the oxidation potential back to **^{PO}Cb** occurred, like the shifts observed in solution state CVs (Figure 3.9).

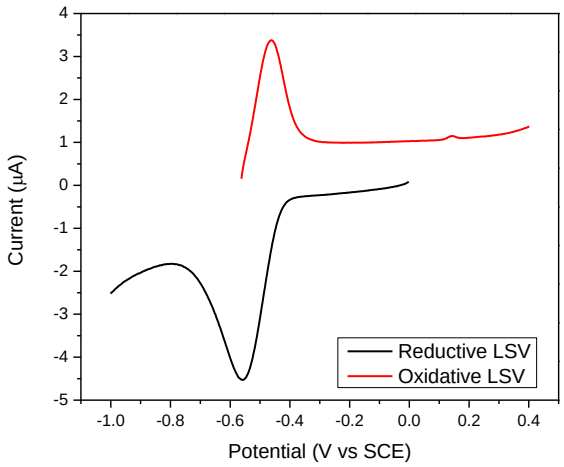

Figure 3.23: LSVs of GC|^{PO}Cb in a 0.1 M KCl aqueous solution.

Before testing UO_2^{2+} coordination, we wanted check the stability of the **^{PO}Cb^{2-}** generated on the surface of the GC|^{PO}Cb electrode. We first tested this with a 5-minute delay, letting the electrode sit in solution for 5 minutes between the reductive LSV and the oxidative LSV. We observed a significant loss in the peak current response with the added delay, dropping from a peak current of 3.4 μA without a delay to 1.1 μA with the 5-minute delay (Figure 3.24a). We ran CVs before and after this test that revealed a loss in current response, which we attribute to the loss of **^{PO}Cb** from the film (Figure 3.24b). We also performed tests that would simulate the movements required for the proposed coordination/capture experiment. After a reductive LSV was run on a GC|^{PO}Cb film, it was removed from the CV cell and dipped it into a vial containing 0.1 M KCl. After a minute in the solution, the electrode was put back into the CV cell and an oxidative LSV starting from OCP was run. No significant

oxidative peak was present in the LSV and a loss in current response for the before and after CVs was also observed (Figure 3.24c-d). These LSVs and CVs suggest the $^{PO}Cb^{2-}$ does not adhere to the surface as well as the ^{PO}Cb. This is not surprising as the charged $^{PO}Cb^{2-}$ would likely be more soluble in water than the non-charged ^{PO}Cb.

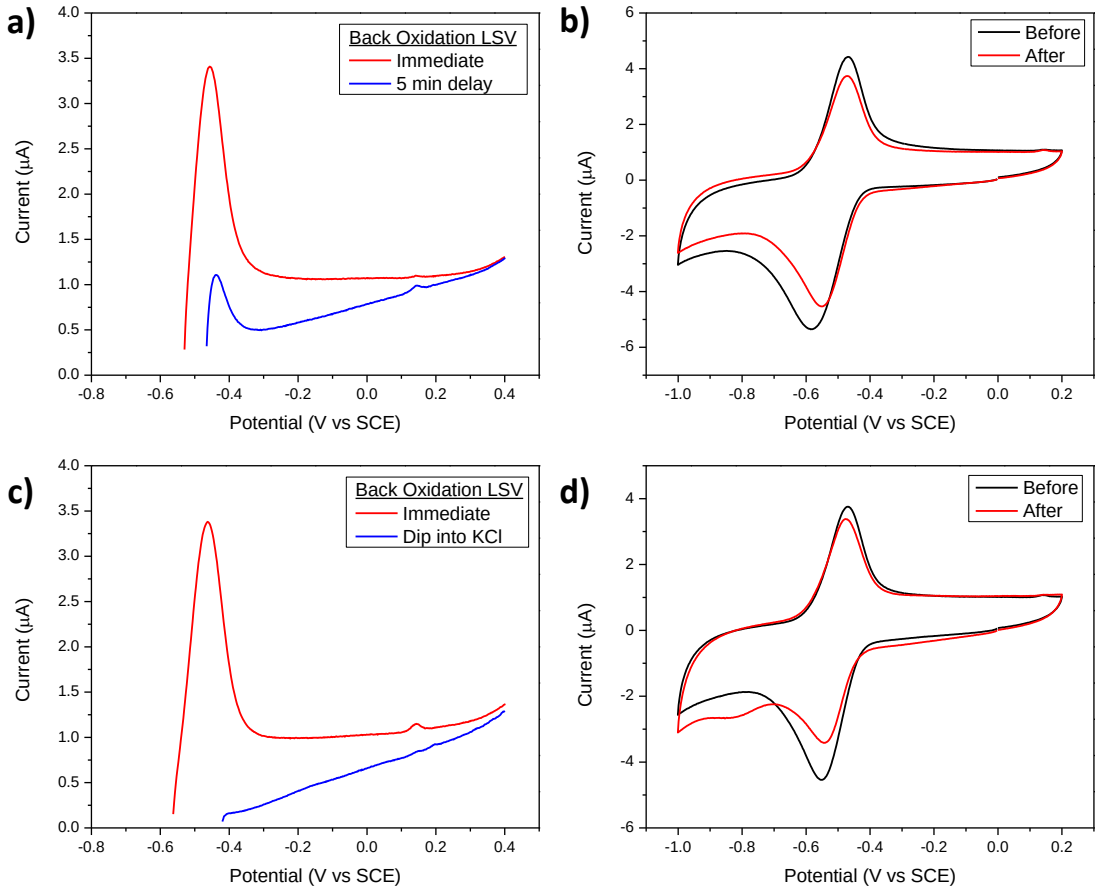

Figure 3.24: Oxidative LSVs starting at OCP and CVs of GC|^{PO}Cb in 0.1 M KCl aqueous solution. a) Immediate LSV versus 5-minute delay LSV. b) CVs before and after 5-minute delay test. c) Immediate LSV versus electrode dip test LSV. d) CVs before and after dip test.

To see if the addition of the CNT layer to the films increased the stability of the surface generated *nido* carborane, we decided to run the same control experiments on GC|CNT|^{PO}Cb-Pyr films. Reductive LSVs with subsequent oxidative LSVs for GC|CNT and GC|CNT|^{PO}Cb-

Pyr films were ran. The GC|CNT reductive LSV had a reduction at -0.23 V vs SCE and the subsequent oxidative LSV had two oxidation peaks at 0.16 and 0.31 V vs SCE (Figure 3.25a). The GC|CNT|^{PO}Cb-Pyr reductive LSV had a reduction peak at -0.59 V vs SCE, with the oxidative LSV having an oxidation at -0.479 V vs SCE from **^{PO}Cb-Pyr** (Figure 3.25b). The oxidative LSV of GC|CNT|^{PO}Cb-Pyr also had oxidation peaks from the CNT layer.

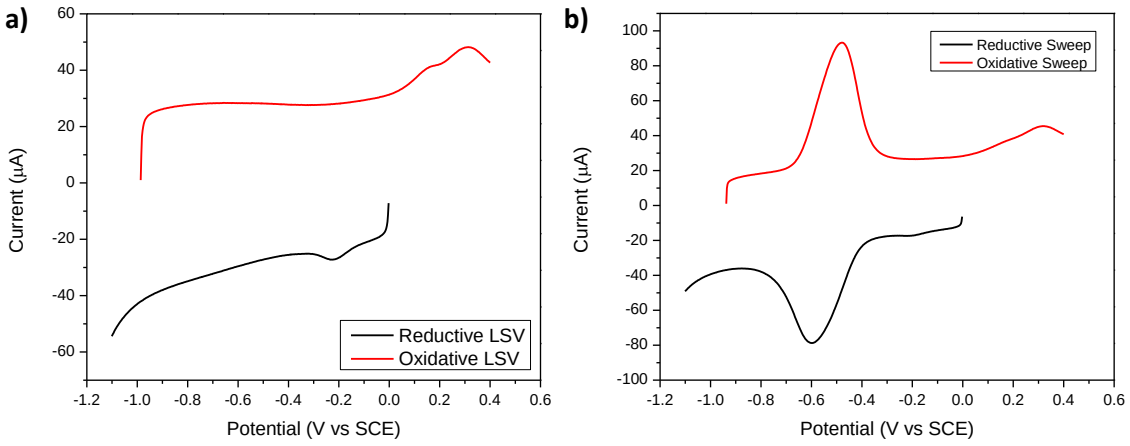

Figure 3.25: LSVs of GC|CNT and GC|CNT|^{PO}Cb-Pyr in 0.1 M KCl aqueous solution. a) Reductive LSV with subsequent oxidative LSV that started at OCP for GC|CNT. b) Reductive LSV with subsequent oxidative LSV that started at OCP for GC|CNT|^{PO}Cb-Pyr

We ran the 5-minute delay between reductive and oxidative LSVs test on the GC|CNT|^{PO}Cb-Pyr film and observed only a minor loss in the peak current for the oxidation, compared to the immediate LSV (Figure 3.26). The dip test for the GC|CNT|^{PO}Cb-Pyr film showed only a small loss in peak current (-17 µA), which was a significant improvement over the GC|^{PO}Cb films stability for the same test (Figure 3.24c). These results showed that the addition of CNT layer and the additional π-π interactions increased the stability of the *nido* carborane generated on the surface of the film.

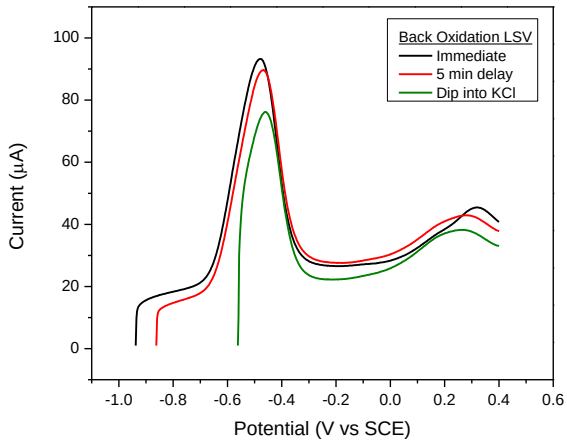

Figure 3.26: Oxidative LSVs after various stability tests of GC|CNT|^{PO}Cb-Pyr starting at OCP in 0.1 M KCl aqueous solutions.

GC|CNT|^{PO}Cb-Pyr coordination and capture of metals was then tested. GC|CNT|^{PO}Cb-Pyr films after reductive LSVs were dipped into 2 mM individual metal aqueous solutions for 30 seconds. Once the electrodes were removed, they were rinsed and put into a fresh 0.1 M KCl solution. Oxidative LSVs of the films starting from their OCP were then run to determine if the oxidation potential had shifted. The GC|CNT|^{PO}Cb-Pyr exposed to Cs^{+} had no significant change to the oxidation potential (Figure 3.27a). The current response was significantly higher than the control LSV, but this is likely due to the individual film properties as the reductive LSV for this film also had a higher current response than the controls reductive LSV. The GC|CNT|^{PO}Cb-Pyr films exposed to separate Nd^{3+} and Sm^{3+} solutions both had a slight shift in the oxidation potential from -0.462 V vs SCE of the control to -0.4 and -0.408 V vs SCE, respectively (Figure 3.27b-c). This potential shift likely indicates the coordination and capture of Nd^{3+} and Sm^{3+} by the GC|CNT|^{PO}Cb-Pyr film. The GC|CNT|^{PO}Cb-Pyr exposed to Th^{4+} had a linear response in current that did not resemble the normal oxidation back to *closo* carborane (Figure 3.27d). The GC|CNT|^{PO}Cb-Pyr exposed to UO_2^{2+} also did not have the carborane

oxidative feature, but rather had a slight change in current response around the oxidation feature of CNTs (Figure 3.27e). The GC|CNT|^{PO}Cb-Pyr exposed to the equimolar mixed metal solution (Cs^{+}, Nd^{3+}, Sm^{3+}, Th^{4+}, UO_2^{2+}) had a response nearly identical to the UO_2^{2+} only exposure (Figure 3.27f). The control GC|CNT exposure to the mixed metal solution also had a similar response to the GC|CNT|^{PO}Cb-Pyr exposure to the mixed metal solution (Figure 3.27f-g). These LSVs suggest that the CNT and the ^{PO}Cb-Pyr both potentially play a role in the coordination of metals to the films from aqueous solutions.

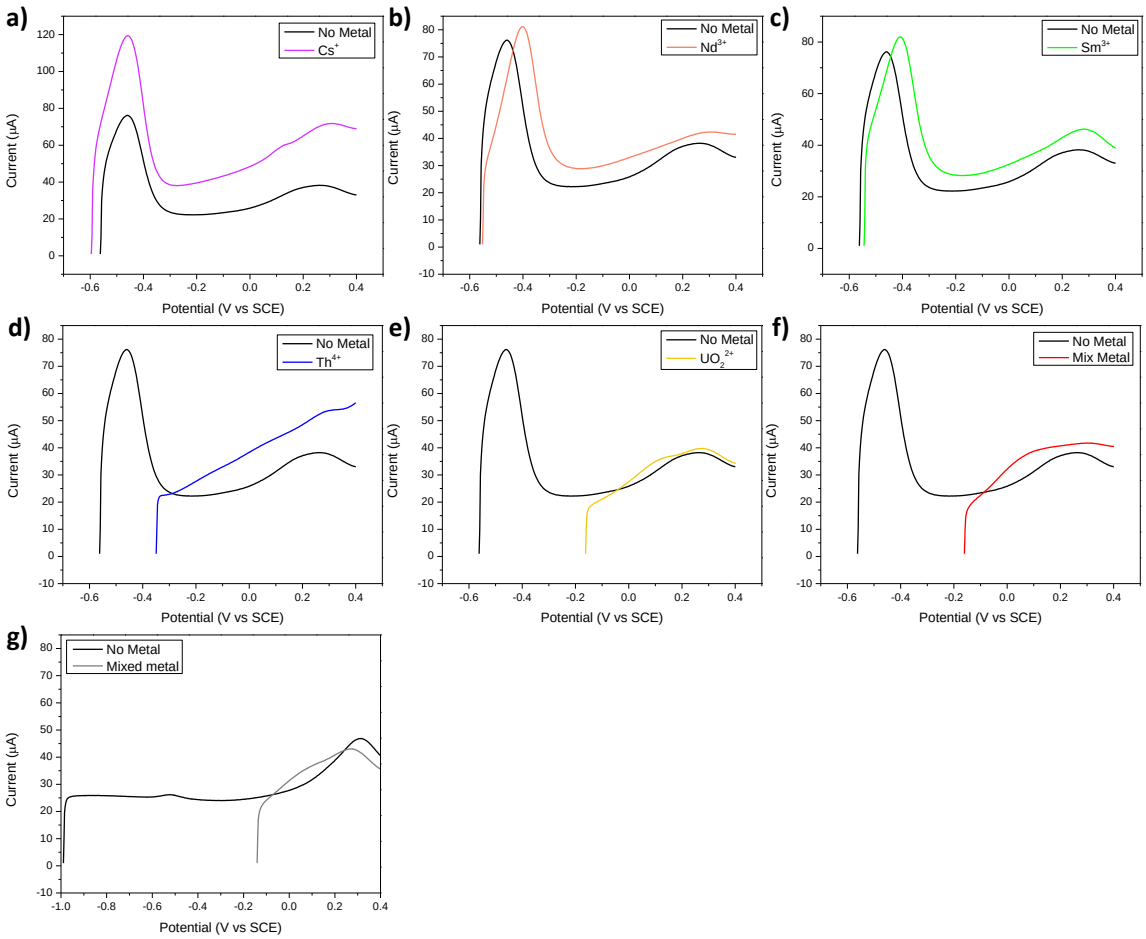

Figure 3.27: Oxidative LSVs of GC|CNT|^{PO}Cb-Pyr and GC|CNT after dipping into various metal solutions starting at OCP in 0.1 M KCl aqueous solutions. Plotted against the KCl dip control a) GC|CNT|^{PO}Cb-Pyr exposure to 2 mM $CsNO_3$ b) GC|CNT|^{PO}Cb-Pyr exposure to 2 mM $Nd(NO_3)_3$ c) GC|CNT|^{PO}Cb-Pyr exposure to 2 mM Sm^{3+} d) GC|CNT|^{PO}Cb-Pyr exposure to 2 mM $Th(NO_3)_4$ e) GC|CNT|^{PO}Cb-Pyr exposure to 2 mM $UO_2(NO_3)_2$ f) GC|CNT|^{PO}Cb-Pyr exposure to 2 mM Mixed (Cs^+, Nd^{3+}, Sm^{3+}, Th^{4+}, UO_2^{2+}). f) GC|CNT exposure to 2 mM mixed metal (Cs^+, Nd^{3+}, Sm^{3+}, Th^{4+}, UO_2^{2+}).

CVs were taken of the GC|CNT|^{PO}Cb-Pyr films after every capture experiment to see if any change in redox features was observed. The films exposed to Cs^+, Nd^{3+}, Sm^{3+} and Th^{4+}

saw no change in the CVs. Films exposed to UO_2^{2+}, however, had a new reductive feature at -0.865 V vs SCE and oxidative feature at -0.03 V vs SCE (Figure 3.28). The reductive feature over multiple CVs would decrease, but the oxidative feature did not significantly decay. These new features may be due to UO_2^{2+} remaining on the surface of the electrode.

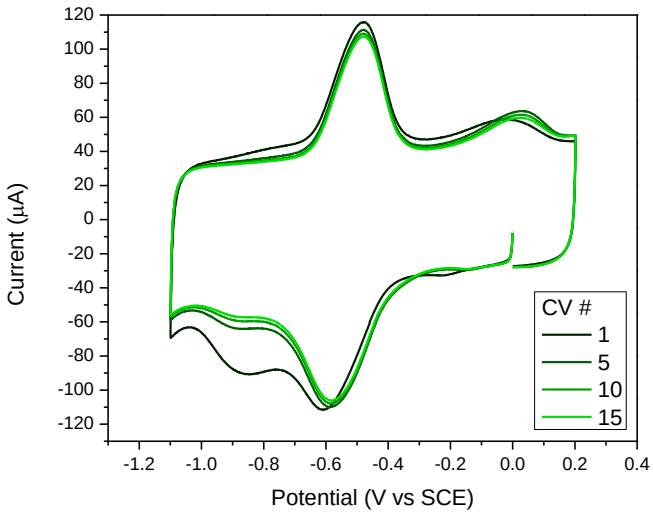

Figure 3.28: CVs of GC|CNT|^{PO}Cb-Pyr post UO_2^{2+} exposure taken in 0.1 M KCl aqueous solution.

The surface generated *nido* carborane stability when exposed to air was tested to see if the capture experiments could be performed outside the glove box. LSVs were ran in 0.1 M KCl aqueous solutions degassed with argon. No change in the oxidative LSV was observed for the GC|CNT|^{PO}Cb-Pyr film that was left in solution after the reductive LSV (Figure 3.29a). When the GC|CNT|^{PO}Cb-Pyr film was exposed to the atmosphere for 30 seconds after the reductive LSV was taken, no return oxidation feature is observed in the oxidative LSV (Figure 3.29a). CVs before and after the air exposure of this film did not show any loss in current

response (Figure 3.29b). This suggests that exposure to the atmosphere oxidizes the *nido* carborane on the surface back the *closo* carborane and is not lost or degraded.

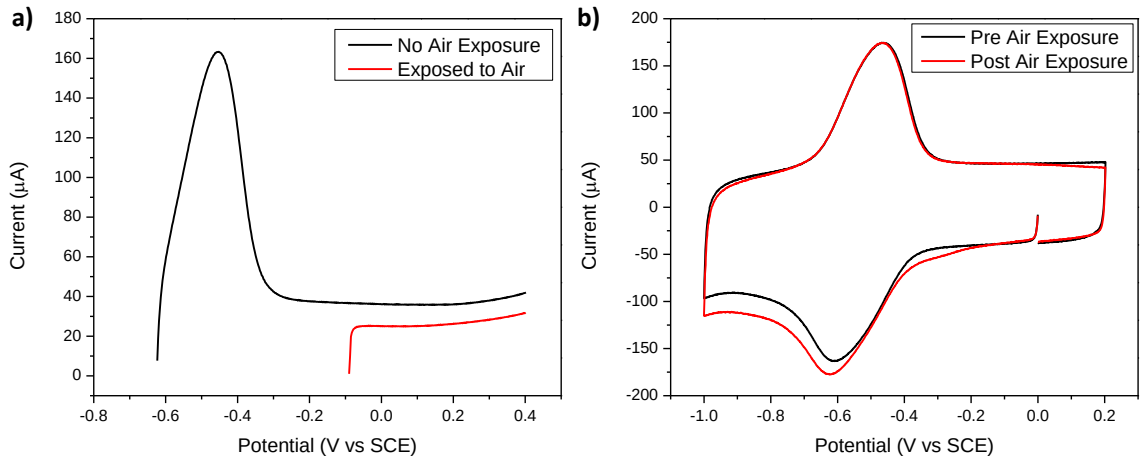

Figure 3.29: LSVs and CVs of GC|CNT|^{PO}Cb-Pyr outside the glovebox in 0.1 M KCl aqueous solutions. a) Oxidative LSVs starting at OCP of GC|^{PO}Cb after a reductive LSV with and without exposure to air. b) CVs before and after air exposure.

While the films on GC demonstrated stable electrochemical activity of **^{PO}Cb** and **^{PO}Cb-Pyr** in aqueous conditions and the use of GC|CNT permitted higher area surface loading of the **^{PO}Cb**, we needed still larger electrodes to test UO_2^{2+} capture-release where the concentration changes in UO_2^{2+} were measurable. Hence, we employed carbon fiber cloth (CF) cut to a working area of 4 cm^2. We drop casted **^{PO}Cb** or **^{PO}Cb-Pyr** in DCE onto each side of the electrode, letting it air-dry in casting (CF|^{PO}Cb, CF|^{PO}Cb-Pyr) (Figure 3.30a). CF|CNT electrodes were prepared in an analogous manner by drop casting of solutions of CNT suspended in DCE to each side of a 4 cm^2 CF electrode, letting it dry in between sides. To the CF|CNT **^{PO}Cb** or **^{PO}Cb-Pyr** in DCE was drop casted onto each side of the electrode, letting it air-dry in casting (CF|CNT|^{PO}Cb, CF|CNT|^{PO}Cb-Pyr) (Figure 3.30b).

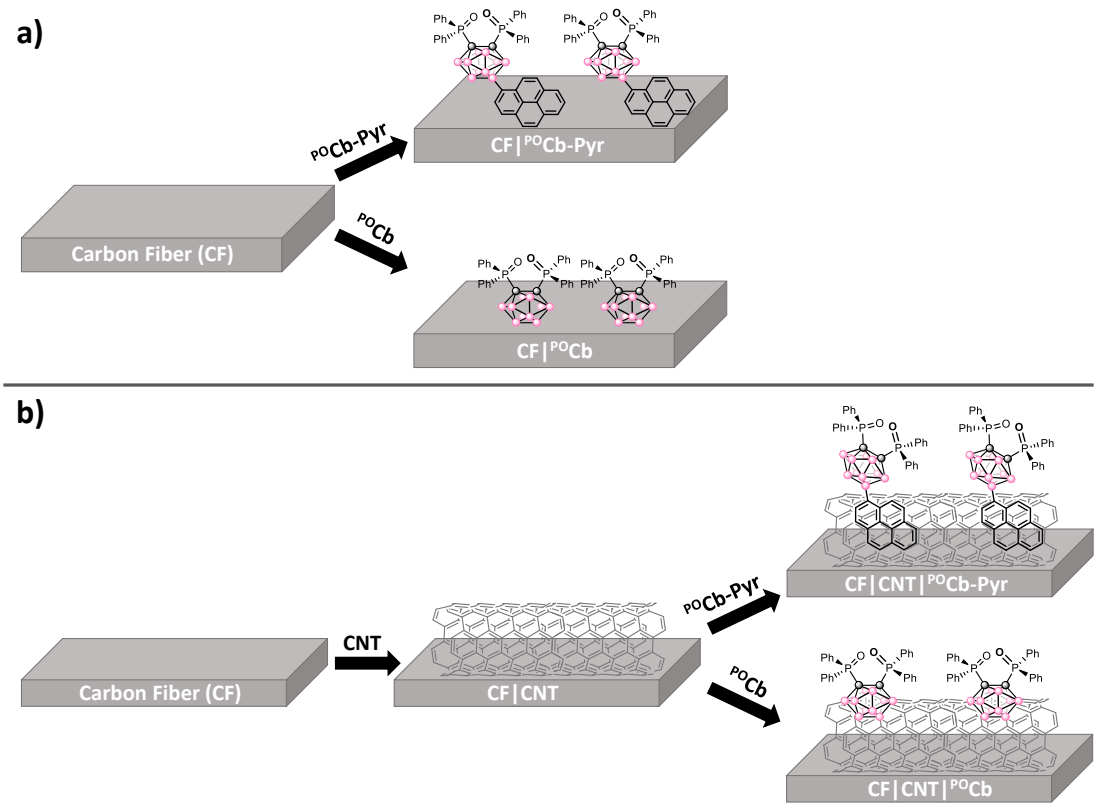

Figure 3.30: Scheme for developing various CF electrodes. a) CF|^{PO}Cb and CF|^{PO}Cb-Pyr b) CF|CNT|^{PO}Cb and CF|CNT|^{PO}Cb-Pyr

A similar trend was observed for the CF|^{PO}Cb and CF|^{PO}Cb-Pyr that observed for GC counterparts, with the CF|^{PO}Cb electrode having roughly double the current density as CF|^{PO}Cb-Pyr (Figure 3.31a-b). Unlike the GC electrodes, the films on CF did not require multiple CVs for the peaks to grow in. The CF|^{PO}Cb electrode, however, did see significant decay in current density with repeated CV scans, while the CF|^{PO}Cb-Pyr remained relatively stable. We decided to see if the addition of CNT onto CF would provide the same benefits as the GC electrodes. Akin to the GC electrodes, the addition of CNT increased the current density for CF|CNT|^{PO}Cb and CF|CNT|^{PO}Cb-Pyr (Figure 3.31c-d). The CF|CNT|^{PO}Cb still lost some current density over repeated scans but a slower rate compared to CF|^{PO}Cb. Collating

these voltammetry measurements, we found the CF|CNT electrodes offered a higher surface area due to the use of CF while the CNT enhanced electrode stability while promoting ionic contact with aqueous solutions allowing significant generation of the *nido*-carboranes on the surface.

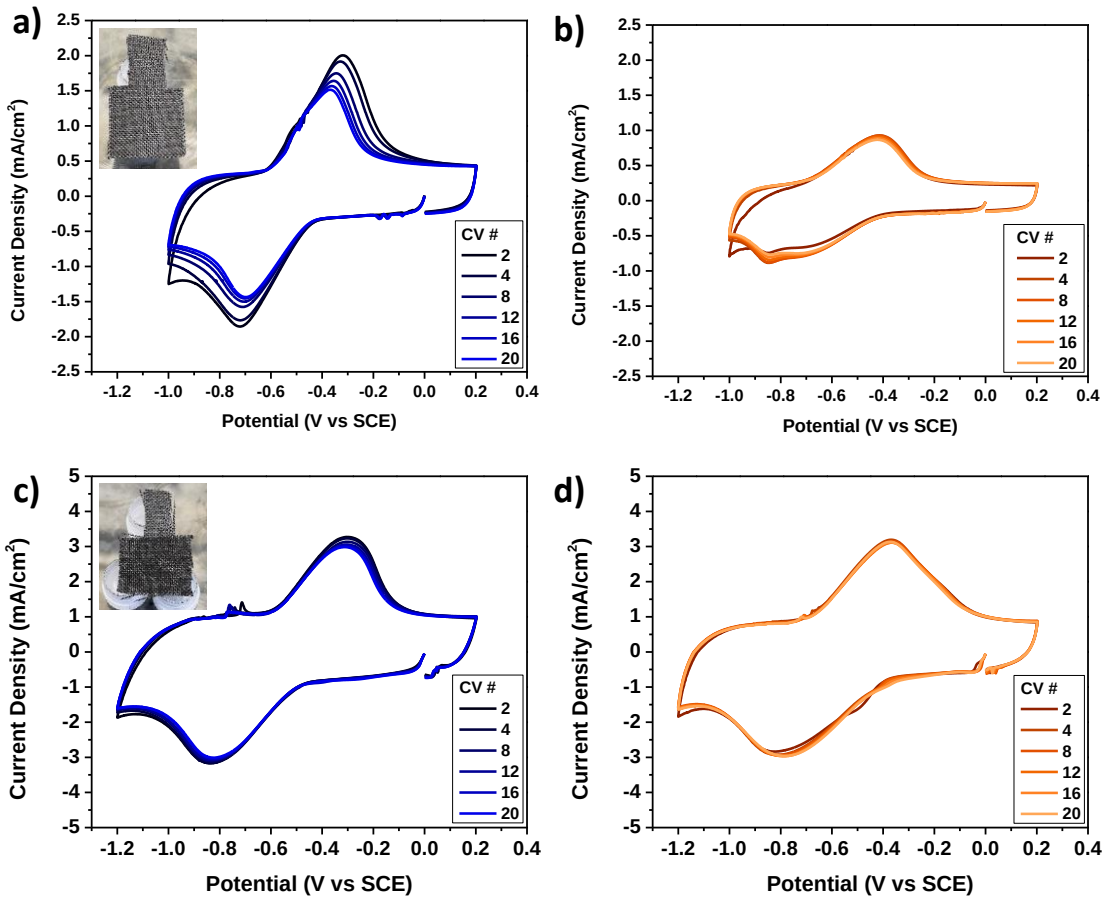

Figure 3.31: CVs of carborane films (120 nmols) on 4 cm^2 carbon fiber electrodes in 0.1 M KCl aqueous solution. a) CF|^{PO}Cb (picture insert) b) CF|^{PO}Cb-Pyr c) CF|CNT|^{PO}Cb (picture insert) d) CF|CNT|^{PO}Cb-Pyr.

3.2.5 Heterogeneous Capture

We scaled up the functionalized CF|CNT electrodes to 34 cm^2 to test their heterogeneous capture ability (Figure 3.39). These electrodes were galvanostatically reduced

in an H-cell to generate the surface bound *nido*-carborane species (Figure 3.32a). The CF|CNT charge plot rapidly decreased in potential and hit the potential cut off after only 32 seconds (Figure 3.32b), while the CF|CNT|^{PO}Cb and CF|CNT|^{PO}Cb-Pyr electrodes showed charging plateaus around the potentials observed in their CVs (Figure 3.32c-d). The charging stopped for the CF|CNT|^{PO}Cb and CF|CNT|^{PO}Cb-Pyr after the desired charge was passed to achieve an approximate 80% SOC of the *nido*-carboranes on the surface of the electrodes.

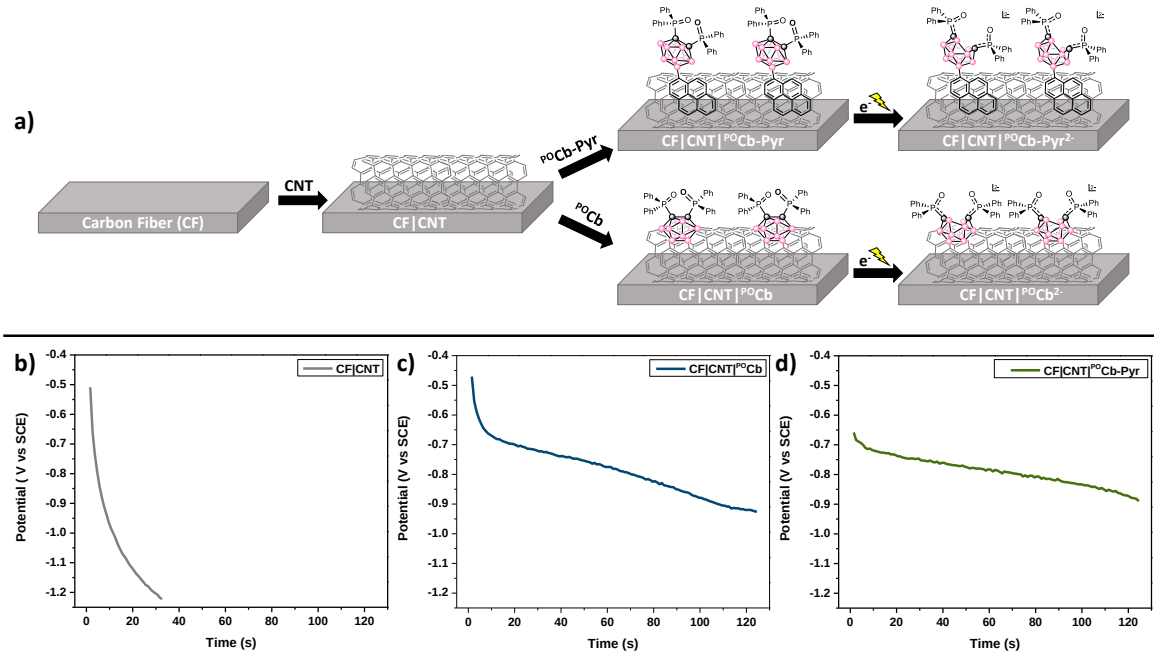

Figure 3.32: Assembly and charging of 34 cm^2 functionalized carbon fiber electrodes. a) Functionalization scheme. b) Charging plot of CF|CNT c) Charging plot of CF|CNT|^{PO}Cb d) Charging plot of CF|CNT|^{PO}Cb-Pyr

The charged electrodes were then submerged in 10 ml of a stock solution containing equimolar $CsNO_3$, $Nd(NO_3)_3(THF)_3$, $Sm(NO_3)_3(H_2O)_6$, $Th(NO_3)_4(H_2O)_x$, and $UO_2(NO_3)_2(H_2O)_6$ in 0.1 M KCl for 10 minutes (Figure 3.33). The stock solution was

subsequently drawn off the electrode and stored for analysis by ICP-OES. The electrodes were then brought outside the glove box and soaked in nitric acid overnight to oxidize the carborane and strip the captured metals into solution. CF|CNT, CF|CNT|^{PO}Cb, and CF|CNT|^{PO}Cb-Pyr electrodes not subjected to electrochemical reduction were also prepared as controls in order to deconvolute adsorption from electrochemical capture. All experiments were performed in triplicate with the stock solutions, captured solutions, and stripped (released) solutions being analysed by ICP-OES to determine metal concentrations.

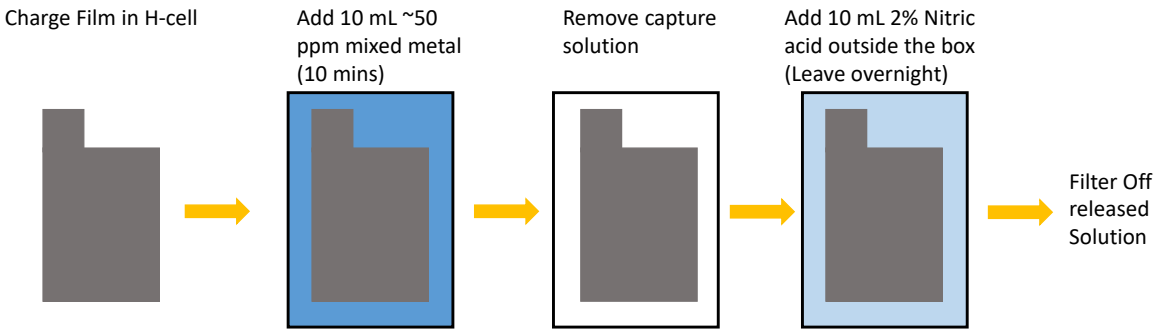

Figure 3.33: Heterogeneous capture and release steps of actinides from simulated SNF

Analysis of the CF|CNT control electrodes both with and without galvanostatic charging (grey bars and superimposed dashed bars, respectively; Figure 3.34) revealed an average percent capture for the charged electrodes of 27.8% for Th^{4+} and 12.3% for UO_2^{2+}, both significantly higher than Cs^+, Nd^{3+} and Sm^{3+} each at ~ 3.7% capture. Most importantly, these values were within error of the uncharged CF|CNT electrodes indicating that galvanostatic charging of these controls played no role in metal adsorption. In contrast, comparing the charged carborane-tethered electrodes to the uncharged ones revealed stark differences. For instance, the charged CF|CNT|^{PO}Cb electrodes captured significantly higher quantities of the actinides, Th^{4+} (52.6 %) and UO_2^{2+} (31.7%), relative to the ~5.4% capture of

Cs^{+}, Nd^{3+} and Sm^{3+} (Figure 3.34, blue bars). Most importantly, these values were all significantly higher than both the uncharged CF|CNT|^{PO}Cb control (Figure 3.34, superimposed dashed blue bars) and the CF|CNT controls. The increase in percent capture shows that the $^{PO}Cb^{2-}$ generated on the surface of the electrode preferentially captures the actinides out of aqueous solution. Lastly, the charged CF|CNT|^{PO}Cb-Pyr electrodes were next analysed. Compared to CF|CNT|^{PO}Cb, here we observed a modest increase in the percent capture for Th^{4+} (66.1%) and UO_2^{2+} (53.1%); however, this also came at the expense of modestly higher capture rates of Cs^{+}, Nd^{3+} and Sm^{3+} to ~12% each (Figure 3.34, orange bars). The slightly higher extraction values of CF|CNT|^{PO}Cb-Pyr vs. CF|CNT|^{PO}Cb electrodes is likely due to the increased stability from the additional π-π stacking, which can help prevent the loss of $^{PO}Cb\text{-}Pyr^{2-}$ from the surface. In both cases, the uncharged CF|CNT|^{PO}Cb and CF|CNT|^{PO}Cb-Pyr electrodes both showed significantly lower capture rates compared to the charged electrodes. This observation aligns with our biphasic work wherein the ^{PO}Cb does not extract UO_2^{2+} from aqueous solutions.[19, 27] In addition, we note that the CF|CNT|^{PO}Cb and CF|CNT|^{PO}Cb-Pyr capture controls (blue and orange dashed bars) are lower than in the CF|CNT controls. We attribute this to the surface-adsorbed carboranes blocking the non-specific binding sites on the surface of the CNTs. These results demonstrated that the CF|CNT preferentially binds the actinides over the alkali and lanthanides upon with the addition of $^{PO}Cb^{2-}$ and $^{PO}Cb\text{-}Pyr^{2-}$ to the surface significantly increasing the percent capture of actinides and the selectivity towards them.

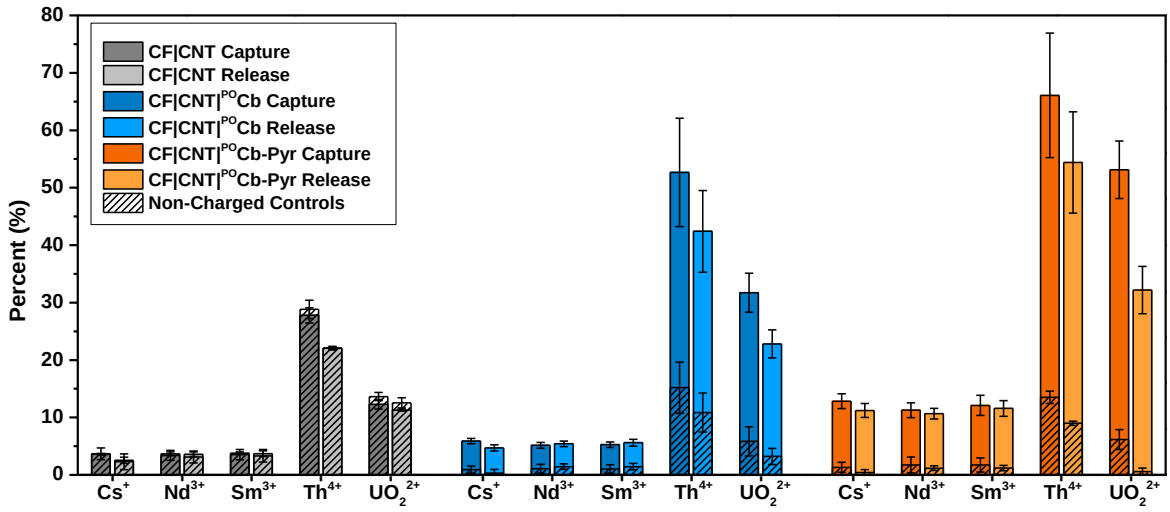

Figure 3.34: Percent heterogeneous capture and release of selected metals from mixed metal aqueous solutions (Cs^{+}, Nd^{3+}, Sm^{3+}, Th^{4+}, UO_2^{2+}) performed in triplicate with charged and non-charged CF|CNT, CF|CNT|^{PO}Cb, and CF|CNT|^{PO}Cb-Pyr electrodes.

Release of the captured metals could be easily performed by exposing the electrodes to 2% nitric acid in air, resulting in the oxidation of $^{PO}Cb^{2-}$ to ^{PO}Cb and metal release. The percent released into a fresh solution followed the same trends as capture with the charged carborane-functionalized electrodes enriching the extracted solutions with the actinides (Th^{4+} and UO_2^{2+}). The CF|CNT|^{PO}Cb electrode was able to transfer 42.4% and 22.8% of the Th^{4+} and UO_2^{2+} present in the stock solution to a fresh solution (Figure 3.34, pale blue bars). The CF|CNT|^{PO}Cb-Pyr was ~10% more efficient with 54.4% and 32.2% transferred of Th^{4+} and UO_2^{2+} respectively (Figure 3.34, pale orange bars). This protocol provides an efficient and simple method to release the metals and enrich the actinides in the final solution over the alkali and lanthanide metals in a stock.

3.3. Summary

The results herein present a simple adaptation of an electrochemically driven solution-phase metal separation process into a heterogeneous process. Drop casted films of carborane complexes maintained ionic contact with aqueous solutions with stable pseudocapacitive electrochemical behaviour. We improved the heterogeneous electrodes via the addition of CNT to carbon surfaces, attaching pyrene anchoring groups to the ligand and using carbon fiber electrodes, culminating in CF|CNT|^{PO}Cb and CF|CNT|^{PO}Cb-Pyr electrodes with high yield capture and release of actinides selectively over lanthanides and alkali metals. Tuning this system for heterogeneous capture of UO_2^{2+} from seawater with the ability to reuse electrodes is currently being investigated.

3.4. Experimental

General Considerations

All manipulations were performed under an atmosphere of dry, oxygen-free N_2 by means of standard Schlenk or glovebox techniques (MBraun, equipped with a -38 °C freezer, or VAC gloveboxes). Hexanes, pentane, dichloromethane (DCM), and benzene were dried on an MBraun solvent purification system. THF was dried over sodium benzophenone and distilled. 1,2-dichloroethane (DCE) was dried over CaH_2 for several days prior to distillation and subsequent storage on activated 4 Å molecular sieves. Dry 1,4-dioxane and chloroform-*d* were brought into the box and stored over 4 Å molecular sieves. Deionized water (Milli-Q, 18.2 MΩ.cm) was degassed by bubbling with argon overnight before transferring into a wet N_2 box. Carbon fiber sheets were purchased from the Fuelcell Store (ELAT Hydrophilic, lot # 46759-15-EH). The carbon fiber sheets were washed by dipping into acetone, hexanes, isopropyl alcohol, and DI and dried in an oven at 175 ^{o}C overnight before use. Single walled

carbon nanotubes (90%) were purchased from SkypSprings nanomaterials and used as received. [$Th(NO_3)_4$•H_2O] was purchased from Stream Chemicals. [$UO_2(NO_3)_2$•$(H_2O)_6$] was purchased from International Bio-Analytical Industries Inc. [$Sm(NO_3)_3$•$(H_2O)_6$] was purchased from Strem chemicals. $CsNO_3$ was purchased from Aldrich. 1-Bromopyrene was purchased from Ambeed. *Ortho*-carborane was purchased from Boron Specialties and sublimed before use. Ph_2PCl was purchased from Aldrich and vacuum distilled prior to use. $Nd(NO_3)_3(THF)_3$,[28] 9-Iodo-*o*-Carborane,[29] [XPhos-Pd] Catalyst,[30] and **^{PO}Cb** were prepared using literature procedures.[19]

Physical Measurements

NMR spectra were obtained on an Agilent Technologies 400 MHz spectrometer and referenced to residual solvent resonances of chloroform ($CDCl_3$) or externally (^{11}B: 85% $(Et_2O)BF_3$, ^{31}P: 85% H_3PO_4,).

Elemental analyses (C, N, H) were recorded at the University of California, Santa Barbara using an Exeter Analytical CE440 elemental analyser.

Electrochemistry experiments were carried out using a Metrohm Autolab PGSTAT128N potentiostat/galvanostat and carried out inside a wet N_2 glovebox.

Inductively Coupled Plasma-Optical Emission Spectroscopy (ICP-OES) was performed on an Agilent 5800 and used to determine the concentrations of Th, Nd, Sm, Cs, and U in aqueous solutions. Nitric acid (J.T.Baker, ICP-OES grade for trace metal analysis, ACS testing specifications, LOT 1122090) and deionized water (Milli-Q, 18.2 MΩ.cm) were used for sample preparation and dilution. A nine-point calibration curve was made by serial dilution (100-0.1 ppm) of a custom multi-element certified reference material from High Purity Standards in 2% nitric acid. The emissions lines used were Th (269.242 nm, 274.716 nm,

283.730 nm), Nd (401.224 nm, 406.108 nm, 410.945 nm, 430.357 nm), Sm (356.827 nm, 359.259 nm, 360.949 nm, 446.734 nm), Cs (495.311 nm, 672.328 nm) and U (263.553 nm, 367.007 nm, 385.957 nm). The calibrations curves for Th, Nd, Sm and U all had $R^2 > 0.9999$. An 8-point calibration curve was used for Cs with a $R^2 > 0.998$, due to an interference in the 0.1 ppm standard**.**

X-ray photoelectron spectroscopy (XPS) was taken on a ThermoFisher Escalab Xi+

Raman spectroscopy was taken on a Horiba Jobin Yvon T64000 confocal microscope using the 488 nm laser.

Synthesis

Synthesis of 1,2-$(Ph_2PO)_2$ -9-Pyrenyl-*O*-Carborane (^{PO}Cb-Pyr). The synthesis of **^{PO}Cb-Pyr** was accomplished by a three step modified literature procedures.[18, 19]

Step 1. Magnesium shavings (0.75 g), Iodine (5 mg), and 1-bromopyrene (29.6 eq., 29.6 mmol) were charged into a 100 mL Schlenk round bottom with 30 mL THF (orange solution). Under N_2, the solution was heated for 1.5 hours at 55 ^oC resulting in a deep orange solution. THF was then pumped off resulting in a brown solid. 9-Iodo-*O*-Carborane (1 eq., 9.26 mmol), XPhos-Pd-G3 (0.01 eq., 0.09 mmol), and XPhos (0.01 eq., 0.09 mmol) were added to a 500 mL Schlenk round bottom and dissolved in ~25 mL 1,4-dioxane. The Grignard pyrene was then dissolved in ~100 mL 1,4-dioxane and slowly added to the carborane solution and subsequently heated to 75 ^oC for 4 hours. The reaction was then diluted with 100 mL DCM and quenched with 100 mL H_2O. The aqueous layer was extracted with DCM (3 × 100 mL) and the combined organic layers subsequently washed with brine and dried over $MgSO_4$. The crude product was dried down and purified using a silica gel column obtaining a 28% yield (890 mg) of 9-Pyrenyl -*O*-Carborane (**1**). **^{1}H NMR** (400 MHz, $CDCl_3$) δ 8.96 (d, *J* = 9.4

Hz, 1H), 8.31 (d, *J* = 7.9 Hz, 1H), 8.16 – 8.09 (m, 2H), 8.09–8.03 (m, 2H), 8.01 (d, *J* = 2.6 Hz, 2H), 7.99–7.92 (m, 1H), 3.72 (d, *J* = 26.2 Hz, 2H). **^{11}B NMR** (128 MHz, $CDCl_3$) δ 7.81, -1.44, -8.12, -12.46 – -16.93 (m).

Step 2. A solution of *n*-BuLi in hexanes (2.5 M, 2.1 eq, 3.05 mmol) was dropwise added to a solution of **1** (1 eq., 1.45 mmol) in ~400 mL of dry diethyl ether at -78 ^{o}C resulting in a cloudy white solution. After 20 minutes, the solution was warmed to room temperature and stirred for an additional 45 minutes. The solution was cooled back down to -78 ^{o}C and Ph_2PCl (2 eq., 0.522 mL) was dropwise added to the solution. After stirring for 30 minutes, the solution was brought to room temperature and stirred for an additional hour. The solution was then dried down and dissolved in DCM before filtering over a celite. The purified product was precipitated out with the addition of pentane, yielding an orange solid with a 78.6% yield (536 mg) of 1,2-$(Ph_2P)_2$ -9-Pyrenyl -*O*-Carborane (**2**). **^{1}H NMR** (400 MHz, $CDCl_3$) δ 8.75 (d, *J* = 9.4 Hz, 1H), 8.15 (d, *J* = 7.9 Hz, 1H), 8.13–8.06 (m, 2H), 8.01–7.90 (m, 14H), 7.52–7.43 (m, 12H). **^{11}B NMR** (128 MHz, $CDCl_3$) δ 9.13, -0.26, -6.36, -10.26. **^{31}P NMR** (162 MHz, $CDCl_3$) δ 7.87 (d, *J* = 121.0 Hz), 5.41 (d, *J* = 121.0 Hz).

Step 3. A solution of **2** (1 eq., 1.14 mmols) was dissolved in 25 ml of DCM and cooled to 0^{o}C. A solution of *meta*-chloroperoxybenzoic acid (2 eq., 2.28 mmols) was dissolved in minimal DCM and was added dropwise to the solution. After stirring for 20 minutes, the solution was slowly warmed to room temperature and stirred for an additional 15 minutes. The reaction was stopped by the addition of an aqueous solution of $NaHCO_3$. The aqueous layer was extracted with DCM (3 × 25 mL) and washed with brine and dried over $MgSO_4$. The crude product was dried down and purified using a silica gel column obtaining a 69.5% yield (589 mg) of 1,2-$(Ph_2PO)_2$ -9-Pyrenyl-*O*-Carborane (**^{PO}Cb-Pyr**). **^{1}H NMR** (400 MHz,

$CDCl_3$) δ 8.53 (d, *J* = 9.4 Hz, 1H), 8.19–8.04 (m, 11H), 8.02–7.92 (m, 4H), 7.87 (d, *J* = 9.4 Hz, 1H), 7.66–7.51 (m, 12H). **^{11}B NMR** (128 MHz, $CDCl_3$) δ 11.72, 7.09 – -0.97 (m), -8.30 (d, *J* = 494.5 Hz). **^{31}P NMR** (162 MHz, $CDCl_3$) δ 24.43, 24.20. *Anal. Calcd.* $C_{42}H_{38}B_{10}P_2O_2$: C, 67.73; H, 5.14. *Found*: C, 67.28; H, 5.15.

Synthesis of [CoCp$^*_2$]$_2$[^{PO}Cb-Pyr]: A 500 ml round bottom equipped with a magnetic stir bar was charged with **^{PO}Cb-Pyr** (123.9 mg, 0.167 mmol) and ~200 ml of benzene. The solution was left to stir until the **^{PO}Cb-Pyr** was fully dissolved. In a separate vial, recrystallized $CoCp^*_2$ (109.6 mg, 0.332mmol, 2.0 equiv.) was dissolved in 20 ml of benzene and added dropwise to the stirring solution of **^{PO}Cb-Pyr**. Upon addition, an orange solid immediately precipitated from the reaction mixture, and the mixture was stirred for an additional 4 h at room temperature. After stirring was discontinued, the solids were allowed to settle to the bottom of the vial before the supernatant was filtered over a celite plug. The solids were washed with benzene (3 × 10 ml) with each wash being filtered over the celite plug. The remaining solids were then dissolved in a minimal amount of MeCN (10 ml) and filtered over the celite plug into a new vial. The volatiles were removed in vacuo, yielding a shiny golden-yellow solid **[CoCp$^*_2$]$_2$[^{PO}Cb-Pyr]**. **^{1}H NMR** (400 MHz, MeCN-d_3) δ 9.50 (d, *J* = 9.4 Hz, 1H), 8.61 (d, *J* = 7.9 Hz, 1H), 8.17 – 8.03 (m, 5H), 8.03 – 7.93 (m, 4H), 7.91 – 7.83 (m, 2H), 7.80 (d, *J* = 9.4 Hz, 1H), 7.35 – 7.19 (m, 13H), 6.33 (s, 1H), 5.55 (s, 1H), 1.54 (s, 59H). **^{11}B NMR** (128 MHz, MeCN-d_3) δ 29.93 – 11.79 (m), 7.50 (d, *J* = 115.1 Hz), 4.11 – -3.66 (m), -11.91 – -28.23 (m). **^{31}P NMR** (162 MHz, MeCN-d_3) δ 30.15, 29.64.

Electrochemistry

Cyclic voltammetry on glassy carbon rods: The ends of glassy carbon (GC) rods were sanded down and polished to a mirror finish to have a working surface area of 0.1935

cm^2. Films were made by drop casting solutions on the surface of freshly polished GC and left to dry open to air. For the pure carborane films, 10 µL of 1mM solutions of ^{PO}Cb or ^{PO}Cb-Pyr were dropped onto the freshly polished electrodes and dried open to air (GC|^{PO}Cb, GC|^{PO}Cb-Pyr). For the CNT films, 73 mg of CNT were placed in a 20 mL vial and suspended in 20 mL of DCE. This solution was then ultra-sonicated for 30 minutes in a bath sonicator. A 10 µL drop of CNT suspended in DCE (3.65 mg/mL) was placed onto the surface of a fresh GC electrode and left to dry open to air (GC|CNT). Once all the DCE evaporated, 10 µL of 1 mM ^{PO}Cb or ^{PO}Cb-Pyr in DCE was dropped onto the surface and left to dry open to air (GC|CNT|^{PO}Cb, GC|CNT|^{PO}Cb-Pyr). All electrodes were then subsequently cycled into a wet N_2 glovebox. Cyclic voltammetry (CV) was then taken in 0.1 M KCl Milli-Q solutions with a Pt counter electrode and referenced to a standard calomel electrode (SCE). Variable scan rates were taken of each film after 20 CVs at 0.1 V/s were taken.

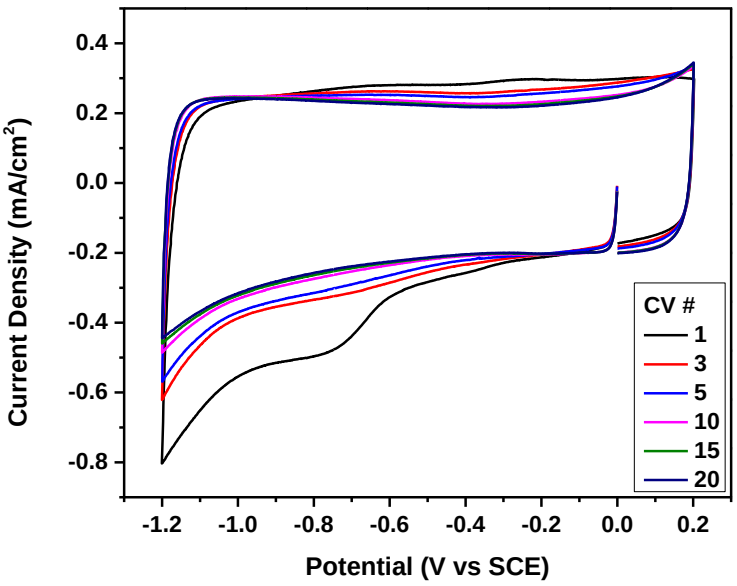

Figure 3.35: CVs of GC|CNT in 0.1 M KCl aqueous solutions at a scan rate of 0.1 V/s.

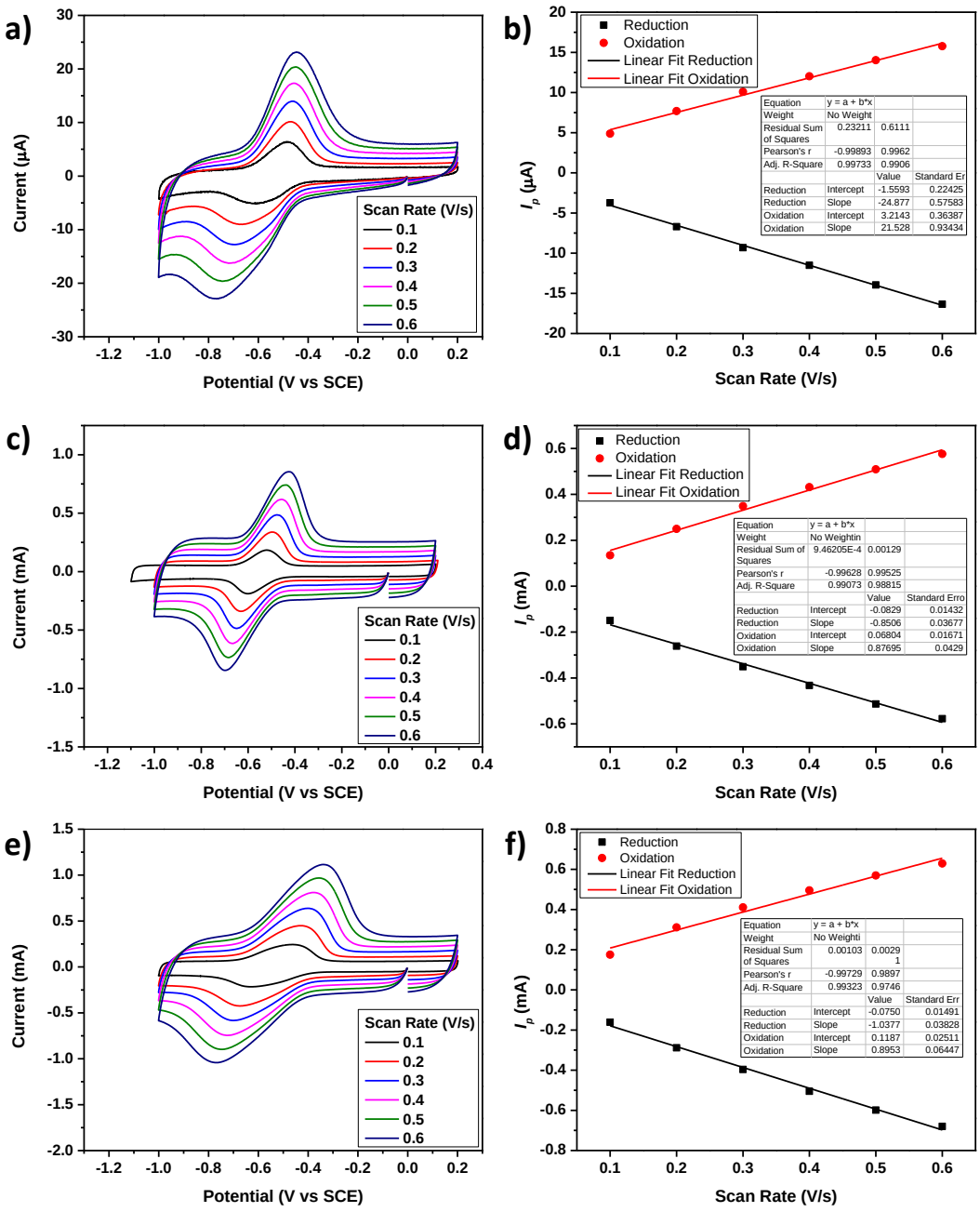

Figure 3.36: CVs of films on GC rods in 0.1 M KCl aqueous solutions at various scan rates and the peak current (I_p) vs scan rate plotted with a linear fit. a) GC|^{PO}Cb CVs b) GC|^{PO}Cb I_p vs scan rate c) GC|CNT|^{PO}Cb CVs d) GC|CNT|^{PO}Cb I_p vs scan rate d) GC|CNT|^{PO}Cb-Pyr CVs e) GC|CNT|^{PO}Cb-Pyr I_p vs scan rate.

Cyclic voltammetry on carbon fiber: Carbon Fiber (CF) was cut into 2 × 2 cm square electrodes with a 1 × 2 cm tab (Figure 3.37a) attached to a steel holder. The cut electrodes were washed with acetone, hexanes, isopropyl alcohol, DI water before being dried in an oven at 175 ^{o}C overnight. For the pure carborane functionalized CF electrodes, 120 µL of 1 mM solutions of ^{PO}Cb or ^{PO}Cb-Pyr was dispersed onto one side of the working area of the CF electrode and dried open to air after each addition. Once all of the DCE had evaporated the other side was also coated with 120 µL of 1 mM solutions of ^{PO}Cb or ^{PO}Cb-Pyr and left to dry open to air (CF|^{PO}Cb, CF|^{PO}Cb-Pyr). For the CNT functionalized CF electrodes, 73 mg of CNT were placed in 20 mL vial and suspended in 20 mL of DCE. This solution was then ultra-sonicated for 30 minutes in a bath sonicator. 200 µL of CNT suspended in DCE (3.65 mg/mL) was evenly dispersed over the CF electrode and left to dry open to air before the other side was coated (CF|CNT). Once all the DCE evaporated, 120 µL of 1 mM ^{PO}Cb or ^{PO}Cb-Pyr in DCE was dispersed onto the surface and left to dry open to air before the other side was coated (GC|CNT|^{PO}Cb, GC|CNT|^{PO}Cb-Pyr) (Figure 3.37b). The electrodes were attached to a steel holder (Figure 3.37c) before being cycled into a wet N_2 glovebox. Cyclic voltammetry (CV) was performed in 0.1 M KCl Milli-Q solutions with a Pt counter electrode and referenced to a standard calomel electrode (SCE).

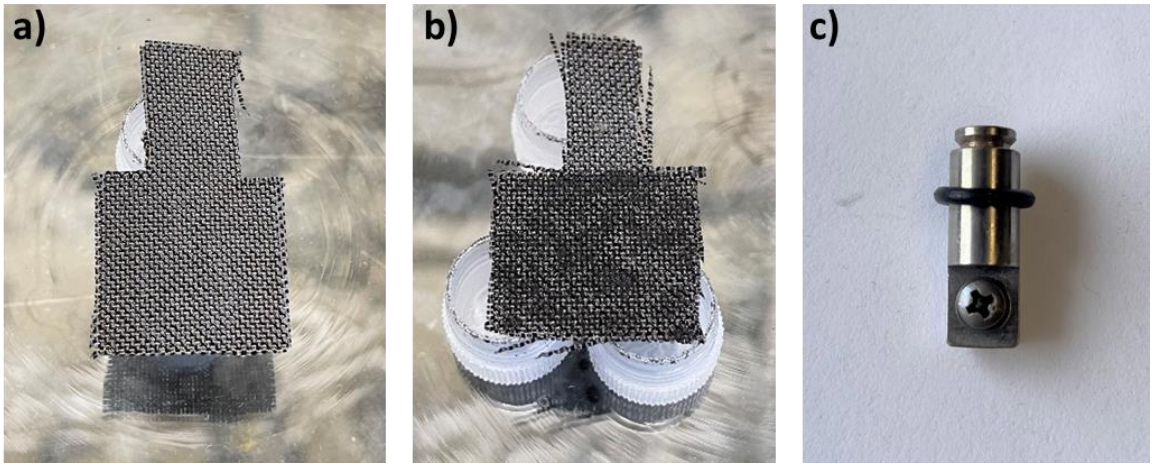

Figure 3.37 a) non-functionalized CF electrode. b) CF electrode functionalized with CNT and ^{PO}Cb (CF|CNT|^{PO}Cb). c) Steel electrode holder.

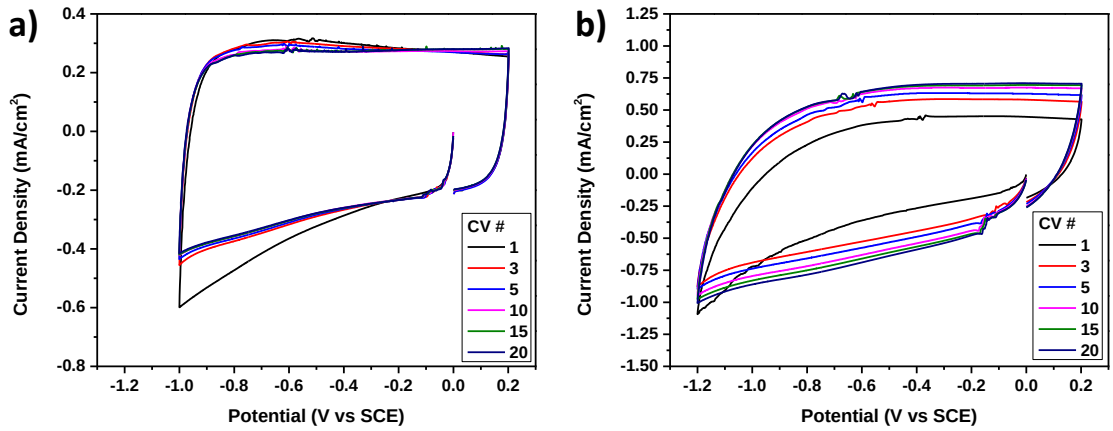

Figure 3.38: a) CVs of CF electrode. b) CVs of CF|CNT.

Heterogeneous Capture-Release

Mixed Metal Stock Solution: Individual stock solutions of $CsNO_3$, $Nd(NO_3)_3(THF)_3$, $Sm(NO_3)_3(H_2O)_6$, $Th(NO_3)_4(H_2O)_x$, and $UO_2(NO_3)_2(H_2O)_6$ were made up to be roughly 2 mM in a 0.1M KCl Milli-Q solution. ICP-OES was used to determine the accurate concentrations of individual stocks. Roughly 100 mL aliquots of each stock solution were added to 1 L volumetric flask and diluted to the 1 L mark with 0.1 M KCl Milli-Q solutions to achieve a

final concentration of ~0.2 mM for each metal. The mixed metal stock solution concentration was determined by ICP-OES (Cs 0.2156 mM, Nd 0.1848 mM, Sm 0.1891 mM, Th 0.187 mM, U 0.1926 mM)

Electrode Preparation: CF was cut into 8.5 × 4 cm (34 cm^2) electrodes with a 1.5 × 1.5 cm tab. The cut electrodes were washed with acetone, hexanes, isopropyl alcohol, DI and dried in an oven at 175 ^oC overnight before being functionalized. CNT (73 mg) were placed in 20 mL vial and suspended in 20 mL of DCE. The solution was then ultra-sonicated for 30 minutes in a bath sonicator. 1.7 mL of this CNT suspended in DCE solution (3.65 mg/mL) was evenly dispersed onto each side of a 34 cm^2 carbon fiber cloth and left to dry in open air before coating the second side. Once dried, 1 mL of 2 mM solutions of carborane (^{PO}Cb or ^{PO}Cb-Pyr) was dispersed on each side and left to dry between sides (Figure 3.39). Once dried these electrodes were cycled into a wet N_2 glovebox.

Figure 3.39: Example of a 34 cm^2 CF|CNT|^{PO}Cb electrode

Charging Electrodes: An H-cell (Figure 3.40) separated by a glass frit was filled with ~60 mL 0.1 M KCl on each side and a washed 20 × 20 cm sheet of CF attached to a steel holder was placed in the counter electrode compartment of the H-cell. An SCE electrode was placed in a separate compartment attached to the working electrode compartment with a Luggin capillary to measure the potential at the working electrode. The functionalized electrodes (CF|CNT, CF|CNT|^{PO}Cb, and CF|CNT|^{PO}Cb-Pyr) were attached to steel holders and submerged in the working electrode compartment. A -5 mA current was applied between the counter electrode and the working functionalized electrode for 124 seconds to reach an 80% state of charge or hit a potential cut-off of -1.2 V vs SCE (Figure 3.32b-d). Once charging was complete, the electrode was removed from the H-cell and allowed to drip dry before being placed into a 20 mL vial.

Figure 3.40: Glass frit separated H-Cell

Capture Experiment: The 20 mL vial containing the charged electrode was tared before ~10 ml of the mixed solution was poured into the vial. The weight of the mixed metal solution dispensed was recorded. The solution was then swirled to ensure the electrode came into full contact with the solution and was left to sit in the solution for 10 minutes. The solution was then drawn off and put into a separate vial. The vial containing the electrode was weighed again to measure and record the residual mixed metal solution trapped in the electrode. The captured solutions were brought outside the glove box and filtered with a 0.22 μm PVDF syringe filter to remove particulates before being diluted with nitric acid to achieve a 2% nitric acid solution for ICP-OES analysis.

Release Experiment: Outside the box, the electrodes in 20 mL vials were tared before ~10 mL of 2% nitric acid was put into the vials. The amount of nitric acid transferred was recorded. The solution was shaken with the electrode and allowed to sit in the nitric acid overnight. The solution was then drawn off and filtered with a 0.22 μm PVDF syringe filter into a pre-leached flacon tube for ICP-OES analysis.

Non-charged Control Experiments: Non-Charged functionalized electrodes (CF|CNT, CF|CNT|^{PO}Cb, and CF|CNT|^{PO}Cb-Pyr) went through the same process for capture and release with the only difference being no current being passed through the electrode.

3.5. References

(1) Glatz, J.-P. 6.11 - Spent Fuel Dissolution and Reprocessing Processes. In *Comprehensive Nuclear Materials (Second Edition)*, Konings, R. J. M., Stoller, R. E. Eds.; Elsevier, 2020; pp 305-326.

(2) Kumari, I.; Kumar, B. V. R.; Khanna, A. A review on UREX processes for nuclear spent fuel reprocessing. *Nucl. Eng. Des.* **2020**, *358*, 110410. DOI: https://doi.org/10.1016/j.nucengdes.2019.110410.

(3) Abney, C. W.; Mayes, R. T.; Saito, T.; Dai, S. Materials for the Recovery of Uranium from Seawater. *Chem. Rev.* **2017**, *117* (23), 13935-14013. DOI: 10.1021/acs.chemrev.7b00355.

(4) Feng, M.-L.; Sarma, D.; Qi, X.-H.; Du, K.-Z.; Huang, X.-Y.; Kanatzidis, M. G. Efficient Removal and Recovery of Uranium by a Layered Organic–Inorganic Hybrid Thiostannate. *J. Am. Chem. Soc.* **2016**, *138* (38), 12578-12585. DOI: 10.1021/jacs.6b07351.

(5) Song, Y.; Zhu, C.; Sun, Q.; Aguila, B.; Abney, C. W.; Wojtas, L.; Ma, S. Nanospace Decoration with Uranyl-Specific “Hooks” for Selective Uranium Extraction from Seawater with Ultrahigh Enrichment Index. *ACS Cent. Sci.* **2021**, *7* (10), 1650-1656. DOI: 10.1021/acscentsci.1c00906.

(6) Wang, Z.; Ma, R.; Meng, Q.; Yang, Y.; Ma, X.; Ruan, X.; Yuan, Y.; Zhu, G. Constructing Uranyl-Specific Nanofluidic Channels for Unipolar Ionic Transport to Realize Ultrafast Uranium Extraction. *J. Am. Chem. Soc.* **2021**, *143* (36), 14523-14529. DOI: 10.1021/jacs.1c02592.

(7) Yuan, Y.; Meng, Q.; Faheem, M.; Yang, Y.; Li, Z.; Wang, Z.; Deng, D.; Sun, F.; He, H.; Huang, Y.; et al. A Molecular Coordination Template Strategy for Designing Selective Porous Aromatic Framework Materials for Uranyl Capture. *ACS Cent. Sci.* **2019**, *5* (8), 1432-1439. DOI: 10.1021/acscentsci.9b00494.

(8) Chi, F.; Zhang, S.; Wen, J.; Xiong, J.; Hu, S. Highly Efficient Recovery of Uranium from Seawater Using an Electrochemical Approach. *Ind. Eng. Chem. Res.* **2018**, *57* (23), 8078-8084. DOI: 10.1021/acs.iecr.8b01063.

(9) Liu, C.; Hsu, P.-C.; Xie, J.; Zhao, J.; Wu, T.; Wang, H.; Liu, W.; Zhang, J.; Chu, S.; Cui, Y. A half-wave rectified alternating current electrochemical method for uranium extraction from seawater. *Nat. Energy* **2017**, *2* (4), 17007. DOI: 10.1038/nenergy.2017.7.

(10) Ge, A.; Rudshteyn, B.; Videla, P. E.; Miller, C. J.; Kubiak, C. P.; Batista, V. S.; Lian, T. Heterogenized Molecular Catalysts: Vibrational Sum-Frequency Spectroscopic, Electrochemical, and Theoretical Investigations. *Acc. Chem. Res.* **2019**, *52* (5), 1289-1300. DOI: 10.1021/acs.accounts.9b00001.

(11) Sun, L.; Reddu, V.; Fisher, A. C.; Wang, X. Electrocatalytic reduction of carbon dioxide: opportunities with heterogeneous molecular catalysts. *Energy Environ. Sci.* **2020**, *13* (2), 374-403, 10.1039/C9EE03660A. DOI: 10.1039/C9EE03660A.

(12) Lei, H.; Liu, C.; Wang, Z.; Zhang, Z.; Zhang, M.; Chang, X.; Zhang, W.; Cao, R. Noncovalent Immobilization of a Pyrene-Modified Cobalt Corrole on Carbon Supports for Enhanced Electrocatalytic Oxygen Reduction and Oxygen Evolution in Aqueous Solutions. *ACS Catal.* **2016**, *6* (10), 6429-6437. DOI: 10.1021/acscatal.6b01579.

(13) Maurin, A.; Robert, M. Noncovalent Immobilization of a Molecular Iron-Based Electrocatalyst on Carbon Electrodes for Selective, Efficient CO2-to-CO Conversion in Water. *J. Am. Chem. Soc.* **2016**, *138* (8), 2492-2495. DOI: 10.1021/jacs.5b12652.

(14) Blakemore, J. D.; Gupta, A.; Warren, J. J.; Brunschwig, B. S.; Gray, H. B. Noncovalent Immobilization of Electrocatalysts on Carbon Electrodes for Fuel Production. *J. Am. Chem. Soc.* **2013**, *135* (49), 18288-18291. DOI: 10.1021/ja4099609.

(15) Chen, T.; Li, M.; Liu, J. π–π Stacking Interaction: A Nondestructive and Facile Means in Material Engineering for Bioapplications. *Cryst. Growth Des.* **2018**, *18* (5), 2765-2783. DOI: 10.1021/acs.cgd.7b01503.

(16) Sinnokrot, M. O.; Valeev, E. F.; Sherrill, C. D. Estimates of the Ab Initio Limit for π–π Interactions: The Benzene Dimer. *J. Am. Chem. Soc.* **2002**, *124* (36), 10887-10893. DOI: 10.1021/ja025896h.

(17) Hanna, C. M.; Sanborn, C. D.; Ardo, S.; Yang, J. Y. Interfacial Electron Transfer of Ferrocene Immobilized onto Indium Tin Oxide through Covalent and Noncovalent Interactions. *ACS Appl. Mater. Interfaces.* **2018**, *10* (15), 13211-13217. DOI: 10.1021/acsami.8b01219.

(18) Anderson, K. P.; Mills, H. A.; Mao, C.; Kirlikovali, K. O.; Axtell, J. C.; Rheingold, A. L.; Spokoyny, A. M. Improved synthesis of icosahedral carboranes containing exopolyhedral BC and CC bonds. *Tetrahedron* **2019**, *75* (2), 187-191. DOI: https://doi.org/10.1016/j.tet.2018.11.040.

(19) Keener, M.; Hunt, C.; Carroll, T. G.; Kampel, V.; Dobrovetsky, R.; Hayton, T. W.; Ménard, G. Redox-switchable carboranes for uranium capture and release. *Nature* **2020**, *577* (7792), 652-655. DOI: 10.1038/s41586-019-1926-4.

(20) Leites, L. A. Vibrational spectroscopy of carboranes and parent boranes and its capabilities in carborane chemistry. *Chem. Rev.* **1992**, *92* (2), 279-323. DOI: 10.1021/cr00010a006.

(21) Pujari, S. P.; Scheres, L.; van Lagen, B.; Zuilhof, H. Organic Monolayers from 1-Alkynes Covalently Attached to Chromium Nitride: Alkyl and Fluoroalkyl Termination. *Langmuir* **2013**, *29* (33), 10393-10404. DOI: 10.1021/la401978h.

(22) Chang, D.; Malinski, T.; Ulman, A.; Kadish, K. M. Electrochemistry of nickel(II) porphyrins and chlorins. *Inorg. Chem.* **1984**, *23* (7), 817-824. DOI: 10.1021/ic00175a006.

(23) Bregadze, V. I. Dicarba-closo-dodecaboranes C2B10H12 and their derivatives. *Chem. Rev.* **1992**, *92* (2), 209-223. DOI: 10.1021/cr00010a002.

(24) Fujii, S. Expanding the chemical space of hydrophobic pharmacophores: the role of hydrophobic substructures in the development of novel transcription modulators. *MedChemComm* **2016**, *7* (6), 1082-1092, 10.1039/C6MD00012F. DOI: 10.1039/C6MD00012F.

(25) Asawa, Y.; Nishida, K.; Kawai, K.; Domae, K.; Ban, H. S.; Kitazaki, A.; Asami, H.; Kohno, J.-Y.; Okada, S.; Tokuma, H.; et al. Carborane as an Alternative Efficient Hydrophobic Tag for Protein Degradation. *Bioconjug. Chem.* **2021**, *32* (11), 2377-2385. DOI: 10.1021/acs.bioconjchem.1c00431.

(26) Corbin, N.; Zeng, J.; Williams, K.; Manthiram, K. Heterogeneous molecular catalysts for electrocatalytic CO2 reduction. *Nano Res.* **2019**, *12* (9), 2093-2125. DOI: 10.1007/s12274-019-2403-y.

(27) Keener, M.; Mattejat, M.; Zheng, S.-L.; Wu, G.; Hayton, T. W.; Ménard, G. Selective electrochemical capture and release of uranyl from aqueous alkali, lanthanide, and actinide

mixtures using redox-switchable carboranes. *Chem. Sci.* **2022**, *13* (12), 3369-3374, 10.1039/D1SC07070C. DOI: 10.1039/D1SC07070C.

(28) Evans, W. J.; Giarikos, D. G.; Workman, P. S.; Ziller, J. W. Utility of Anhydrous Neodymium Nitrate as a Precursor to Extended Organoneodymium Nitrate Networks. *Inorg. Chem.* **2004**, *43* (18), 5754-5760. DOI: 10.1021/ic049187b.

(29) Andrews, J. S.; Zayas, J.; Jones, M. 9-Iodo-o-carborane. *Inorg. Chem.* **1985**, *24* (22), 3715-3716. DOI: 10.1021/ic00216a053.

(30) Bruno, N. C.; Tudge, M. T.; Buchwald, S. L. Design and preparation of new palladium precatalysts for C–C and C–N cross-coupling reactions. *Chem. Sci.* **2013**, *4* (3), 916-920, 10.1039/C2SC20903A. DOI: 10.1039/C2SC20903A.

Chapter 4 Commercial Metal Phthalocyanine Charge Carriers

4.1. Introduction

The near exponential deployment of renewable energy (RE) technologies worldwide has resulted in rapidly decreasing RE capital costs while providing an increasingly decarbonized energy grid. While RE production has increased, so has curtailment in many leading jurisdictions (e.g., California, Germany, etc.)[1], driven in part by a shortage of energy storage systems (ESS). Redox flow batteries (RFBs) are attractive grid-scale ESS due to their long lifetimes, scalability, and decoupled energy and power density. RFBs store energy in separate external "catholyte" and "anolyte" electrolyte tanks containing soluble molecular redox couples, termed charge-carriers. These charge-carrier solutions can be flowed to membrane-separated electrodes where charge-discharge occurs.[2-4] The energy capacity of these systems is governed by the tank sizes and the charge-carrier concentrations. The flow rate and electrode and membrane surface area control the power density.[4]

There remain significant economic and chemical barriers to expanding small-scale RFB installations into wide scale deployment. Most V-based RFBs have an estimated minimum cost of $400/kWh which is well above the U.S. Department of Energy's $100/kWh target for wide-scale ESS deployment.[5] The raw material cost of vanadium charge carriers contribute ~$300/kWh to the total cost of the system, indicating charge-carrier cost reduction is of vital importance.[6] RFB deployment is also limited by chemical factors such as membrane crossover capacity fade and low charge carrier solubility.[7] The use of symmetric charge carriers – i.e., different redox states of the same molecule in both the catholyte and anolyte solutions – decreases associated membrane costs by allowing for the use of inexpensive physical separators[6, 8] and minimizes deleterious membrane crossover of mixed charge carrier species. One limit on symmetric charge-carriers has been the perceived need for high

solubility. With the emergence of semisolid RFBs and slurry-based electrochemical flow capacitors (EFCs) capable of high energy densities, it is clear that these solubility limits can be overcome. This development allows the expansion of potential charge-carriers to include previously ignored classes of compounds with poor solubility, such as phthalocyanine metal complexes (PcM).[9-12]

Our group, spearheaded by Camden Hunt, synthesized and characterized 1,4,8,11,15,18,22,25-octaethoxyphthalocyanine manganese nitride (^{OEt}PcMnN) (Figure 4.1a) as a potential symmetric charge carrier.[13] While unsubstituted PcM complexes generally are insoluble in most solvents, the addition of eight ethoxy groups to the phthalocyanine ring enabled ^{OEt}PcMnN to be sparingly soluble in organic solvents. We found that ^{OEt}PcMnN was able to reversibly undergo two subsequent reductions as well as two subsequent oxidations (Figure 4.1b). No signs of degradation were observed for these redox features even after 500 consecutive CVs were ran on the solution, preliminarily showing their stability.[14] Having multiple stable oxidation states with large potential differences between them made ^{OEt}PcMnN an excellent candidate as a symmetric charge carrier.

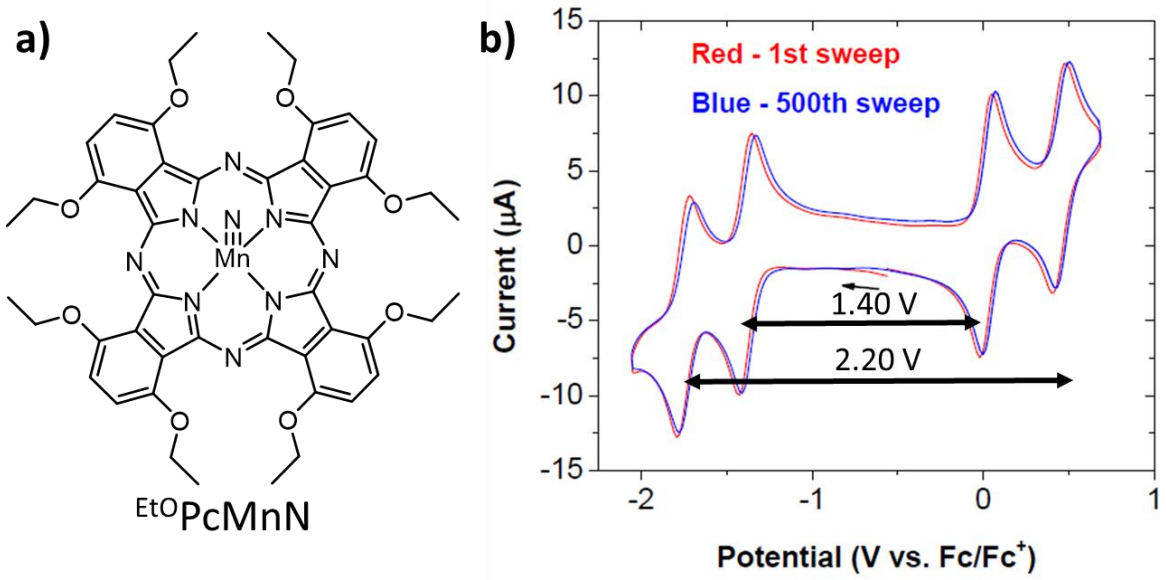

Figure 4.1: Structure and repeated CVs of ^{OEt}PcMnN (0.24 mM) at 0.5 V/s in DCM $[Bu_4N][PF_6]$ (0.1M) using a 3 mm glassy carbon working electrode. a)^{OEt}PcMnN structure. b) 1st and 500th CVs of ^{OEt}PcMnN.

The ability of ^{OEt}PcMnN to serve as a symmetric charge carrier was tested by galvanostatically cycling in an H-cell with ^{OEt}PcMnN on each side. A 100 µA charging current and a −12.5 µA discharging current were applied to the cell and cycled between a 75% and 0% state of charge (SOC) for 35 cycles. The charge-discharge curves had two distinct plateaus during cycling corresponding to the generation of ^{OEt}PcMnN^{1-}/ ^{OEt}PcMnN^{1+} and ^{OEt}PcMnN^{2-}/ ^{OEt}PcMnN^{2+} in solution (Figure 4.2a). The FE remained relatively stable while cycling, but the VE did decrease over time due to cell polarization (Figure 4.2b). The downside to this solution state cycling was the low solubility of ^{OEt}PcMnN, which led to a low energy density of 0.02 Wh/L.

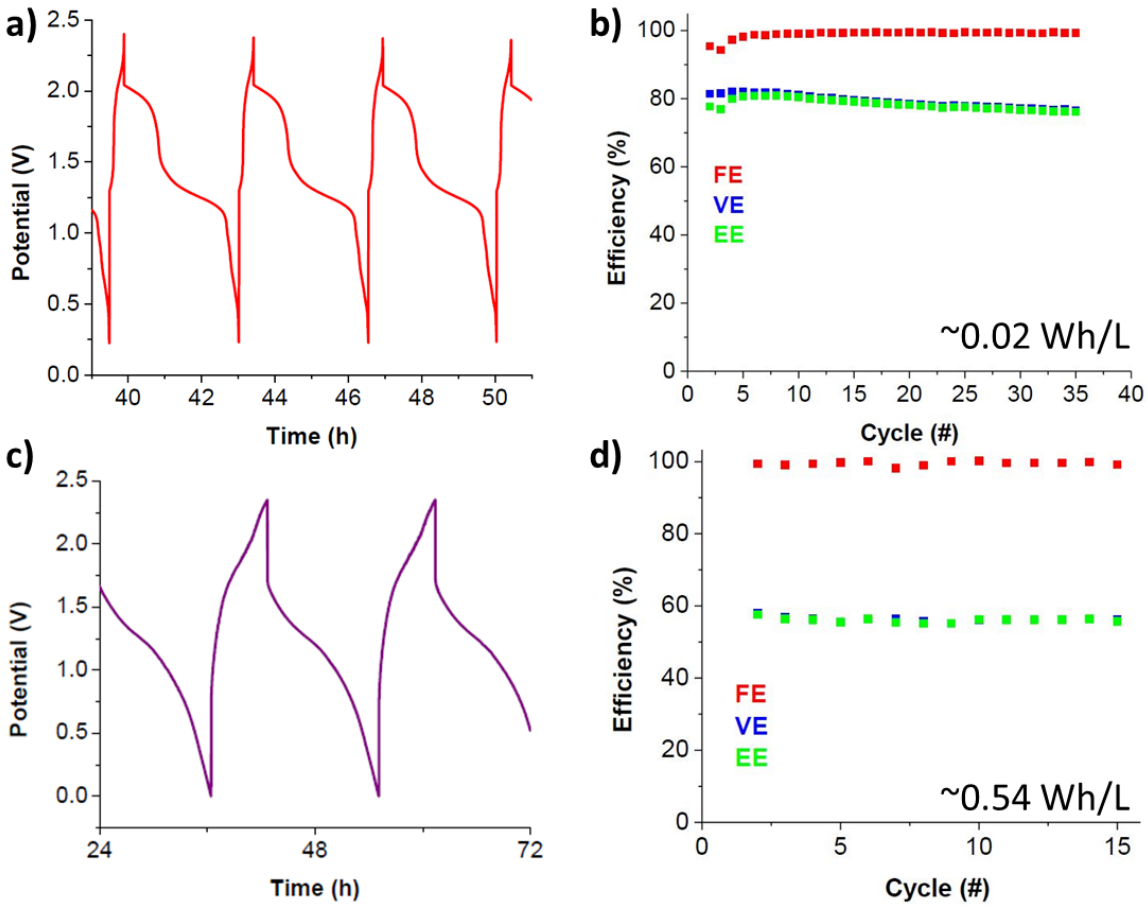

Figure 4.2: Cycling data of ^{OEt}PcMnN and ^{OEt}PcMnN/KB a) ^{OEt}PcMnN solution state galvanostatic charge-discharge curves. b) Faradaic efficiency (FE), voltage efficiency (VE), and energy efficiency (EE) for solution state cycling. c) ^{OEt}PcMnN/KB slurry state galvanostatic charge-discharge curves. d) FE, VE, and EE for slurry state cycling.

A percolation network setup by the addition of a Ketjenblack (KB) slurry was used to increase the energy density of the system. This system pushed past the solubility limit of ^{OEt}PcMnN in MeCN and utilized the KB percolation network to charge the undissolved ^{OEt}PcMnN. The charge-discharge curves for this system blended the linear response of a capacitor contributed from the KB with the plateaus observed in the solution state cycling

(Figure 4.2a). This allowed for the systems energy density to be increase ~27 times to 0.54 Wh/L, while retaining >99% capacity retention (Figure 4.2d).

In a follow-up report, we explored the electrochemical properties of the expanded first-row series (^{OEt}PcM; M = VO, Cr, MnCl, Fe, Co, Ni, Cu, Zn) and determined that many of these displayed favorable properties for use as charge carriers.[15] All ^{OEt}PcM had multiple accessible redox states, with varying properties based on axial substitution of the metal. Non-labile axial coordination generally led to cleaner more reversible CVs, while non-axial substitution led to electrochemical absorption events. We were curious if these differences in properties would have an effect on their ability to serve as charge carriers.

In this chapter, we expand our scope to investigate the charge-carrier properties of inexpensive, commercially available, peripherally unsubstituted PcM complexes (Figure 4.3). Peripherally unsubstituted PcM are known to be chemically robust and to display rich electrochemical properties, but have poor solubility in common organic solvents.[16, 17] In 2020, PcMs were produced on the megaton scale with a cumulative $1.5 billion US market value for the dye and pigment industry.[18] "Phthalo Blue" (PcCu) is the most widely produced and costs around $4.48/kg.[19] The use of such inexpensive materials could significantly drive down charge carrier costs and address one of the main hurdles to RFB development.

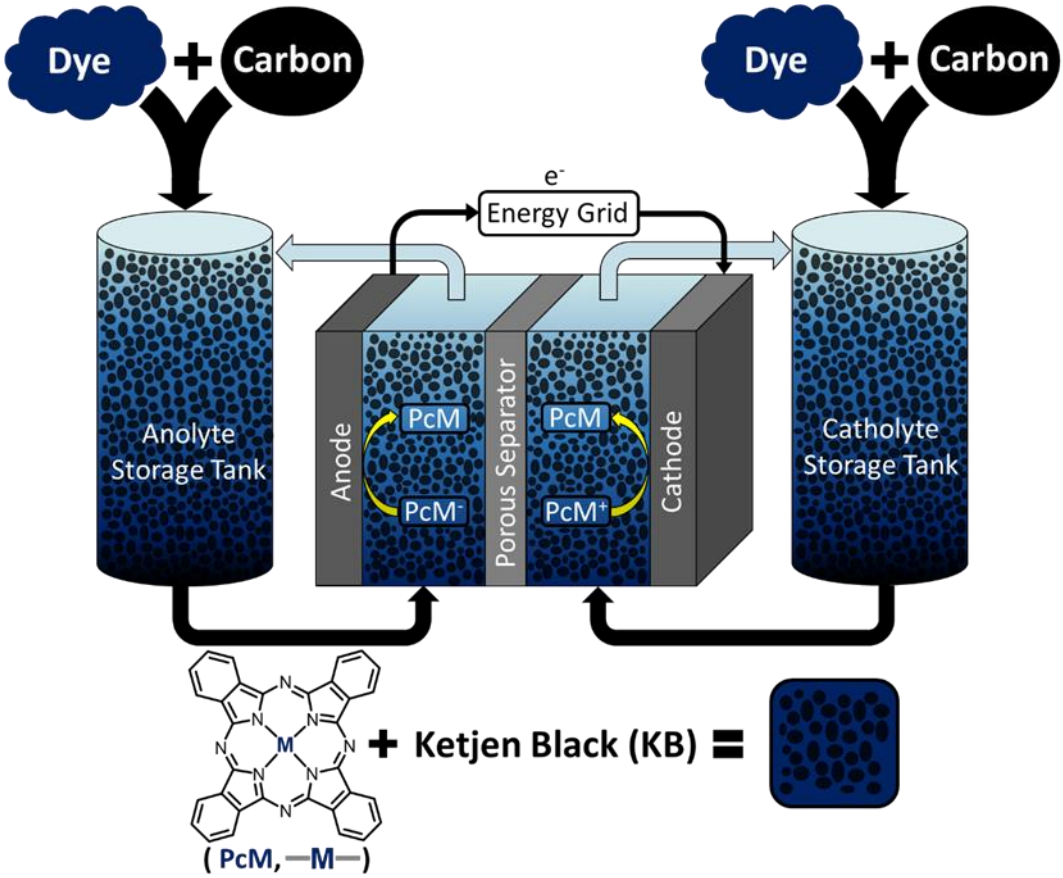

Figure 4.3: Diagram of a symmetric slurry-based hybrid RFB/EFC using PcM dyes as charge carriers and a capacitive, conductive carbon material, KB

4.2. Results and Discussion

4.2.1. KetjenBlack Electrochemistry

KB is a type of electro-conductive carbon that is manufactured by the incomplete combustion of oil products. It is used as an antistatic and electroconductive agent in a variety of materials. KB can impart conductivity into materials at low loading amounts due to its high surface area and particle size. We used KB in the slurry system to serve as a percolation network as well as a capacitive component of storage.

We galvanostatically cycled a 50 mg slurry of KB in 0.2 M $[Bu_4N][PF_6]$ MeCN solution with charge and discharge currents of 500 µA and -250 µA and a potential cut-off 2.5 V. The resulting charge-discharged curves had a linear relationship with the amount of charged passed, which aligns with the expected response of a capacitor (Figure 4.4a). The FE of the system was high at 99%, but the VE was low at only 57% (Figure 4.4b). The energy density of the system was also low around 0.06 Wh/L and under these conditions the KB was able to store 25 C/g.

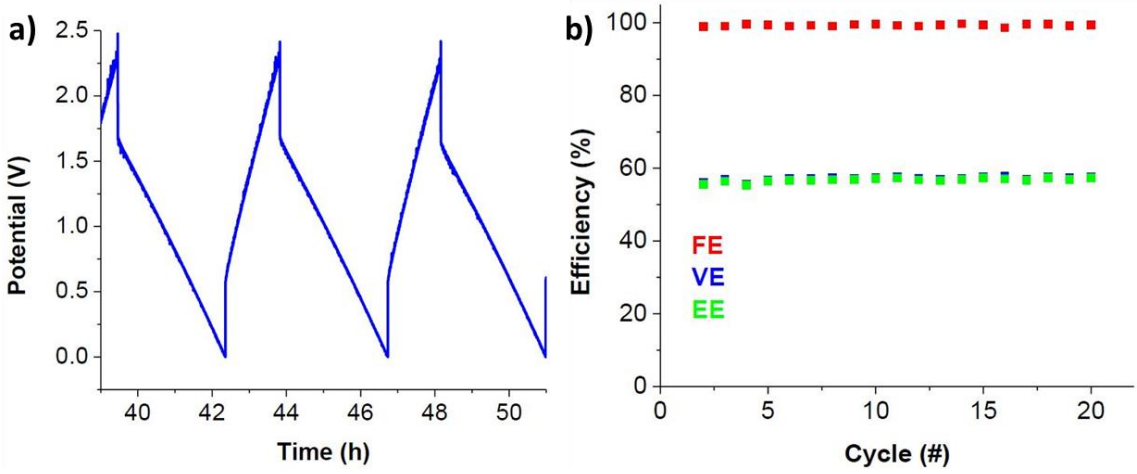

Figure 4.4: Cycling data of KB slurry a) KB slurry galvanostatic charge-discharge curves. b) FE, VE, and EE of KB slurry cycles.

The self-discharge rate for the systems was tested to ensure the cells were capable of storing charge. Cells of ^{OEt}PcMnN/KB and KB slurries were charged to a 75% SOC and left in the charged state overnight. Periodically the open circuit potential (OCP) of the cell was measured to see if the charge was maintained (Figure 4.5). Both slurries observed a slight loss in the OCP for the first two hours but held steady for the rest of the 24-hour period. The ^{OEt}PcMnN/KB slurry maintained a higher OCP compared to the pure KB slurry.

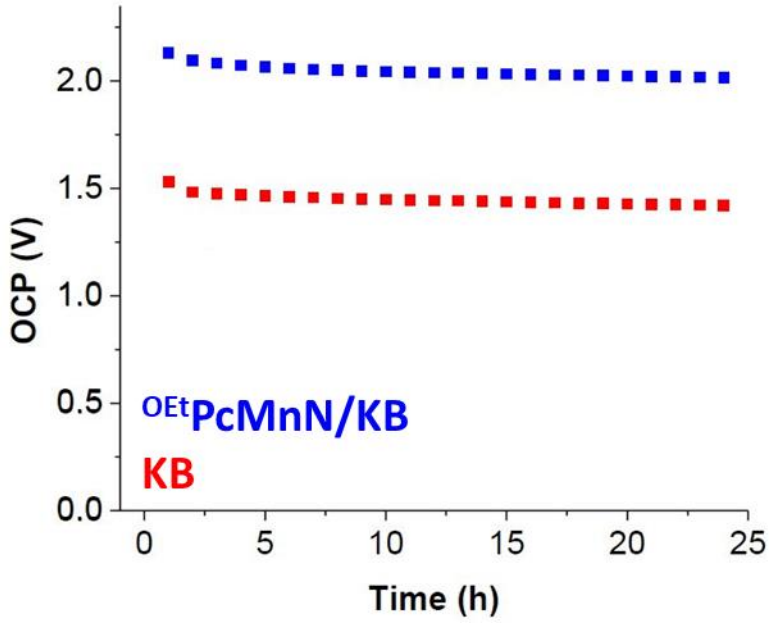

Figure 4.5: Self discharge experiment on ^{OEt}PcMnN/KB and KB

To characterize the formation of an electronically conductive percolation networks in suspensions, we semi-quantitatively measured the DC resistivity of KB slurries between two Pt loops immersed in KB suspensions. We found this DC resistance decreased by a factor of 4000 going from a 0.5%(w/w) to a 1.0%(w/w) KB suspension, with further KB addition leading to negligible changes in DC resistance (Figure 4.6).[20] This indicates at 1.0%(w/w) the KB slurry is forming an electronically conductive percolation network between the two electrode.

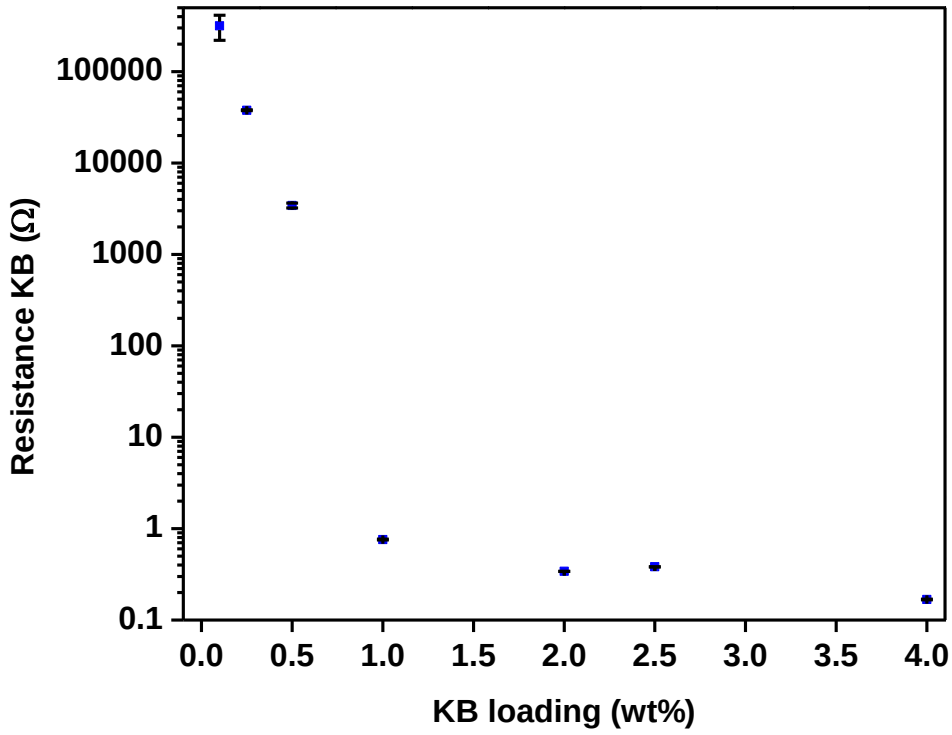

Figure 4.6: Measured DC electronic resistance of KB suspensions with respect to mass loading of KB in the suspensions.

Before we began work on with the unsubstituted PcM batteries, we cycled 51 mg slurries of KB again under the same conditions. The same linear response in the charge discharge curves was observed, but the KB was able to achieve a higher charge capacity ~ 39.8 C/g. This different observed charge capacity of KB could be due to a few factors. The overall cell resistance could be lower which would allow for more charge to be passed before the potential cut-off was hit. We also slightly changed our processing of KB from grinding the KB into a powder inside the glove box to bulk grinding outside the box. This may have led to an overall smaller particle size which would increase the surface area per gram of KB. This increased surface area may have potentially contributed to the higher charge capacity.

4.2.2. Electrochemical Characterizations

We previously synthesized and electrochemically characterized a series ^{OEt}PcM species and wanted to see if the unsubstituted PcM counterparts retained the same electrochemical properties.[15] The issue with electrochemically characterizing the unsubstituted PcM is their extremely low solubility in organic solvents. Solutions of PcM (PcVO, PcMnCl, PcFe, PcNi, and PcCu) were made up by adding 5 mg of the PcM to 5 mL of MeCN with $[Bu_4N][PF_6]$ (0.1M). The majority of the PcM solid did not dissolve into solution, but faint color changes suggest a dissolution of miniscule but non-zero quantities of PcM. This solution was decanted into a CV cell, leaving the solid behind. CVs taken of these solutions had redox events barely exceeded baseline capacitive current, so we ran differential pulse voltammetry (DPV) of the solutions to better resolve the redox events (Figure 4.7).

The DPVs for the PcM series did not align with the corresponding ^{OEt}PcM. PcVO had what appears to be to two possible reduction events and two possible oxidation events like ^{OEt}PcVO, but these events occurred at different potentials compared to the ^{OEt}PcVO events (Figure 4.7a). PcMnCl, PcFe, and PcNi all had potentially multiple reduction and oxidation events observed in the DPVs (Figure 4.7b-d). We are unsure if all of these redox events observed are from the PcM, due to the fact that the PcM used were all dye content varying between 85-95% purity. The DPVs of PcCu appeared relatively clean with an oxidation event and possibly two reduction events (Figure 4.7e). These DPVs showed that not all of the PcM series had two reversible oxidations and reductions like ^{OEt}PcMnN, so for testing as charge carriers we decided to treat them as one electron anolytes and catholytes.

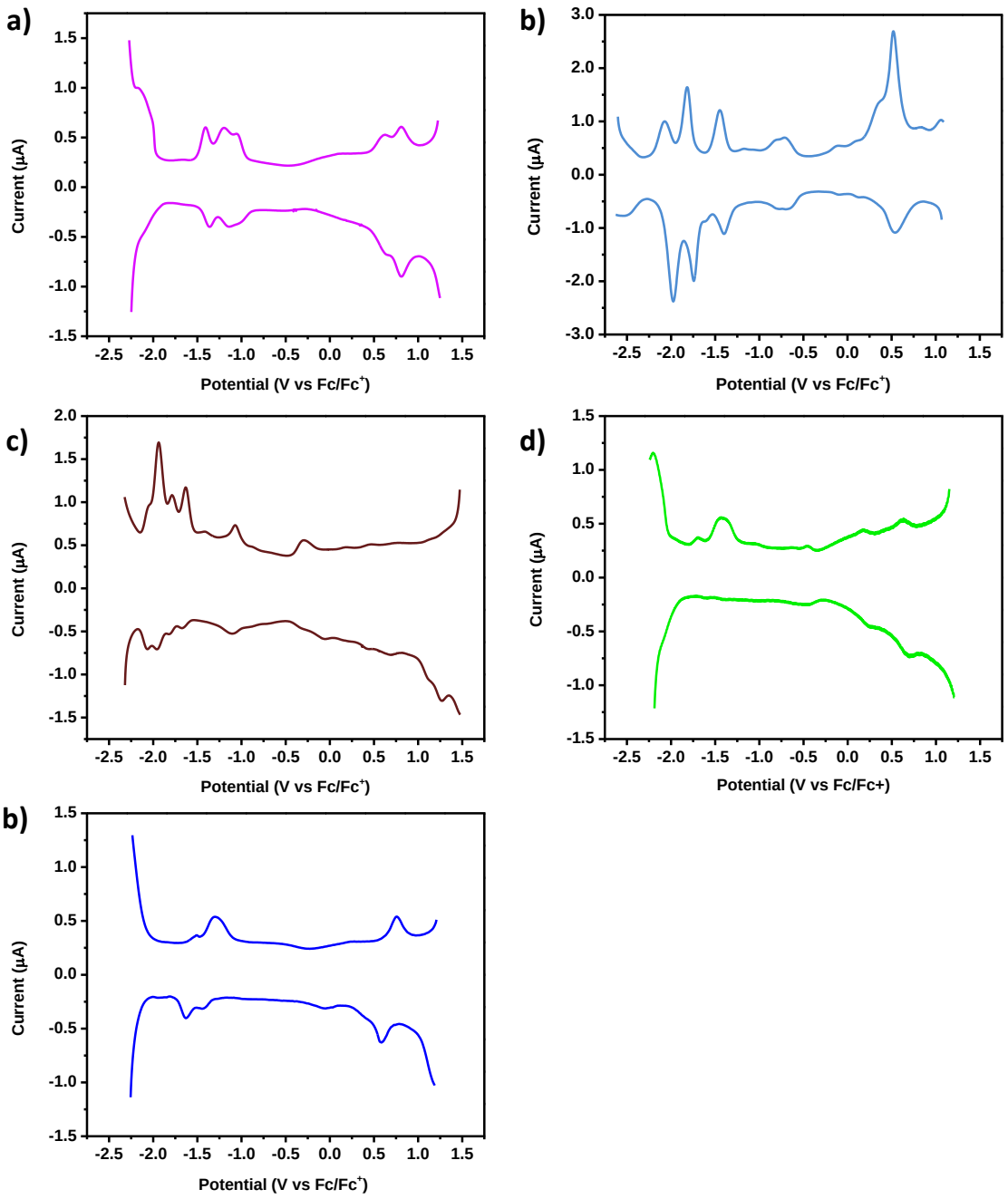

Figure 4.7: DPVs of various saturated solutions of PcM in 0.1 M $[Bu_4N][PF_6]$ MeCN using a glassy carbon working electrode, Pt counter and pseudoreference electrodes. a) PcVO, b) PcMnCl, c) PcFe, d) PcNi and e) PcCu.

4.2.3. Cell Cycling Experiment

With the base characteristics of KB cycling and the percolation network understood, we next began to characterize PcM/KB hybrid systems. For these studies, an approximate 1:2 PcM:KB mass ratio in 0.2 M $[Bu_4N][PF_6]$ MeCN solutions were used (unless otherwise specified). The charge-carrier properties were then tested by cycling between 75% and 0% of the theoretical state of charge (SOC) while applying 500 μA charging and -250 μA discharging currents.

We initially sought to compare ^{EtO}PcM vs. PcM solubility effects on overall performance by comparing two sets of compounds: metal axially substituted (^{EtO}PcVO vs. PcVO) and non-axially substituted (^{EtO}PcNi vs. PcNi) compounds. Both ^{OEt}PcVO/KB and PcVO/KB demonstrated high capacity retention (>99%, Figure 4.8a,c) with correspondingly high faradaic efficiencies (FE; > 98.6%, Figure 4.8b) excluding the first cycle. Average voltage efficiencies (VE; 63.6% (^{EtO}PcVO), 74% (PcVO)) and energy efficiencies (EE; 62.4% (^{EtO}PcVO), 72.8% (PcVO)) were similar although the PcVO/KB mixture showed marginally higher efficiencies (Figure 4.8 b). Slurries of ^{OEt}PcNi/KB and PcNi/KB also demonstrated high capacity retention (>99%; Figure 4.8d,f) and high FE (98.3% (^{EtO}PcNi), 96.7% (PcNi); Figure 4.8e). Average VE (63.6% (^{EtO}PcNi), 57.2% (PcNi)) and EE (62.5% (^{EtO}PcNi), 55.3% (PcNi)) were similar for both mixtures. ^{OEt}PcNi/KB mixture displayed slightly higher efficiencies than PcNi/KB (Figure 4.8e), however, we note that a decrease in VE and EE for this latter mixture was observed during the last three cycles. This decrease may be attributed to a clogged glass frit separator.

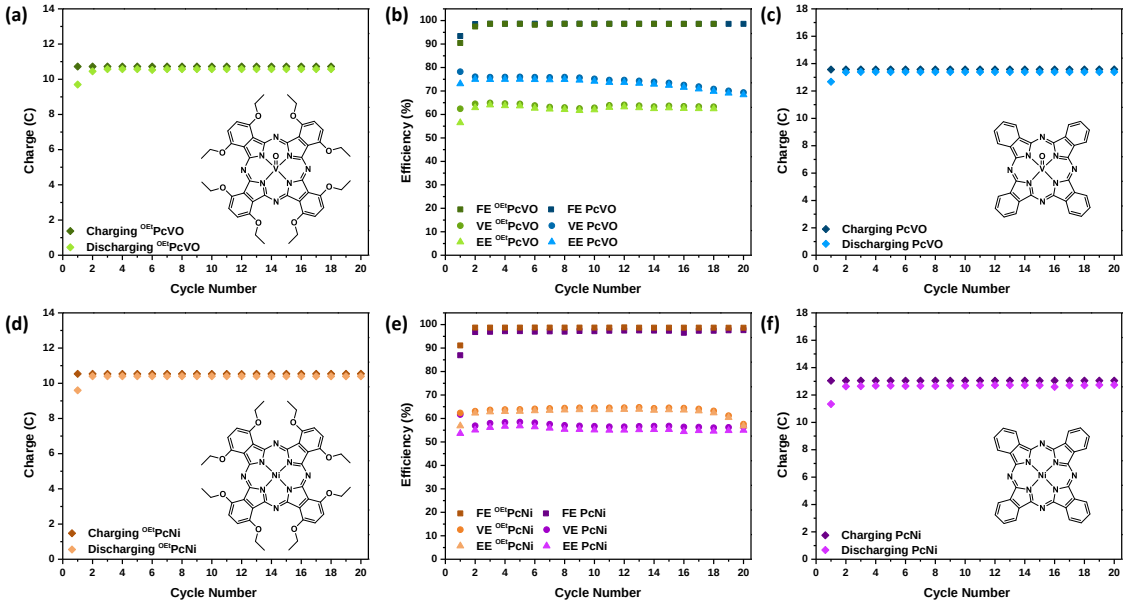

Figure 4.8: Galvanostatic charge-discharge measurements comparing ^{OEt}PcM and PcM in a glass-fritted H-cell with coiled Pt electrodes (500 µA charge, -250 µA discharge) and containing mixtures of PcM/KB in MeCN (5 mL per compartment) and $[Bu_4N][PF_6]$ (0.2 M). (a) Charge transfer plot for a ^{OEt}PcVO/KB (60.3 mg, 100.2 mg) slurry; theoretical capacity = 14.2 C. (b) FE, VE, and EE of galvanostatically charged ^{OEt}PcVO/KB and PcVO/KB slurries. (c) Charge transfer plot for a PcVO/KB (55.4 mg, 110 mg) slurry; theoretical capacity = 18 C. (d) Charge transfer plot for a ^{OEt}PcNi/KB (55 mg, 110 mg) slurry; theoretical capacity = 14 C. (e) FE, CE, and EE of galvanostatically charged ^{OEt}PcNi/KB and PcNi/KB slurries. (f) Charge transfer plot for a PcNi/KB (48.9 mg, 11.7 mg) slurry; theoretical capacity = 17.3 C.

These results indicate that the performance metrics of the soluble (^{EtO}PcVO, ^{EtO}PcNi) versus the virtually insoluble (PcVO, PcNi) charge-carriers do not differ substantially. The percolation network generated by KB allowed for the insoluble PcM to be charged to the desired state of charge while still maintaining high efficiencies. Moreover, strong ligation to the axial position of the metal center – e.g., PcVO vs. PcNi – appeared to play little role in the

performance of these systems. This is surprising given our previous report on ethoxy-functionalized first row PcM electrochemistry showed that late metal species (^{EtO}PcCo, ^{EtO}PcNi, and ^{EtO}PcCu) containing no axially-bound ligands displayed non-diffusional electrode adsorption in their cyclic voltammograms. In contrast, axially-substituted early metal species (^{EtO}PcVO, ^{EtO}PcMnN) showed diffusional, quasi-reversible redox events.[15] The results presented here (Figure 4.8) suggest that no correlation exists between these observed CV trends and the charge-discharge experiments. Given that the performance was independent of peripheral Pc ring substitution, we were inspired to further expand our charge carrier scope to commercially available PcM derivatives ($PcTiCl_2$, PcMnCl, PcFe, PcCo, PcCu, and PcPb).

Using the conditions detailed above, the galvanostatic charge-discharge curves for $PcTiCl_2$/KB and PcMnCl/KB achieved charging capacities greater than KB alone (Figure 4.9a-b, left). Notably these charge-discharge curves appeared highly capacitive in nature, with most of the E vs Q traces appearing linear like the KB cycles (Figure 4.9). While these slurries maintained moderate VE and EE of ~60% over the course of 20 cycles, the observed FE (> 96.5%) fluctuated between cycles due to inconsistent discharge capacities Figure 4.9a-b, right). The PcFe/KB slurry had similar VE and EE values (> 60%), but in contrast maintained a stable FE > 98.6% (Figure 4.9c, right). The galvanostatic charge-discharge curves for PcFe/KB appeared to have more faradaic contribution over the course of a cycle leading to a less linear response compared to the $PcTiCl_2$/KB and PcMnCl/KB slurries (Figure 4.9c, left). The later metal systems, namely the PcCo/KB and PcCu/KB systems, performed optimally maintaining high FE (> 98.4%), VE (> 69%), and EE (> 68%) values (Figure 4.9d-e, right). The galvanostatic charge-discharge curves for both slurries displayed a mixture of capacitive and faradaic components (Figure 4.9d-e, left). Both retained >99% capacity over course of

cycling, with the PcCu/KB running over 50 cycles. We lastly wanted to test a heavier metal commercial PcM species, PcPb, as a comparison to the 3d species. While the observed charge-discharge curves for the PcPb/KB slurry also displayed a mix of capacitive and faradaic components (Figure 4.9f, left) akin to the late metal first-row species, the FE, VE, and EE values decayed over time (Figure 4.9f, right) to ~ 6% after 20 cycles, indicating that PcPb is not a stable charge carrier.

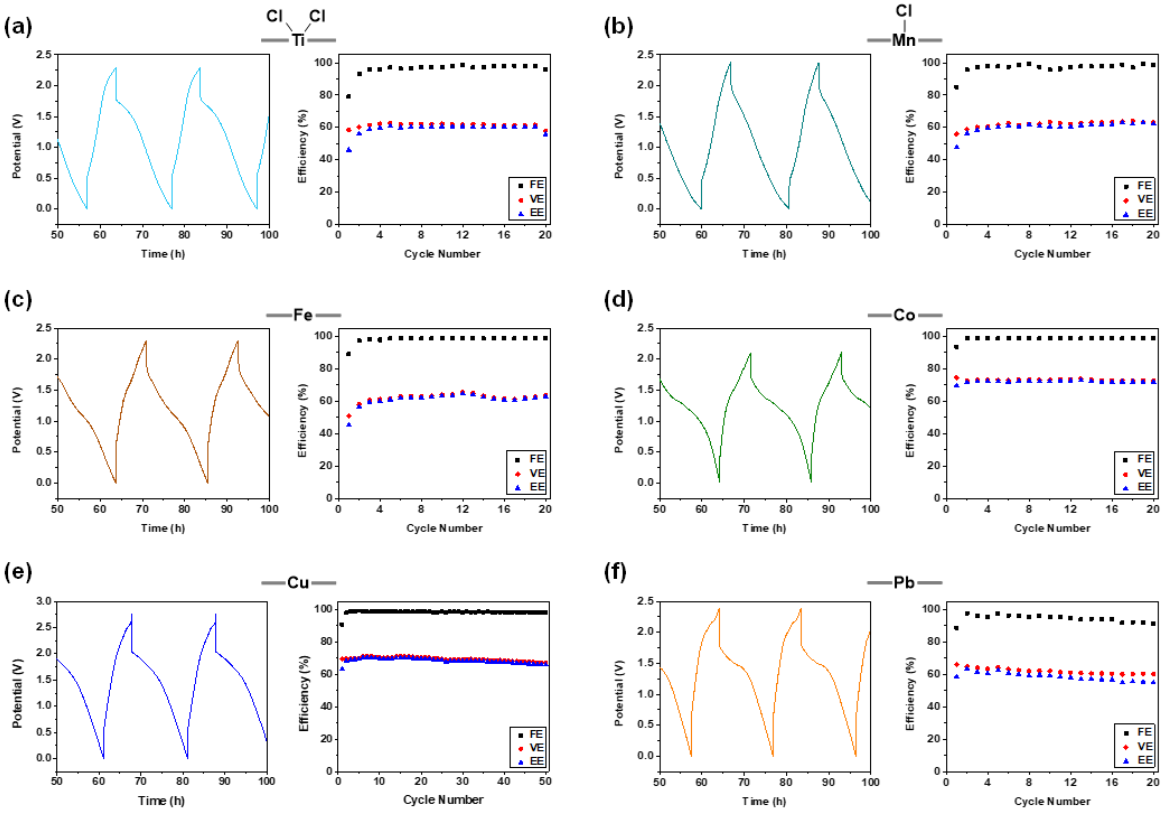

Figure 4.9: Galvanostatic charge-discharge measurements of various PcM in MeCN (5 mL per compartment) with $[Bu_4N][PF_6]$ (0.2 M) in a glass frit H-cell using coiled Pt working electrodes at a 500 µA charge, -250 µA discharge rate. (a) Galvanostatic charge-discharge curves of $PcTiCl_2$/KB (53.1 mg, 102.6 mg) slurry with a theoretical capacity of 16.3 C. FE, CE, EE of galvanostatically charged $PcTiCl_2$/KB slurry. (b) Galvanostatic charge-discharge curves of PcMnCl/KB (53 mg, 103.5 mg) slurry with a theoretical capacity of 16.7 C. FE, CE,

EE of galvanostatically charged PcMnCl/KB slurry. (c) Galvanostatic charge-discharge curves of PcFe/KB (53.4 mg, 105.3 mg) slurry with a theoretical capacity of 17.5 C. FE, CE, EE of galvanostatically charged PcFe/KB slurry. (d) Galvanostatic charge-discharge curves of PcCo/KB (54.1 mg, 102.7 mg) slurry with a theoretical capacity of 17.34 C. FE, CE, EE of galvanostatically charged PcCo/KB slurry (e) Galvanostatic charge-discharge curves of PcCu/KB (50 mg, 110 mg) slurry with a theoretical capacity of 17.1 C. FE, CE, EE of galvanostatically charged PcCu/KB slurry. (f) Galvanostatic charge-discharge curves of PcPb/KB (48.9 mg, 112.7 mg) slurry with a theoretical capacity of 15.8 C. FE, CE, EE of galvanostatically charged PcPb/KB slurry.

While screening the PcM/KB systems, we observed inconsistencies in charge-discharge behavior and high ohmic drops when using glass frits as the separator in our H-cells. For instance, the galvanostatic charge-discharge curves would often diverge in shapes (capacitive vs Faradaic), have varying initial potentials and inconsistent FE, VE and EE between cycles (Figure 4.10).

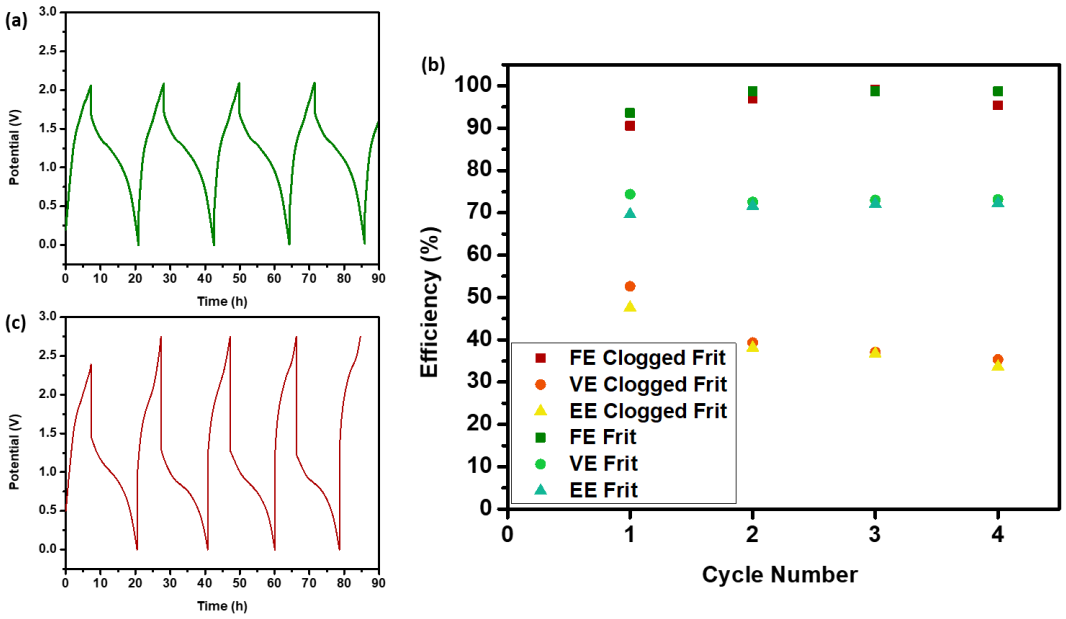

Figure 4.10: Comparison of Galvanostatic cycling experiments for PcCo/Kb slurry using a H-Cell with a glass-frit (cell resistance~464 Ω) and clogged glass-frit (cell resistance~1063 Ω). (a) Galvanostatic, two-electrode charge-discharge curves for Kb and PcCu slurry with glass-frit (b) FE, VE, and EE with frit and clogged frit. (c) Galvanostatic, two-electrode charge-discharge curves for Kb and PcCu slurry with clogged glass-frit.

We measured the resistance of these H-cells using a current interrupt technique with a 1 mM ferrocene/ferrocenium couple dissolved in MeCN in 0.2 M $[Bu_4N][PF_6]$ supporting electrolyte. The cell resistance ranged from 464-1063 Ω (Figure 4.11a-b) for the different cells. Exchange of the glass frit separators for a glass wool barrier yielded a more consistent ionic resistance of ~480 Ω (Figure 4.11c). When no separator was used, the resistance in an H-cell with similar geometry to the fritted cells was measured to be 454 Ω (Figure 4.11d), only ~10-25 Ω lower than an unclogged glass frit or glass wool barrier. To further lower the internal resistance, we increased the $[Bu_4N][PF_6]$ concentration to 0.5 M. This resulted in a

resistance of 318 Ω for the cells with the glass wool separator (Figure 4.11e). We then utilized these updated conditions to test our higher energy density cells using these conditions.

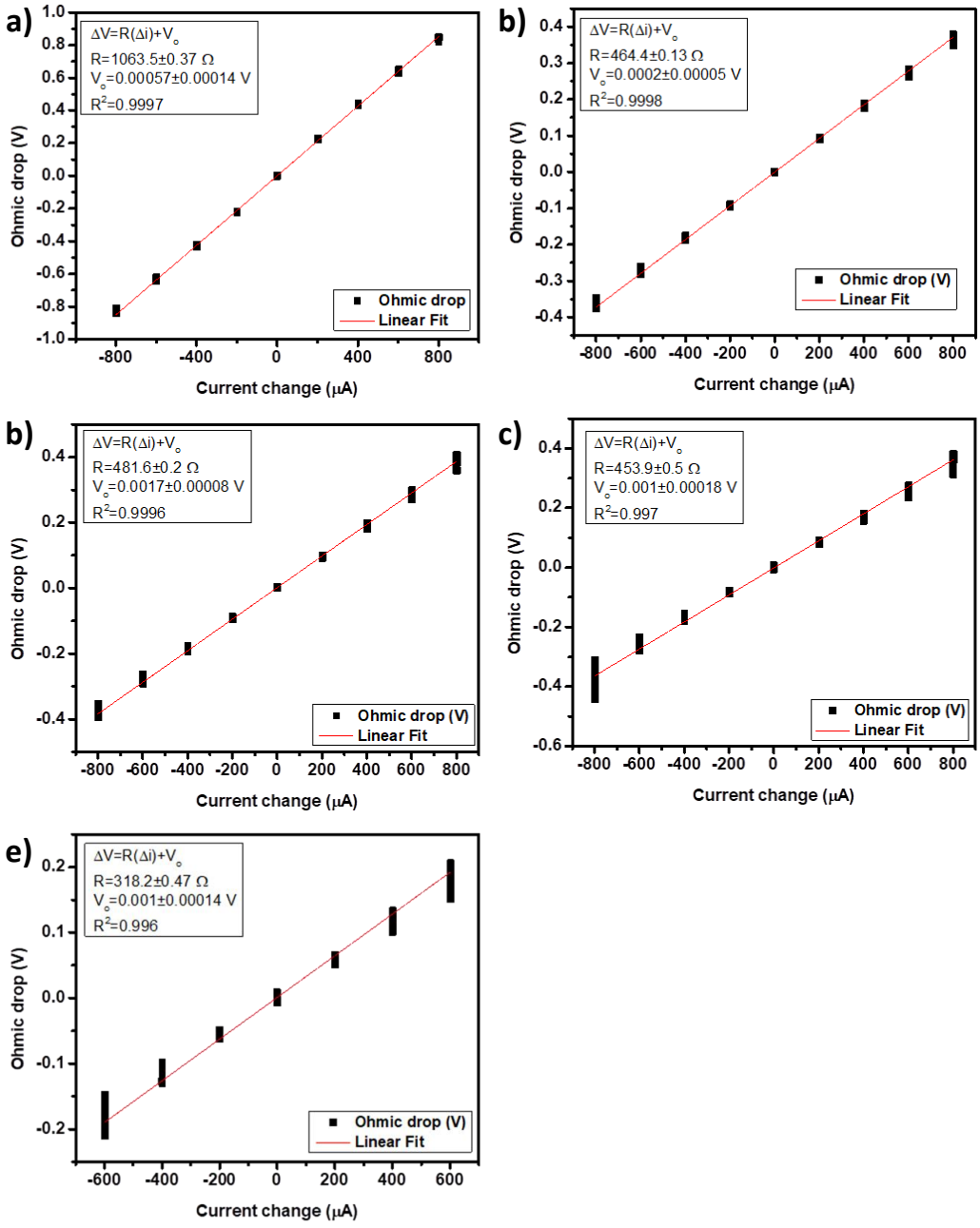

Figure 4.11: Ohmic potential drop versus change in applied current plots. a) H-cell with a clogged glass-frit with $[Bu_4N][PF_6]$ (0.2 M) MeCN. b) H-Cell with a non-clogged glass-fritwith $[Bu_4N][PF_6]$ (0.2 M) MeCN. c) H-Cell with a glass-wool separatorwith $[Bu_4N][PF_6]$ (0.2 M) MeCN. d) H-Cell with no barrierbetween compartments with $[Bu_4N][PF_6]$ (0.2 M) MeCN. e) H-Cell with glass-wool separatorwith $[Bu_4N][PF_6]$ (0.5 M) MeCN.

Due to PcCu stability, high efficiency metrics, and low cost, we chose to use it in higher energy density cells. We doubled the loading amount of PcCu to 100.4 mg while maintaining the same loading of KB. This 1:1 weight ratio of PcCu to KB led to inconsistent charging with noticeable differences being observed in the charge-discharge curves between cycles (Figure 4.12a). Some cycles hit the potential cut-off early, while others were able to achieve the desired SOC. Fluctuations in the FE and VE were also observed and the VE began to steadily decrease during the last 3 cycles (Figure 4.12c). An increase in the coloration of the anolyte solution was observed for this cell when fully charged compared to the lower loaded cell. The color likely comes from the reduced $[PcCu]^{-1}$ species being soluble in solution. The glass wool slowly began to have a noticeable amount of colored solution penetrate it after a few cycles, and the anolyte species would have likely crossed over to the catholyte side had the cell ran longer. In addition to this, the Pt coiled electrodes had a blue coating of PcCu on them when the cell was disassembled. This coating was not removed by rinsing with solvents, which normally works to remove the PcCu/KB slurry. The coating, however, was able to be removed by sonication. This coating on the Pt electrodes may have increased the resistance of the cell and had a role in the fluctuations between cycles.

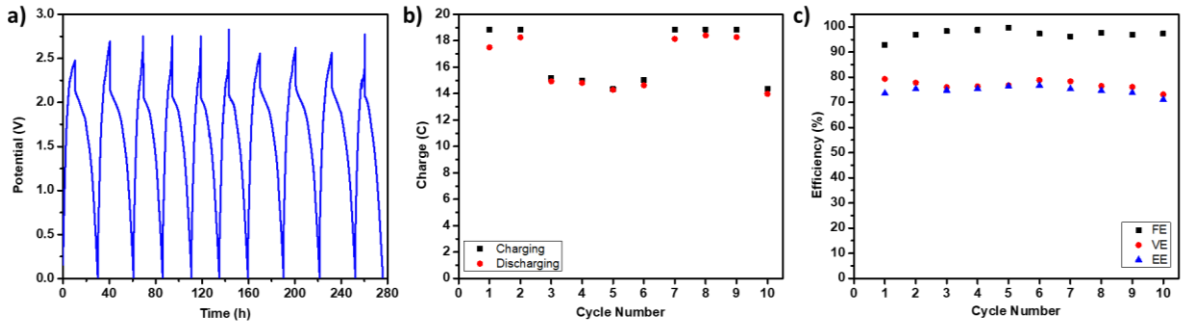

Figure 4.12: Galvanostatic charge-discharge cycles of a PcCu/KB slurry (100.4 mg PcCu, 102 mg KB) with a theoretical capacity of 24.7 C in MeCN (5 mL per compartment) with $[Bu_4N][PF_6]$ (0.5 M) as supporting electrolyte using a glass wool separated H-Cell and coiled Pt working electrodes at 500 µA charge and -250 µA discharge rates. (a) Galvanostatic charge-discharge curves. (b) Charge transfer plot for PcCu/KB slurry. (c) Calculated FE, CE, and EE values for this system.

By doubling the loading of both PcCu and KB, maintaining the 1:2 weight ratio, we were able to achieve an energy density of 1.23 Wh/L (Figure 4.13). No crossover was observed in the glass wool separator, likely due to the additional KB providing enough surface area to keeping the reduce PcCu from being dissolved in solution. Lower ohmic drops were also observed compared to the previous glass frit cells. The cell maintained a high capacity retention > 99% and demonstrated high FE (98.3%), VE (83.5%) and EE (82%) over 25 cycles (Figure 4.13b-c).

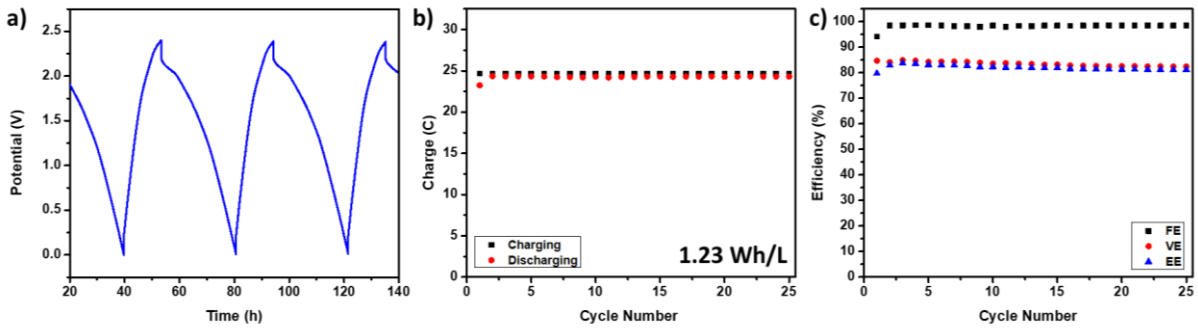

Figure 4.13: Galvanostatic charge-discharge cycles of a PcCu/KB slurry (100.4 mg PcCu, 201.5 mg KB) with a theoretical capacity of 32.9 C in MeCN (5 mL per compartment) with $[Bu_4N][PF_6]$ (0.5 M) as supporting electrolyte using a glass wool separated H-Cell and coiled Pt working electrodes at 500 µA charge and -250 µA discharge rates.(a) selected curves. (b) Charge transfer plot for PcCu/KB slurry. (c) Calculated FE, CE, and EE values for this system.

We wanted to further increase the energy density of the cell but had already maxed out the loading capacity of KB, so we increased the loading of PcCu to 152 mg (1:1.33 PcCu:KB). Only 8 cycles of this cell were achieved due to a potentiostat malfunction. Over those 8 cycles the cell maintained >98.4 % FE but did have a decline in the VE (Figure 4.14a-c). A small amount of crossover of the anolyte into the glass wool was observed while cycling like the 1:1 ratio cell. Even though the cell was able to achieve an energy density of 1.69 Wh/L, the 1:1.33 ratio was not further tested due to observed crossover and decline in VE.

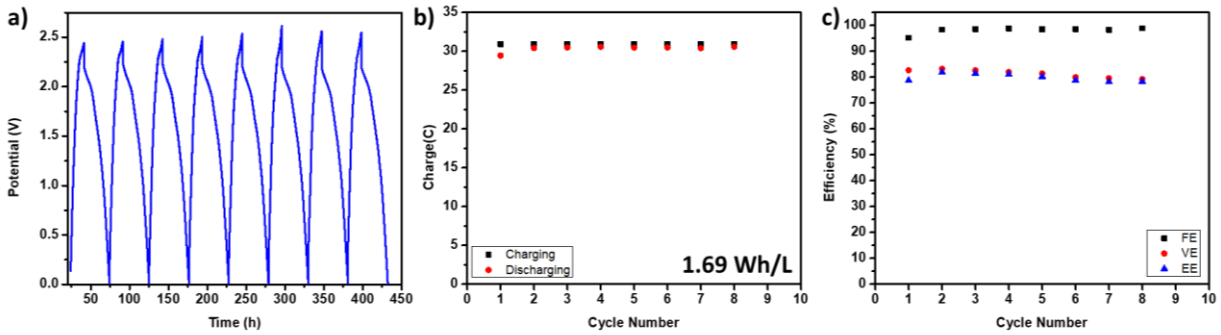

Figure 4.14: Galvanostatic charge-discharge cycles of a PcCu/KB slurry (152 mg PcCu, 201 mg KB) with a theoretical capacity of 41 C in MeCN (5 mL per compartment) with $[Bu_4N][PF_6]$ (0.5 M) as supporting electrolyte using a glass wool separated H-Cell and coiled Pt working electrodes at 500 µA charge and -250 µA discharge rates.(a) Galvanostatic charge-discharge curves. (b) Charge transfer plot for PcCu/KB slurry. (c) Calculated FE, CE, and EE values for this system.

4.3. Summary

The results presented herein offer a comparison of different metal and ring substitution patterns for PcM/KB slurry-based systems for RFB applications. We found that while both ^{OEt}PcVO and ^{OEt}PcNi substituted charge carriers were stable when cycled in conjunction with a KB percolation network, neither showed any significant performative advantages over their unsubstituted counterparts. Indeed, the use of commercially available PcM complexes resulted in improved efficiencies and stability and offered the opportunity for significant cost reductions for these systems. We found that PcCu, an inexpensive commercially produced paint dye, offered the highest efficiencies, stability, and energy density of all charge carriers used. Its calculated cost amounted to ~$73/kWh making it a significantly less-expensive charge carrier than V (~$300/kWh), today's state-of-the-art charge carrier.[6] With an already

developed industrial supply chain and low cost, PcCu could serve as a scalable charge carrier in conjunction with KB for slurry-based RFBs.

4.4. Experimental

4.4.1. Materials and Methods

Techniques and Reagents. HPLC grade Acetonitrile (Fisher Chemical) was dried over activated 4 Å molecular sieves for 24 hours under a nitrogen atmosphere on a Schlenk line, filtered through celite, then distilling over CaH_2 (ACROS Organics), and stored in a glovebox over activated 4 Å molecular sieves. Tetrabutylammonium hexafluorophosphate ($[Bu_4N][PF_6]$) (Oakwood Chemicals) was twice recrystallized from hot ethanol and dried at 50 °C under dynamic vacuum (<0.1 torr) for 24 hours before use. Ketjenblack® EC-600JD (KB) purchased from a private supplier was ground using a mortar-pestle and dried in an oven overnight at 150 °C prior to use. $PcTiCl_2$, PcVO, PcMnCl, PcFe, PcCo, PcNi, and PcPb were purchased from Sigma-Aldrich and used without further purification. PcCu was purchased from Kremer Pigmente and washed with ethanol followed by diethyl ether before being used. ^{OEt}PcVO and ^{OEt}PcNi were synthesized by our previously reported method.[15]

Cycling Experiments: All electrochemical measurements were performed in a glovebox under an inert argon atmosphere using a Metrohm Autolab PGSTAT128N potentiostat/galvanostat. Two coiled Pt electrodes (Bio-Logic) were cleaned before use by rinsing with acetone and heating white-hot with a butane torch. All electrodes were transferred into the glovebox and subsequently rinsed with the respective electrolyte solution immediately prior to use. The H-cells were custom-made by the in-house glassblower and oven dried overnight at 150 °C prior to use. KB and PcM were combined with 5 mL of 0.2 M $[Bu_4N][PF_6]$ in MeCN to each compartment of an H-cell and stirred overnight. Cells were cycled by

applying 500 µA charge and -250 µA discharge current with time cut offs based on theoretical 75% and 0% state of charge along with safety voltage cut offs set as well.

Electrochemical impedance measurements: The electrochemical impedance measurements in this work were performed using a Biologic multi-channel VMP3 potentiostat capable of PEIS measurements controlled using EC-Lab V11.43. The impedance data was modelled using ZFit module within the EC-Lab program.

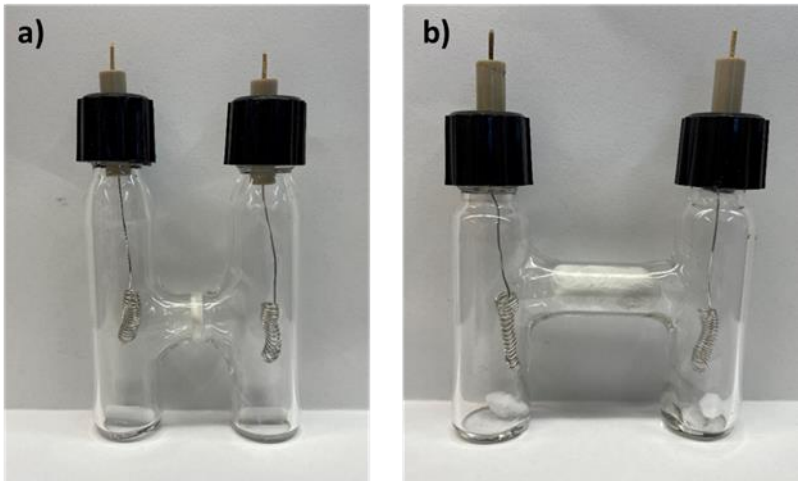

Figure 4.15: H-cell designs. (a) Fine Porosity Glass frit separated H-cell setup with high surface area coiled Pt electrodes. (b) Glass wool separated H-cell setup with high surface area coiled Pt electrodes

4.4.2. Galvanostatic Cycling Calculations

These calculations were done based on the template of our previously published work.[21]

Efficiency Metrics

Faradaic efficiency (FE) is defined by:

(4.1) $FE = \frac{Q_{discharge}}{Q_{charge}} \times 100\%$

where Q is charge transferred.

Voltage efficiency (VE) is defined by:

(4.2) $VE = \frac{V_{mean,discharge}}{V_{mean,charge}} \times 100\%$

where V_{mean} is the mean voltage over the charging or discharging periods.

Energy efficiency (EE) was defined by:

(4.3) $EE = \frac{(FE \times VE)}{100\%}$

Energy Density Calculations:

For the calculation of energy density, several assumptions were necessary:

1) The number of electrons transferred per PcM was 1.
2) The V_{cell} was determined from the $V_{cell,\ discharge}$ from the experimental cycling data.
3) KB provides a capacity of 39.8 C/g , was estimated based on the experimental data.

The energy density of the slurry-state Pc ($\widehat{E_{Pc}}$) contribution was defined by Eqn. S4.4:

(4.4) $\widehat{E_{Pc}} = 0.5nV_{cell}C_{active}F$

Where n is the number of electrons transferred, V_{cell} is the cell potential, C_{active} is the concentration of the active species, and F is Faraday's constant.

The energy density of the slurry-state KB ($\widehat{E_{KB}}$) contribution was defined by Eqn. S4.5:

(4.5) $\widehat{E_{KB}} = \frac{qV_{cell}}{Vol}$

Where q is the total charge transferred calculated using assumption 3 from and Vol is the volume of electrolyte solution used.

In cycling experiments where both Pc and KB were used, the total energy density ($\widehat{E_{total}}$) was determined using Eqn. S4.6:

(4.6) $\left(\widehat{E_{total}}\right) = \widehat{E_{Pc}} + E_{KB}$

4.4.3. Cell Cycling Data

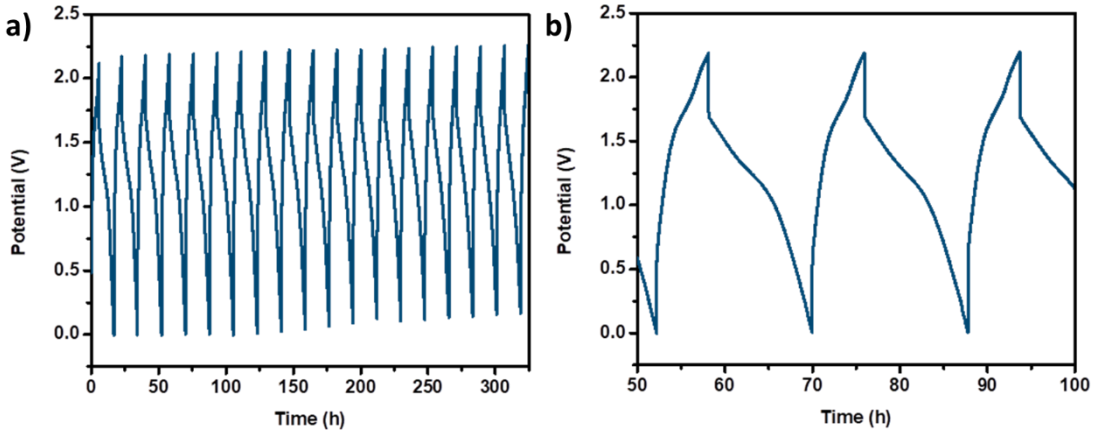

Figure 4.16: Galvanostatic charge-discharge curves of a ^{OEt}PcVO/KB slurry (60.3/100.2 mg/compartment) taken in a glass-fritted H-cell in MeCN (5 mL/compartment) with $[Bu_4N][PF_6]$ (0.2 M) supporting electrolyte and using coiled Pt working and counter electrodes (500 µA charge, -250 µA discharge). a) Full data set, b) Selected curves

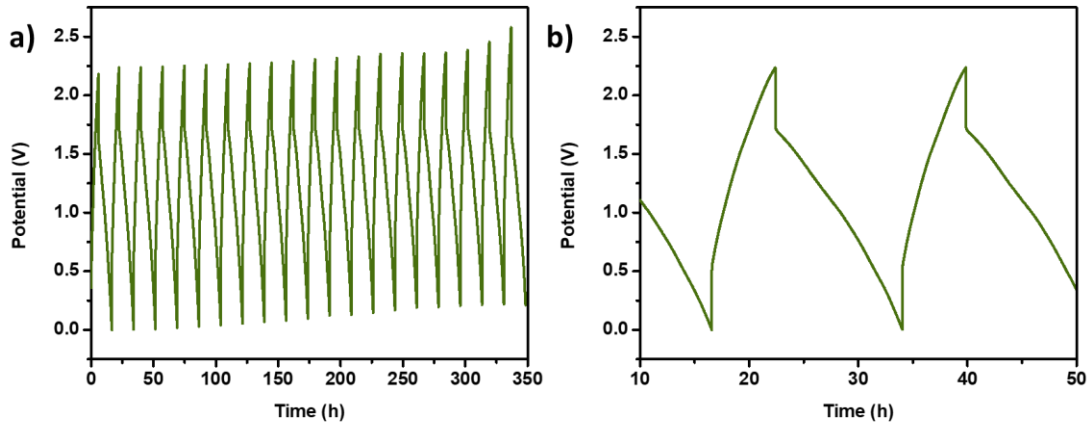

Figure 4.17: Galvanostatic charge-discharge curves of a ^{OEt}PcNi/KB slurry (50/110 mg/compartment) taken in a glass-fritted H-cell in MeCN (5 mL/compartment) with $[Bu_4N][PF_6]$ (0.2 M) supporting electrolyte and using coiled Pt working and counter

electrodes (500 µA charge, -250 µA discharge). a) Full data set, b) Selected curves. *Note a higher potential cut-off of 2.75 V was used due to the H-cell having a high resistance.

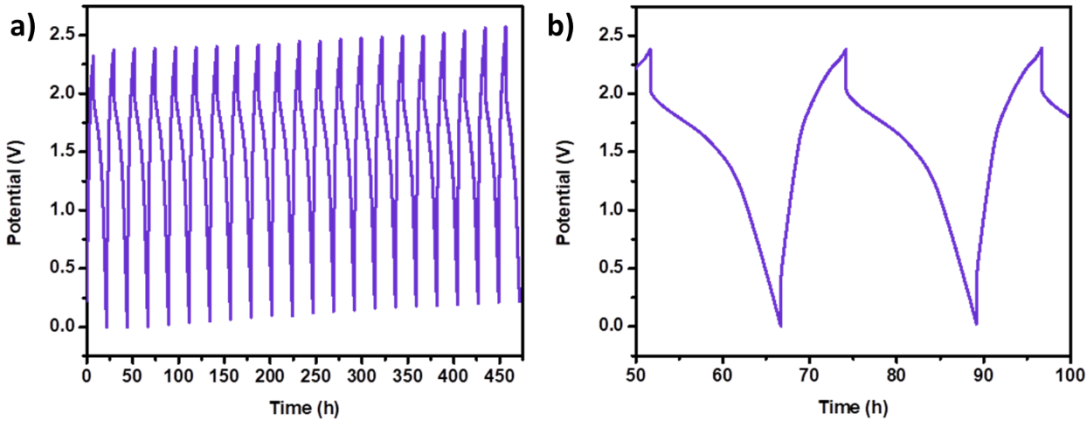

Figure 4.18: Galvanostatic charge-discharge curves of a PcVO/KB slurry (55.4/110 mg/compartment) taken in a glass-fritted H-cell in MeCN (5 mL/compartment) with $[Bu_4N][PF_6]$ (0.2 M) supporting electrolyte and using coiled Pt working and counter electrodes (500 µA charge, -250 µA discharge). a) Full data set, b) Selected curves.

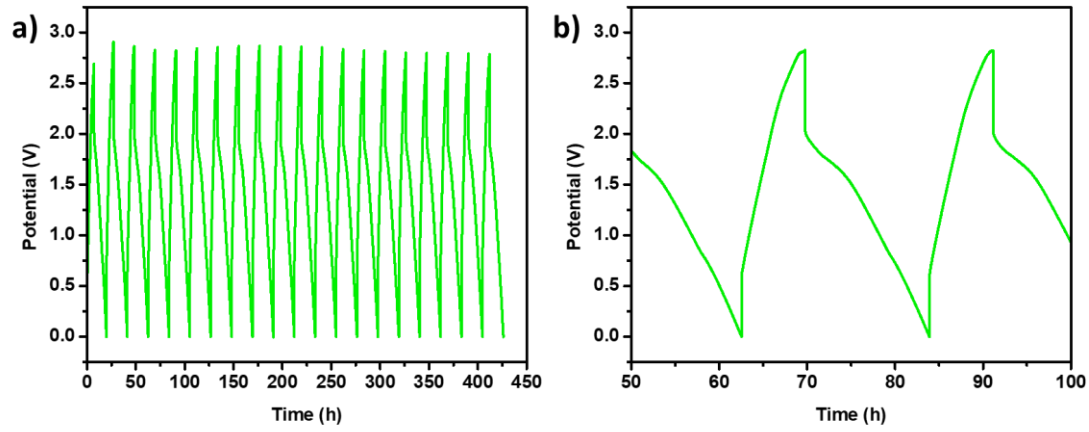

Figure 4.19: Galvanostatic charge-discharge curves of a PcNi/KB slurry (48.9/111.7 mg/compartment) taken in a glass-fritted H-cell in MeCN (5 mL/compartment) with

$[Bu_4N][PF_6]$ (0.2 M) supporting electrolyte and using coiled Pt working and counter electrodes (500 µA charge, -250 µA discharge). a) Full data set, b) Selected curves.

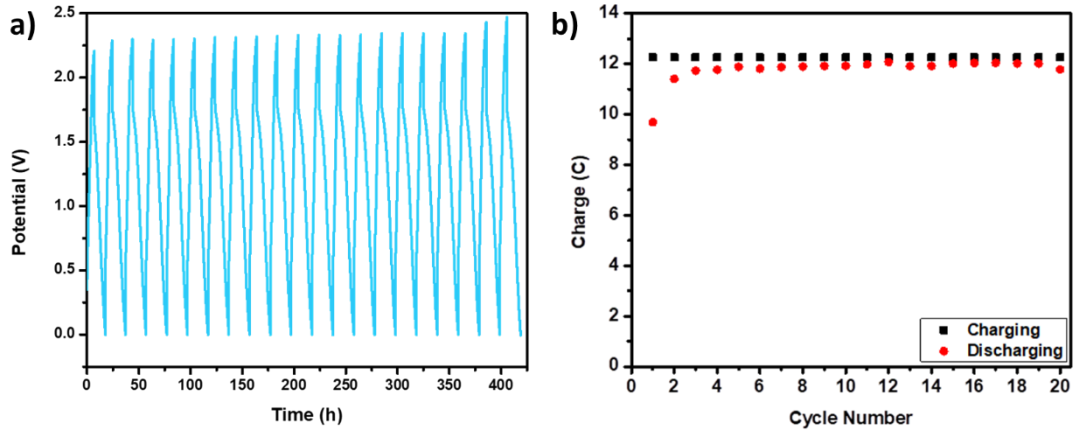

Figure 4.20: Galvanostatic charge-discharge curves of a $PcTiCl_2$/KB slurry (53.1/102.6 mg/compartment) taken in a glass-fritted H-cell in MeCN (5 mL/compartment) with $[Bu_4N][PF_6]$ (0.2 M) supporting electrolyte and using coiled Pt working and counter electrodes (500 µA charge, -250 µA discharge). a) Full data set, d) Charge transfer value.

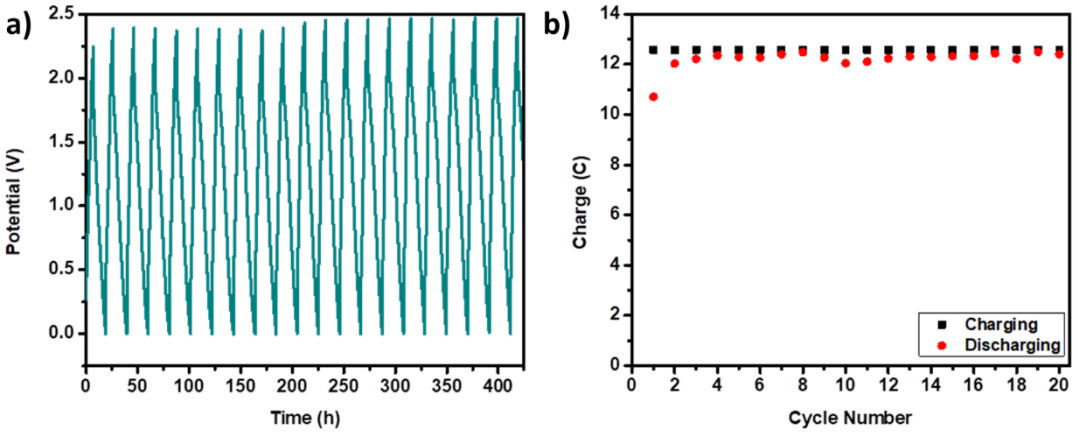

Figure 4.21: Galvanostatic charge-discharge curves of PcMnCl /KB slurry (53/103.5 mg/compartment) taken in a glass-fritted H-cell in MeCN (5 mL/compartment) with

[Bu_4N][PF_6] (0.2 M) supporting electrolyte and using coiled Pt working and counter electrodes (500 µA charge, -250 µA discharge). a) Full data set, d) Charge transfer value.

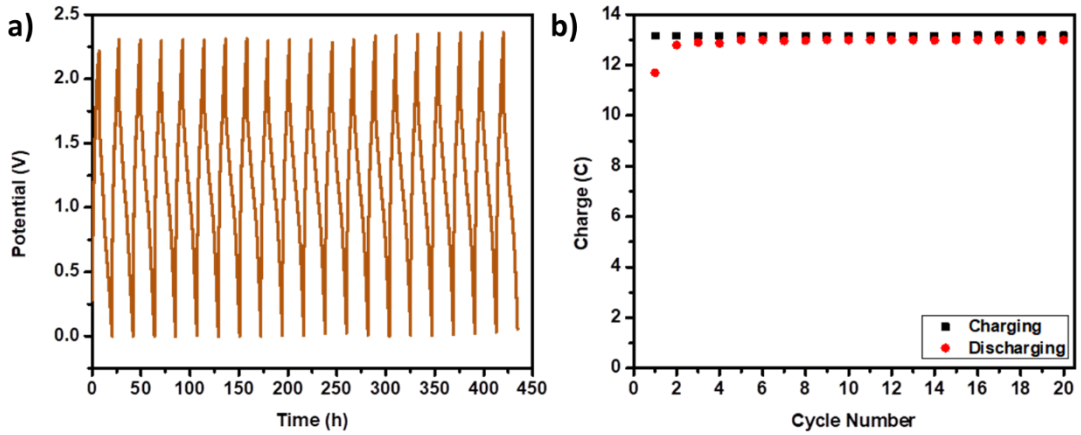

Figure 4.22: Galvanostatic charge-discharge curves of PcFe/KB slurry (53.4/105.3 mg/compartment) taken in a glass-fritted H-cell in MeCN (5 mL/compartment) with [Bu_4N][PF_6] (0.2 M) supporting electrolyte and using coiled Pt working and counter electrodes (500 µA charge, -250 µA discharge). a) Full data set, d) Charge transfer value.

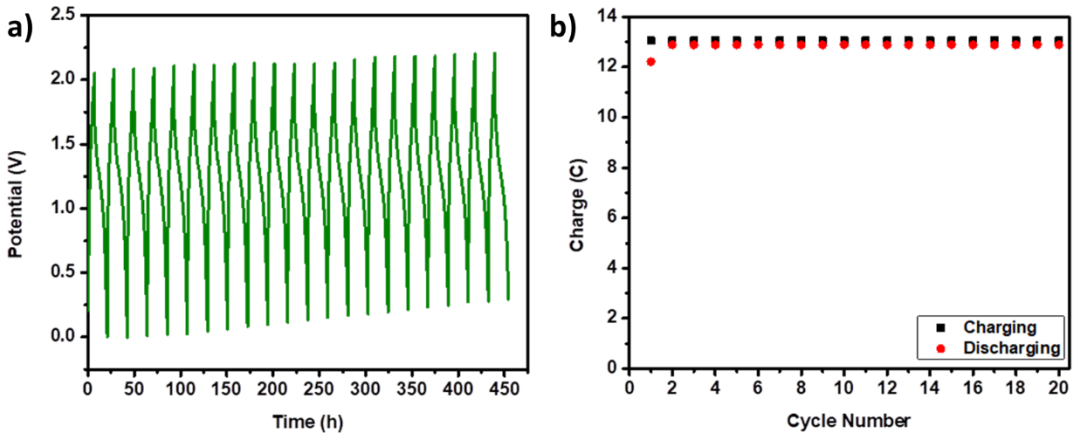

Figure 4.23: Galvanostatic charge-discharge curves of PcCo/KB slurry (54.1/102.7 mg/compartment) taken in a glass-fritted H-cell in MeCN (5 mL/compartment) with $[Bu_4N][PF_6]$ (0.2 M) supporting electrolyte and using coiled Pt working and counter electrodes (500 µA charge, -250 µA discharge). a) Full data set, d) Charge transfer value.

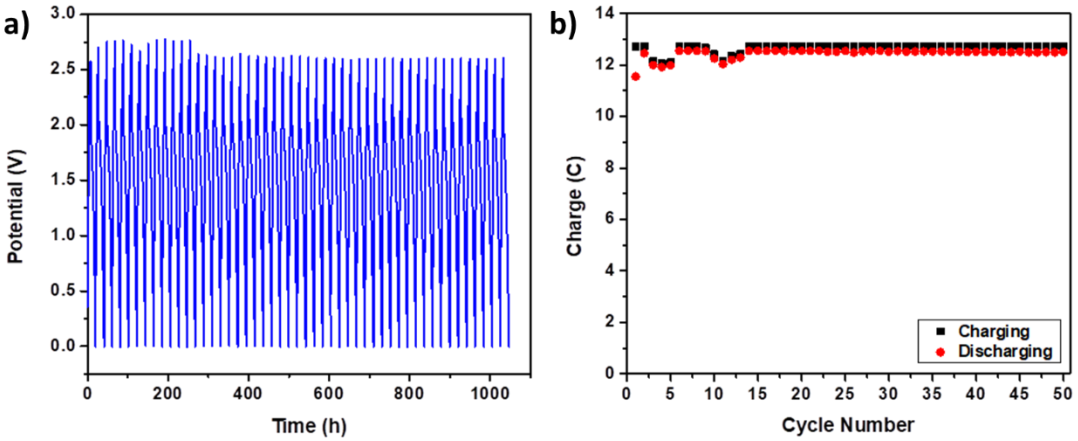

Figure 4.24: Galvanostatic charge-discharge curves of PcCu/KB slurry (50/110 mg/compartment) taken in a glass-fritted H-cell in MeCN (5 mL/compartment) with $[Bu_4N][PF_6]$ (0.2 M) supporting electrolyte and using coiled Pt working and counter

electrodes (500 µA charge, -250 µA discharge). a) Full data set, d) Charge transfer value. *Note a higher potential cut-off of 2.75 V was used due to the H-cell having a high resistance.

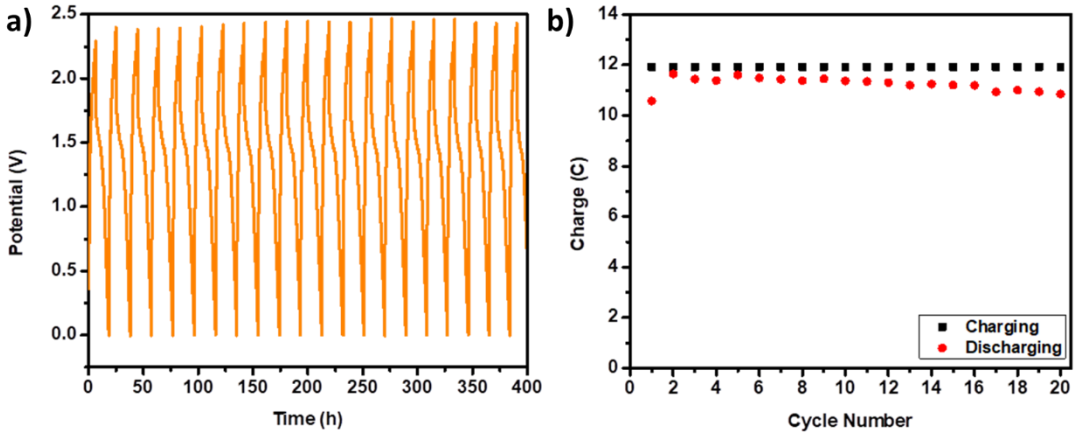

Figure 4.25: Galvanostatic charge-discharge curves of PcPb/KB slurry (54.7/106.5 mg/compartment) taken in a glass-fritted H-cell in MeCN (5 mL/compartment) with $[Bu_4N][PF_6]$ (0.2 M) supporting electrolyte and using coiled Pt working and counter electrodes (500 µA charge, -250 µA discharge). a) Full data set, d) Charge transfer value.

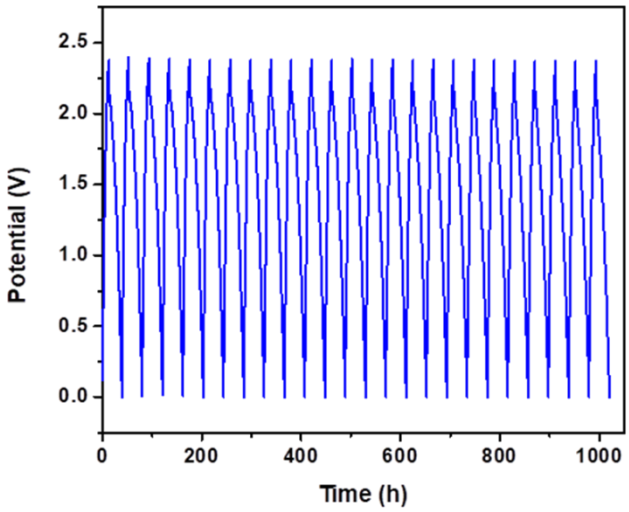

Figure 4.26: Galvanostatic charge-discharge curves of PcCu/KB slurry (100.4/201.5 mg/compartment) taken in a glass-wool H-cell in MeCN (5 mL/compartment) with $[Bu_4N][PF_6]$ (0.2 M) supporting electrolyte and using coiled Pt working and counter electrodes (500 µA charge, -250 µA discharge).

4.4.4. Current Interrupt for Resistance Measurement

Each side of an H-Cell (glass-frit, glass-wool, or no barrier) was filled with 5 mL of a solution containing equimolar (1 mM) ferrocene and ferrocenium hexafluorophosphate in MeCN with 0.2 or 0.5 M $[Bu_4N][PF_6]$. High surface area platinum electrodes were used to apply rapid 2.0 s long current pulses of variable magnitude (±200 µA, ±400 µA, ±600 µA and ±800 µA) separated by 10 s of relaxation at OCP across the H-cell while the potential across the cell was measured. We observed steps in the cell potential synchronous with the current pulse edges corresponding to the ohmic spike/drop (ΔV equal to the product of the cell resistance (R) and change in the current (Δi) offset about the open circuit potential (V_o) of the cell. We verified

the linear dependence of the cell potential change on the current pulse via a least-square linear fit, with slope equal to the cell resistance:

(4.7)$\Delta V = R(\Delta i) + V_o$.[22]

4.5. Reference

(1) California ISO. *Managing Oversupply*. 2022. http://www.caiso.com/informed/Pages/ManagingOversupply.aspx (accessed 2022 6/2).

(2) Dunn, B.; Kamath, H.; Tarascon, J.-M. Electrical Energy Storage for the Grid: A Battery of Choices. *Science* **2011**, *334* (6058), 928-935. DOI: 10.1126/science.1212741.

(3) Huang, Y.; Gu, S.; Yan, Y.; Li, S. F. Y. Nonaqueous redox-flow batteries: features, challenges, and prospects. *Curr. Opin. Chem. Eng.* **2015**, *8*, 105-113. DOI: https://doi.org/10.1016/j.coche.2015.04.001.

(4) Weber, A. Z.; Mench, M. M.; Meyers, J. P.; Ross, P. N.; Gostick, J. T.; Liu, Q. Redox flow batteries: a review. *J. Appl. Electrochem.* **2011**, *41* (10), 1137-1164. DOI: 10.1007/s10800-011-0348-2.

(5) DOE. *Energy Storage Grand Challenge Cost and Performance Assessment 2020*; DOE/PA-0204; 2020. https://www.energy.gov/energy-storage-grand-challenge/downloads/2020-grid-energy-storage-technology-cost-and-performance.

(6) Minke, C.; Kunz, U.; Turek, T. Techno-economic assessment of novel vanadium redox flow batteries with large-area cells. *J. Power Sources* **2017**, *361*, 105-114. DOI: https://doi.org/10.1016/j.jpowsour.2017.06.066.

(7) Soloveichik, G. L. Flow Batteries: Current Status and Trends. *Chem. Rev.* **2015**, *115* (20), 11533-11558. DOI: 10.1021/cr500720t.

(8) Potash, R. A.; McKone, J. R.; Conte, S.; Abruña, H. D. On the Benefits of a Symmetric Redox Flow Battery. *J. Electrochem. Soc.* **2016**, *163* (3), A338-A344. DOI: 10.1149/2.0971602jes.

(9) Li, Z.; Smith, K. C.; Dong, Y.; Baram, N.; Fan, F. Y.; Xie, J.; Limthongkul, P.; Carter, W. C.; Chiang, Y.-M. Aqueous semi-solid flow cell: demonstration and analysis. *Phys. Chem. Chem. Phys.* **2013**, *15* (38), 15833-15839, 10.1039/C3CP53428F. DOI: 10.1039/C3CP53428F.

(10) Duduta, M.; Ho, B.; Wood, V. C.; Limthongkul, P.; Brunini, V. E.; Carter, W. C.; Chiang, Y.-M. Semi-Solid Lithium Rechargeable Flow Battery. *Adv. Energy Mater.* **2011**, *1* (4), 511-516. DOI: 10.1002/aenm.201100152.

(11) Tomai, T.; Saito, H.; Honma, I. High-energy-density electrochemical flow capacitors containing quinone derivatives impregnated in nanoporous carbon beads. *J. Mater. Chem. A* **2017**, *5* (5), 2188-2194, 10.1039/C6TA08733G. DOI: 10.1039/C6TA08733G.

(12) Presser, V.; Dennison, C. R.; Campos, J.; Knehr, K. W.; Kumbur, E. C.; Gogotsi, Y. The Electrochemical Flow Capacitor: A New Concept for Rapid Energy Storage and Recovery. *Adv. Energy Mater.* **2012**, *2* (7), 895-902. DOI: 10.1002/aenm.201100768.

(13) Hunt, C.; Peterson, M.; Anderson, C.; Chang, T.; Wu, G.; Scheiner, S.; Ménard, G. Switchable Aromaticity in an Isostructural Mn Phthalocyanine Series Isolated in Five Separate Redox States. *J. Am. Chem. Soc.* **2019**, *141* (6), 2604-2613. DOI: 10.1021/jacs.8b12899.

(14) Hunt, C.; Mattejat, M.; Anderson, C.; Sepunaru, L.; Ménard, G. Symmetric Phthalocyanine Charge Carrier for Dual Redox Flow Battery/Capacitor Applications. *ACS Appl. Energy Mater.* **2019**, *2* (8), 5391-5396. DOI: 10.1021/acsaem.9b01317.

(15) Peterson, M.; Hunt, C.; Wang, Z.; Heinrich, S. E.; Wu, G.; Ménard, G. Synthesis, characterization, and electrochemical properties of a first-row metal phthalocyanine series. *Dalton Transactions* **2020**, *49*, 16268-16277, 10.1039/D0DT01372B. DOI: 10.1039/D0DT01372B.

(16) Leznoff, C. C.; Lever, A. B. P. Phthalocyanines: Properties and Applications. Wiley VCH: New York, NY, 1989.

(17) L'Her, M.; Pondaven, A. 104 - Electrochemistry of Phthalocyanines. In *The Porphyrin Handbook*, Kadish, K. M., Smith, K. M., Guilard, R. Eds.; Academic Press, 2003; pp 117-169.

(18) Reports, M. I. *Global Phthalocyanine Pigments Market Size, Manufacturers, Supply Chain, Sales Channel And Clients, 2021-2027*. 2021. https://www.marketinsightsreports.com/reports/08123167729/global-phthalocyanine-pigments-market-size-manufacturers-supply-chain-sales-channel-and-clients-2021-2027 (accessed 2022 6/24).

(19) Wanser, S. *Industry & Trade Summary: Synthetic Organic Pigments*; United States International Trade Commission 1997. https://www.usitc.gov/publications/docs/pubs/industry_trade_summaries/pub3021.pdf.

(20) Mattejat, M.; Peterson, M.; Chakraborty, A.; Ménard, G. Dyeing to Carry Charge: Commercial Phthalocyanine Dyes as Charge Carriers for Redox Flow Battery Applications. *Energy Fuels* **2023**, *37* (1), 785-790. DOI: 10.1021/acs.energyfuels.2c03389.

(21) Hunt, C.; Mattejat, M.; Anderson, C.; Sepunaru, L.; Ménard, G. Symmetric Phthalocyanine Charge Carrier for Dual Redox Flow Battery/Capacitor Applications. *ACS Applied Energy Materials* **2019**, *2*, 5391-5396. DOI: 10.1021/acsaem.9b01317.

(22) Larminie, J. R. J. Current interrupt techniques for circuit modelling. In *IEE Colloquium on Electrochemical Measurement*, 17-17 March 1994, 1994; pp 12/11-12/16.

Chapter 5 Metal Cyclam as Symmetric Charge Carriers

5.1. Introduction

Currently aqueous V-based RFBs are the closest to commercialization, but remain cost prohibitive in part due the scarcity and high price of raw vanadium.[1] Switching to cheaper earth abundant metals such as iron, cobalt and nickel can help reduce the total cost of charge carriers. Several organic-based symmetric charge carriers have also been proposed as cheap alternatives to vanadium, but often suffer from a loss of capacity over time.[2] Cycling between metal-borne redox states avoids potential ligand-centered organic radical-based decomposition pathways.[3] Other design principles that can be implemented to increase the stability of charge carriers include ensuring the all the redox states have like charges, either positive or negative, to bimolecular decomposition pathways and using bulky ligands. Cationic charge carriers experience mutual Columbic repulsion from each other can help inhibit bimolecular parasitic/decomposition reactions. The use of bulky ligands can help physically isolate metal-centered reactivity from other compounds in solution.

We were interested in applying these design principles for symmetric charge carriers using earth abundant first row transition metals (iron, cobalt and nickel) bearing redox innocent ligands. Cyclam (1,4,8,11-tetraazacyclotetradecane) and its derivatives such as TMC (l,4,8,ll-tetramethyl-l,4,8,ll-tetraazacyclotetradecane) have a rich library of metal complexes with transition metals in several oxidation states.[4] Many of these metal complexes have been demonstrated to have metal centered reversible oxidation and reduction events. These redox events have been shown to be tunable, with the addition of the methyl groups to the amines on cyclam shifting the potentials of oxidation and reduction events anodically. Spectroscopy studies have demonstrated that with each methyl addition to cyclam the ligand field strength decreases leading to the anodic shifts in potentials.[5]

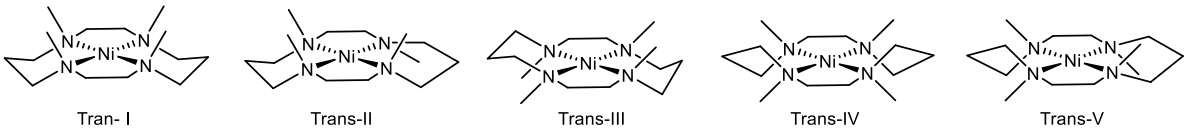

Figure 5.1: Diastereomers of Ni(TMC)

Five diastereomers are known for cyclam and TMC metal complexes (Figure 5.1). The trans-I complex for TMC generally in achieved by direct metalation of TMC ligand, while the trans-III can be afforded by the deprotonation and methylation of metal coordinated cyclam complexes.[4-6] The redox behavior of the trans I and III $[Ni(TMC)]^{2+}$ are reported to be similar to each, while having a 0.59 V anodic shift compared to $[Ni(Cyclam)]^{2+}$.

$[Ni(Cyclam)](ClO_4)_2$ has been previously demonstrated as a charge carrier for RFB applications.[7] A potential difference of 2.55 V between the Ni(I/II) and Ni(II/III) couples was observed in CVs taken in MeCN. Non-flow cycling experiments were conducted on $[Ni(Cyclam)](ClO_4)_2$ in an ethylene carbonate propylene carbonate solution and showed stable cycling between a 0 and 30% SOC.

In this chapter, we wanted to further explore $[Ni(Cyclam)]^{2+}$ and $[Ni(TMC)]^{2+}$ as charge carriers with cycling conditions more closely aligned with RFB applications. We electrochemically characterized a series of $[M(Cyclam)](BF_4)_2$ (M = Fe , Co , Ni) and the trans I and III $[Ni(TMC)](BF_4)_2$ by CV. Cycling experiments of $[Ni(Cyclam)](BF_4)_2$, Trans(I)-$[Ni(TMC)](BF_4)_2$, and Trans(III)-$[Ni(TMC)](BF_4)_2$ were performed revealing instability in the Ni(I) species, making them not suitable charge carriers.

5.2. Results and Discussion

5.2.1. Synthesis and Characterization

Following previously reported methods, transition metal (Fe, Co, Ni) cyclam complexes were synthesized by mixing the desired metal salts with cyclam overnight.[5] All metal cyclam complexes were crystalized to ensure purity before performing electrochemical techniques. solid state structure was acquired for [Ni(Cyclam)]$(BF_4)_2$ by single-crystal XRD studies **(**Figure 5.2**).**

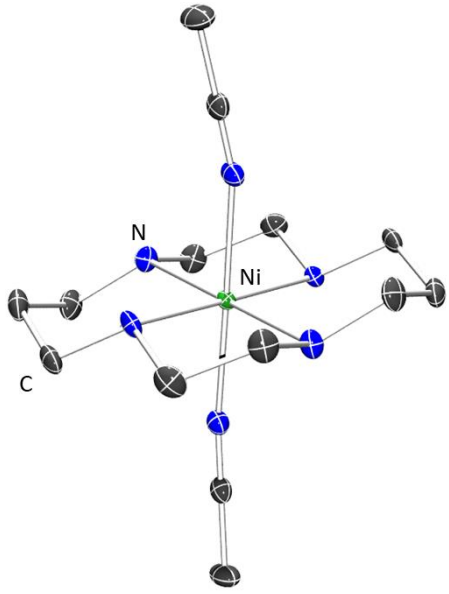

Figure 5.2: Solid-state molecular structure of [Ni(Cyclam)]$(BF_4)_2$. Hydrogen atoms and counter anions omitted for clarity

The tans(I)-[Ni(TMC)]$(BF_4)_2$ was synthesized following a modified literature procedure.[6] Similar to the cyclam metal complexes, the trans(I)-[Ni(TMC)]$(BF_4)_2$ was synthesized by mixing the $Ni(BF_4)_2$ salt with TMC overnight. trans(I)-[Ni(TMC)]$(BF_4)_2$ was characterized by NMR spectroscopy.

The trans(III)-[Ni(TMC)]$(BF_4)_2$ was synthesized following literature procedure.[5] The synthesis was accomplished by a two-step methylation of [Ni(Cyclam)]$(BF_4)_2$. Trans(III)-[Ni(TMC)]$(BF_4)_2$ was characterized by NMR spectroscopy and single-crystal XRD studies (Figure 5.3)

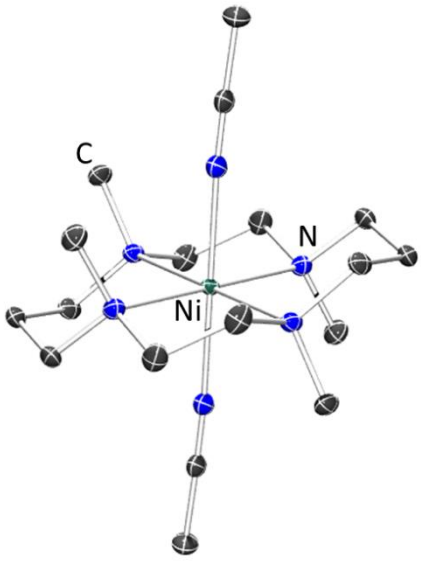

Figure 5.3: Solid-state molecular structure of trans(III)-[Ni(TMC)]$(BF_4)_2$. Hydrogens, and counter anions omitted for clarity.

5.2.2. Electrochemistry

CVs were performed for each metal cyclam complex which revealed quasi-reversible oxidation and reduction events for each complex. [Fe(+II)(Cyclam)]$(BF_4)_2$ had a single e^- oxidation event ($E_{1/2}$ = 0.31 V vs Fc/Fc^+) and possible two e^- reduction events ($E_{1/2}$ = -1.98 V vs Fc/Fc^+) (Figure 5.4a). The current magnitude of the reduction event was found to be approximately twice that of the oxidation, suggesting a 2 e^- reduction to form a neutral [Fe(0)(Cyclam)] species. The [Co(Cyclam)]$(BF_4)_2$ had the least reversible oxidation of the metal complexes, with a peak-to-peak separation of 0.19 V (Figure 5.4b). Similar to

[Fe(Cyclam)]$(BF_4)_2$, a potential two e^- reduction event was observed for [Co(Cyclam)]$(BF_4)_2$. [Ni(Cyclam)]$(BF_4)_2$ had reversible single e^- oxidation and reduction redox events (Figure 5.4c).

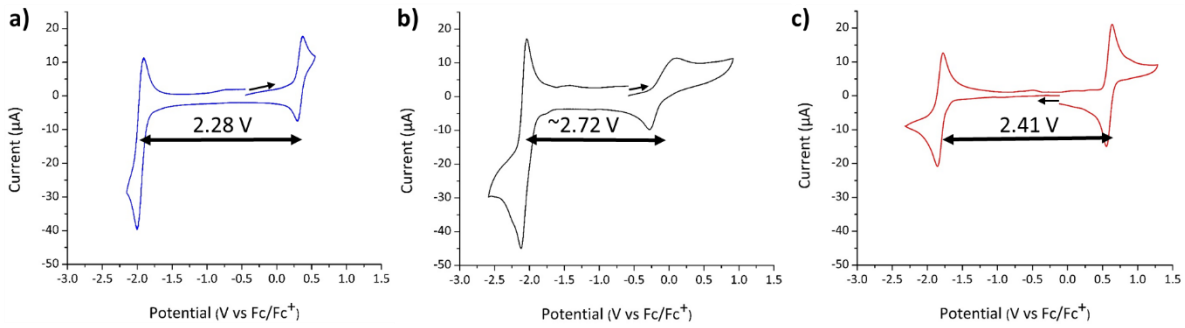

Figure 5.4: CVs comparing various metal cyclams (~1mM) in MeCN with [Bu_4N][BF_4] (0.1 M) using a glassy carbon working electrode and Pt counter and pseudoreference electrodes at a 0.1 V/s scan rate. a) [Fe(Cyclam)]$(BF_4)_2$ b) [Co(Cyclam)]$(BF_4)_2$ c) [Ni(Cyclam)]$(BF_4)_2$

The potential difference between the redox couples of a symmetric charge carrier correlates with the operational potential of a RFB. Higher potential differences are desirable as they help increase the energy densities of RFBs. The lowest potential gap observed for the metal cyclam complexes was [Fe(Cyclam)]$(BF_4)_2$ with 2.28 V (Figure 5.4a). The potential gap for [Co(Cyclam)]$(BF_4)_2$ was the highest at 2.72 V (Figure 5.4b). [Ni(Cyclam)]$(BF_4)_2$ had a slightly lower potential gap of 2.41 V (Figure 5.4c).

CVs of trans(III)-[Ni(TMC)]$(BF_4)_2$ were ran to compare to the redox events of [Ni(Cyclam)]$(BF_4)_2$ (Figure 5.5). The trans(III)-[Ni(TMC)]$(BF_4)_2$ had a similar one e^- quasi-reversible oxidation and reduction events to [Ni(Cyclam)]$(BF_4)_2$, but were both shifted anodically by ~0.4 V. These observed shifts are similar to other reported shifts comparing the same complexes but with different counter anions.[4] We believed this shift may be

advantageous for cycling experiments because it retains the same potential differences between redox events while making the Ni(I) species a weaker reducing agent.

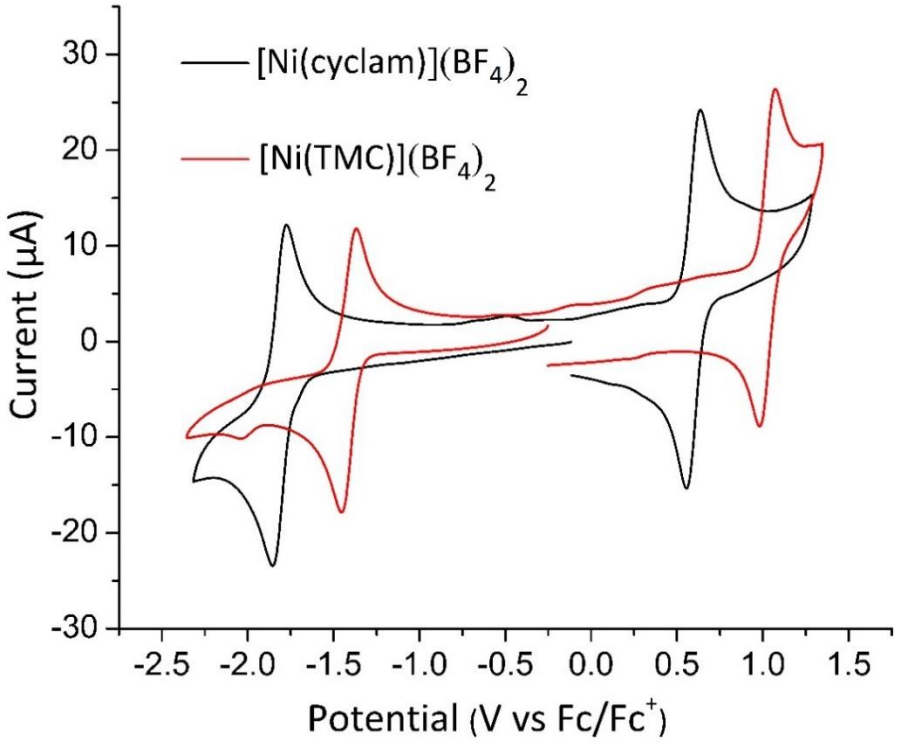

Figure 5.5: CVs comparing [Ni(cyclam)]$(BF_4)_2$ and trans(III)-[Ni(TMC)]$(BF_4)_2$ (~1mM) in MeCN with [Bu_4N][PF_6] (0.1 M) using a glassy carbon working electrode and Pt counter and pseudoreference electrodes at a 0.1 V/s scan rate.

CVs of trans(I)-[Ni(TMC)]$(BF_4)_2$ displayed three distinct oxidation events and three different reductions events. The first oxidation and reduction events of the trans(I)-[Ni(TMC)]$(BF_4)_2$ were close to the potentials of the quasi-reversible oxidation and reduction events of trans(III)-[Ni(TMC)]$(BF_4)_2$ (Figure 5.6). This complicated solution phase redox behavior of trans(I)-[Ni(TMC)]$(BF_4)_2$ qualitatively suggests complex equilibria between different isomers being generated besides the trans(I) isomer.

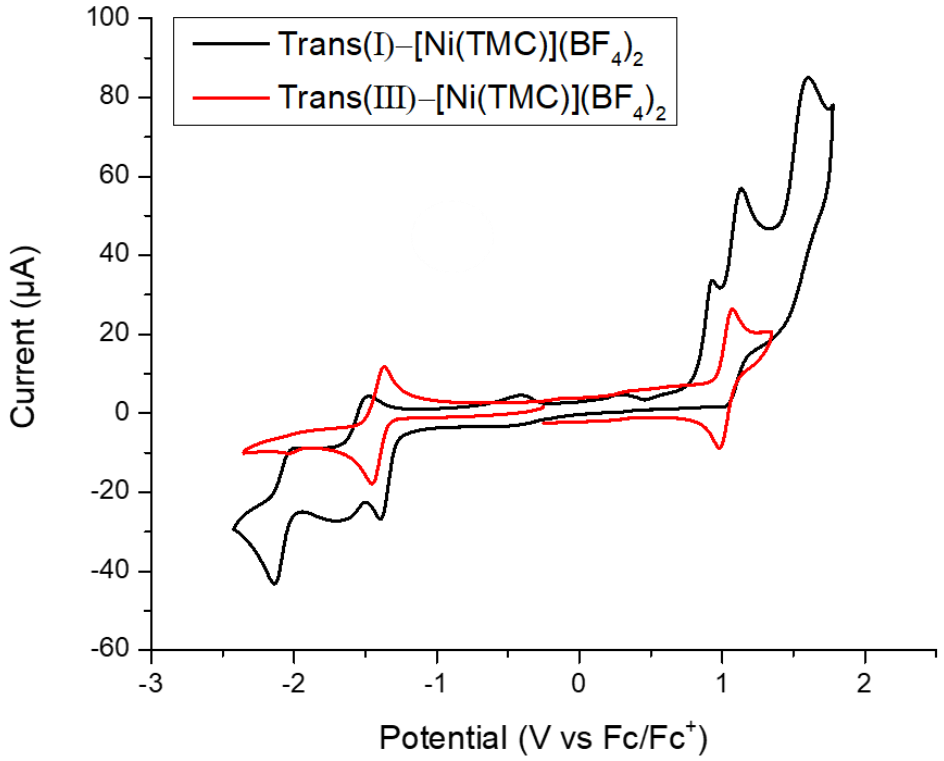

Figure 5.6: CVs comparing trans(I)-[Ni(TMC)]$(BF_4)_2$ and trans(III)-[Ni(TMC)]$(BF_4)_2$. (~1mM) in MeCN with [Bu_4N][PF_6] (0.1 M) using a glassy carbon working electrode and Pt counter and pseudoreference electrodes at a 0.1 V/s scan rate. **Cell Cycling Experiment**

We cycled the [Ni(Cyclam)]$(BF_4)_2$, trans(I)-[Ni(TMC)]$(BF_4)_2$, and trans(III)-[Ni(TMC)]$(BF_4)_2$ metal complexes that suggest the most chemically reversible redox. Solution state cycling of the metals complexes was performed in 0.2 M [Bu_4N][BF_4] MeCN in a glass frit separated H-Cell. They were cycled using high surface area Pt coil electrodes applying a 125 µA charging and -62.5 µA discharging currents.

The cycling experiments performed on [Ni(Cyclam)]$(BF_4)_2$ saw the capacity of the cell quickly declined from an initial capacity of 1.4 C to 0.5 C after only 5 cycles (Figure 5.7). A higher-than-expected charging potential and lower than expected discharging potential was

observed when cycling. The difference from the theoretical potential, 2.41 V (Figure 5.4c), was similar for the charging and discharging curves suggesting internal cell resistance was the main issue.

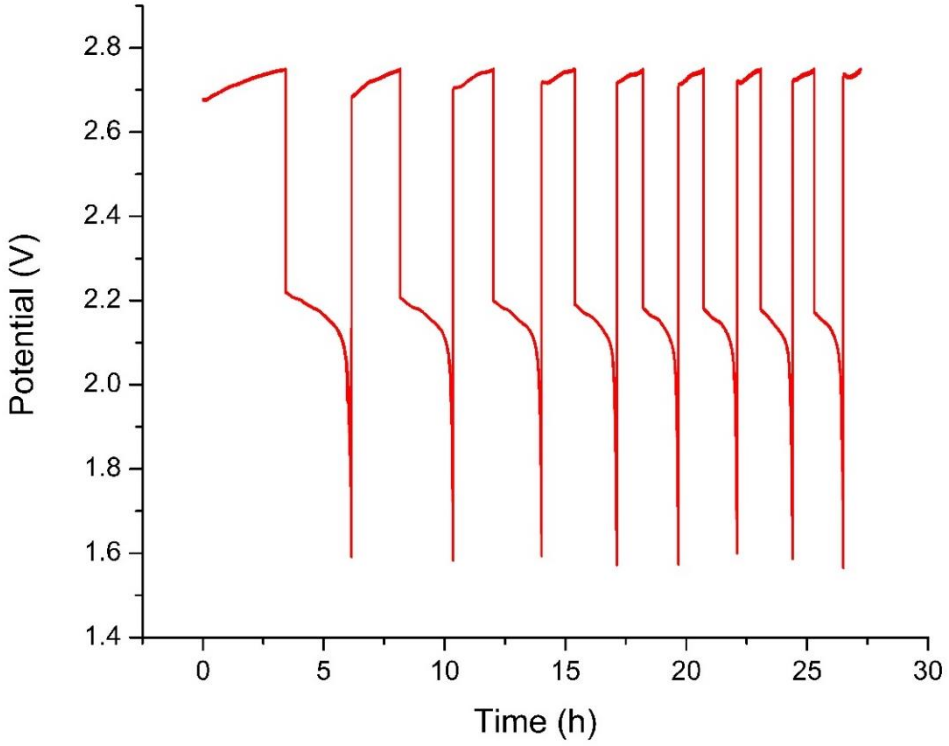

Figure 5.7: Galvanostatic charge-discharge curves of 0.014 M [Ni(cyclam)]$(BF_4)_2$ in 0.2 M [Bu_4N][BF_4] MeCN with Pt. electrode applying a 125 µA charging and -62.5 µA discharging current.

The degradation of the anolyte solutions in cells could visually be seen while cycling. We observed the reduced [Ni(Cyclam)](BF_4) species change over time from a clear purple solution when fully charged to a pink solution with a white precipitate after 50 cycles (Figure 5.8). This suggest the reduced Ni(I) species is an unstable species driving much of the degradation of the cell capacity.

Figure 5.8: Pictures tracking the degradation of [Ni(cyclam)]$(BF_4)_2$ while cycling

We ran open circuit potential (OCP) stability tests on [Ni(Cyclam)]$(BF_4)_2$ to see if any of the components of the cell were contributing to the instability of the Ni(I) species. The cells were charged to roughly a 75% SOC and the OCP subsequently measured at regular intervals (Figure 5.9). If the charged states of [Ni(Cyclam)]$(BF_4)_2$ were stable and not self-discharging, we would observe the OCP hold steady over a long period of time. We tested a variety of different conditions including swapping to a PF_6^- counter anion and electrolyte, using glassy carbon electrodes, lower potential charge cut offs, and using a different glovebox (over concerns of oxygen contamination). None of these changes affected the outcome of the OCP stability test, with the OCP declining rapidly over time for each experiment and visually showing the same signs of degradation observed in the cycling tests.

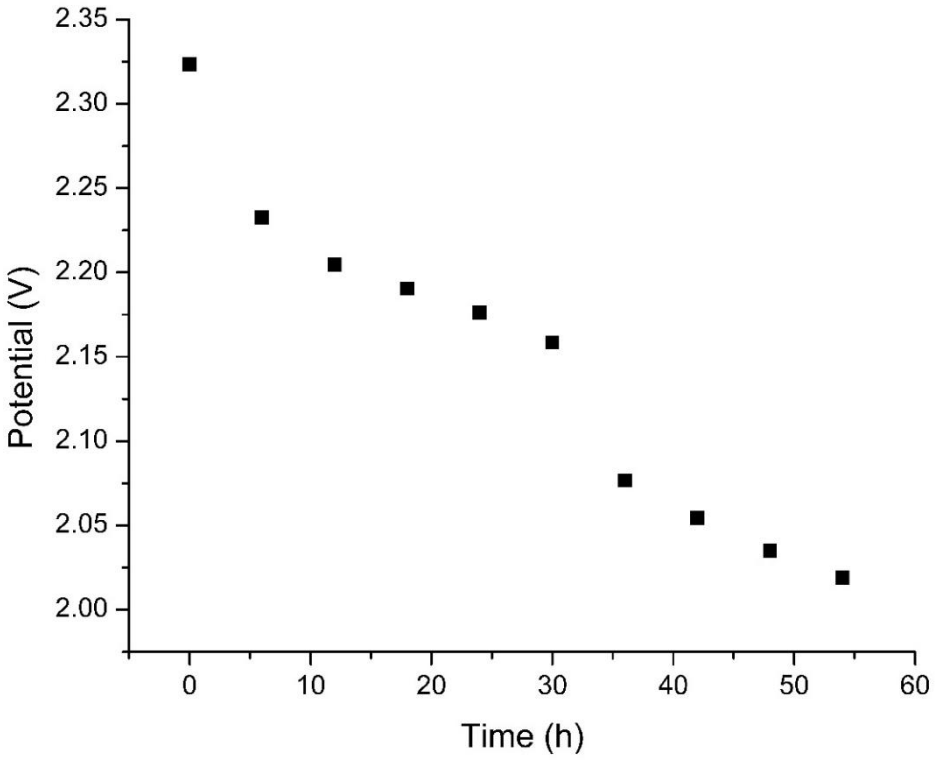

Figure 5.9: OCP self-discharge test of 0.023 M [Ni(cyclam)]$(BF_4)_2$ in 0.2 M [Bu_4N][PF_6] MeCN starting at a 75% SOC.

The first charge curve of the trans(I)-[Ni(TMC)]$(BF_4)_2$ had two distinct charging plateaus (Figure 5.10). This is likely due to different isomers being present in solution that have slightly different potential gaps, which aligns with redox events observed in the CVs (Figure 5.6). When the cell began to discharge, the potential rapidly declined until it hit the lower potential cut off. Since the cell was not able to fully discharge after the first cycle, all subsequent cycles were cut short. The potential of the charging curve of the first cycle was around the expected potential of 2.4 V, while the discharge curve did not start until around 1.4 V. This significant difference suggests the overpotential observed during discharge is largely in part due to the charge carrier and not the internal cell resistance.

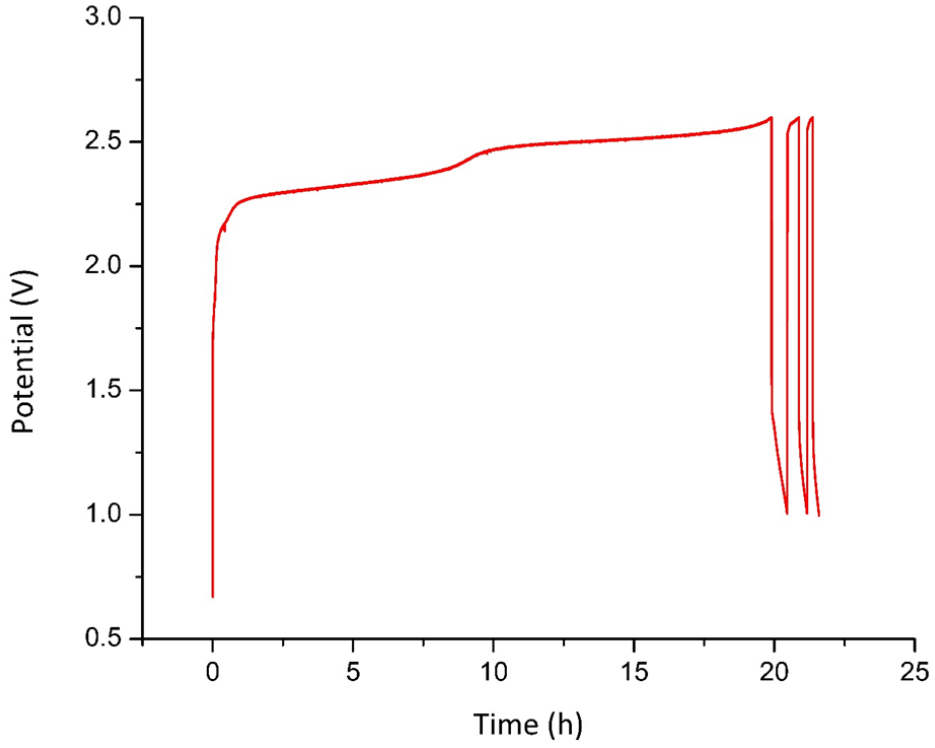

Figure 5.10: Galvanostatic charge-discharge curves of 0.014 M trans(I)-[Ni(TMC)]$(BF_4)_2$ in 0.2 M [Bu_4N][BF_4] MeCN with Pt. electrode applying a 125 µA charging and -62.5 µA discharging current.

We cycled the Trans(III)-[Ni(TMC)]$(BF_4)_2$ to a 75% SOC, but only attained a 14% SOC on the first cycle before the potential cut off was exceeded (Figure 5.11). Over the subsequent 8 cycles, the cell was not able to reach the 14% SOC and began to slowly decline each cycle. The faradaic efficiency for the cell was extremely inconsistent between cycle, ranging from 81% to a (physically unrealistic) 147%. The first cycle had a faradaic efficiency of 147%, implying redox at species beside the Ni(II) center in the Trans(III)-[Ni(TMC)] was occurring in the cell during discharge. The rest of the cycles varied between 81% and 92% faradaic efficiency.

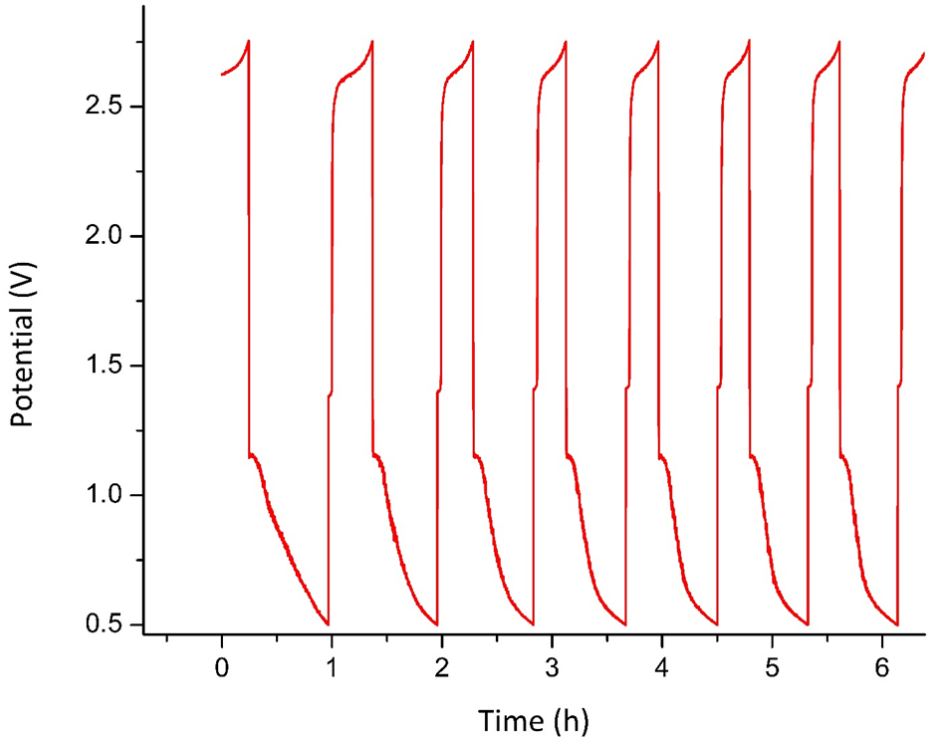

Figure 5.11: Galvanostatic charge-discharge curves of 0.014 M trans(III)-[Ni(TMC)]$(BF_4)_2$ in 0.2 M [Bu_4N][BF_4] MeCN with Pt. electrode applying a 125 µA charging and -62.5 µA discharging current.

5.3. Summary

We found that [Ni(Cyclam)]$(BF_4)_2$ and trans(III)-[Ni(TMC)]$(BF_4)_2$ have two quasi-reversible redox events with a large difference in potential between them. While these metal complexes had promising redox events in their CVs, these properties did not transfer to solution state cycling of the complexes. All the metal complexes tested had poor stability when cycling, degrading after only a few cycles.

5.4. Experimental

Techniques and Reagents. HPLC grade Acetonitrile (Fisher Chemical) was dried over activated 4 Å molecular sieves for 24 hours under a nitrogen atmosphere on a Schlenk line, filtered through celite, then distilling over CaH_2 (ACROS Organics), and stored in a glovebox over activated 4 Å molecular sieves. Tetrabutylammonium Tetrafluoroborate ($[Bu_4N][BF_4]$) was twice recrystallized from hot ethanol and dried at 50 °C under dynamic vacuum (<0.1 torr) for 24 hours before use. Cyclam (1,4,8,11-tetraazamacrocycle) and TMC (l,4,8,ll-tetramethyl-l,4,8,ll-tetraazacyclotetradecane) were used as purchased.

NMR spectra were obtained on an Agilent Technologies 400 MHz spectrometer and referenced to residual solvent resonances of chloroform ($CDCl_3$) or externally (^{11}B: 85% $(Et_2O)BF_3$, ^{31}P: 85% H_3PO_4,).

Cycling Experiments: All electrochemical measurements were performed in a glovebox under an inert argon atmosphere using a Metrohm Autolab PGSTAT128N potentiostat/galvanostat. Two coiled Pt electrodes (Bio-Logic) were cleaned before use by rinsing with acetone and heating white-hot with a butane torch. All electrodes were transferred into the glovebox and subsequently rinsed with the respective electrolyte solution immediately prior to use. The H-cells were custom-made by the in-house glassblower and oven dried overnight at 150 °C prior to use.

Electrochemistry experiments were carried out using a Metrohm Autolab PGSTAT128N potentiostat/galvanostat and carried out inside an argon glovebox.

Synthesis

$[Ni(Cyclam)](BF_4)_2$. A 20 mL vial with a stir bar was charged with Cyclam (540.9 mg, 2.7 mmols) and ~10 mL of ethanol. $Ni(BF_4)_2 \cdot 6H_2O$ (875.3 mg, 2.57 mmols) was added to this

solution and stirred overnight. Diethyl ether (~5 mL) was added to the solution crashing out [Ni(Cyclam)]$(BF_4)_2$ and stirred for an additional 10 minutes. The product was purified by recrystallizing in MeCN and layering with benzene to yield 903 mg (77.3%). Single crystals were taken for XRD. **^{1}H NMR** (400 MHz, MeCN-d_3) δ 13.94 (s, 6H), 5.31(s, 4H), -5.14 (s, 4H), -15.71 (s, 6H). **^{11}B NMR** (128 MHz, MeCN-d_3) δ -0.95. **^{19}F NMR** (376 MHz, MeCN-d_3) δ -149.37.

Trans(I)-[Ni(TMC)]$(BF_4)_2$. A 20 mL vial with a stir bar was charged with TMC (50 mg, 0.195 mmols) and ~10 mL of ethanol. $Ni(BF_4)_2 \cdot 6H_2O$ (69.7 mg, 0.2 mmols) was added to this solution and stirred overnight. Diethyl ether (~5 mL) was added to the solution crashing out Trans(I)-[Ni(TMC)]$(BF_4)_2$ and stirred for an additional 10 minutes. The product was purified by recrystallizing in MeCN and layering with benzene to yield 80 mg (84%). **^{1}H NMR** (400 MHz, MeCN-d_3) δ 108.24 (s, 4H), 87.92 (s, 2H), 81.43 (s, 15H), 42.65 (s, 6H), 4.19 (s, 2H), -15.08 (s, 3H). **^{11}B NMR** (128 MHz, MeCN-d_3) δ 3.87. **^{19}F NMR** (376 MHz, MeCN-d_3) δ -112.6.

Trans(III)-[Ni(TMC)]$(BF_4)_2$. [Ni(Cyclam)]$(BF_4)_2$ (0.5g, 1.15 mmols) was dissolved in 12.5 mL DMSO. Crushed KOH (2 g, excess) was added to the solution and stirred vigorously for 5 minutes. The KOH was then filtered off and methyl iodide (0.5 mL) was added to the solution. After stirring for an additional 30 minutes, a second round of crushed KOH (2 g, excess) was added. After 5 minutes of additional stirring, the KOH was then filtered off and methyl iodide (0.75 mL) was added again to the solution. The solution was left to stir for 30 forming a brick red precipitate. Ethanol (12.5 mL) was then added to the solution and the solids filter off. The isolated solids were then dissolved in hot water and $AgBF_4$ (2.3 mmols) was subsequently added to the solution. The solution was then filtered, and the filtrate

collected in a fresh round bottom. The solution was then cooled to room temperature causing the product to crash out. The product was further purified by recrystallization in MeCN layered with benzene to yield 70 mg, (17%). Single crystals were taken for XRD. **^{1}H NMR** (400 MHz, MeCN-d_3) δ 117.93 (s, 6H), 24.68 (s, 12H), 9.51 (d, J = 937.3 Hz, 6H), 1.52 (s, 6H), -13.10 (s, 6H). **^{11}B NMR** (128 MHz, MeCN-d_3) δ -0.27. **^{19}F NMR** (376 MHz, MeCN-d_3) δ -146.1.

5.5. References

(1) DOE. *Energy Storage Grand Challenge Cost and Performance Assessment 2020*; DOE/PA-0204; 2020. https://www.energy.gov/energy-storage-grand-challenge/downloads/2020-grid-energy-storage-technology-cost-and-performance.

(2) Li, Z.; Jiang, T.; Ali, M.; Wu, C.; Chen, W. Recent Progress in Organic Species for Redox Flow Batteries. *Energy Stor. Mater.* **2022**, *50*, 105-138. DOI: https://doi.org/10.1016/j.ensm.2022.04.038.

(3) Kwabi, D. G.; Lin, K.; Ji, Y.; Kerr, E. F.; Goulet, M.-A.; De Porcellinis, D.; Tabor, D. P.; Pollack, D. A.; Aspuru-Guzik, A.; Gordon, R. G.; et al. Alkaline Quinone Flow Battery with Long Lifetime at pH 12. *Joule* **2018**, *2* (9), 1894-1906. DOI: https://doi.org/10.1016/j.joule.2018.07.005.

(4) Kent Barefield, E. Coordination chemistry of N-tetraalkylated cyclam ligands—A status report. *Coord. Chem. Rev.* **2010**, *254* (15), 1607-1627. DOI: https://doi.org/10.1016/j.ccr.2010.03.007.

(5) Wagner, F.; Barefield, E. K. N-Alkylation of macrocyclic secondary amine complexes of nickel(II). *Inorg. Chem.* **1976**, *15* (2), 408-417. DOI: 10.1021/ic50156a034.

(6) Barefield, E. K.; Wagner, F. Metal complexes of 1,4,8,11-tetramethyl-1,4,8,11-tetraazacyclotetradecane, N-tetramethylcyclam. *Inorg. Chem.* **1973**, *12* (10), 2435-2439. DOI: 10.1021/ic50128a042.

(7) Kim, H.-s.; Yoon, T.; Jang, J.; Mun, J.; Park, H.; Ryu, J. H.; Oh, S. M. A tetradentate Ni(II) complex cation as a single redox couple for non-aqueous flow batteries. *J. Power Sources* **2015**, *283*, 300-304. DOI: https://doi.org/10.1016/j.jpowsour.2015.02.083.